

OPTIMIZATION OF COMPLIANT PARTS OF A HYBRID TRAILING EDGE
CONTROL SURFACE OF A MORPHING UNMANNED AERIAL VEHICLE

A THESIS SUBMITTED TO
THE GRADUATE SCHOOL OF NATURAL AND APPLIED SCIENCES
OF
MIDDLE EAST TECHNICAL UNIVERSITY

BY
PINAR ARSLAN

IN PARTIAL FULFILLMENT OF THE REQUIREMENTS
FOR
THE DEGREE OF MASTER OF SCIENCE
IN
AEROSPACE ENGINEERING

JANUARY 2017

Approval of the thesis:

**OPTIMIZATION OF COMPLIANT PARTS OF A HYBRID TRAILING EDGE
CONTROL SURFACE OF A MORPHING UNMANNED AERIAL VEHICLE**

submitted by **PINAR ARSLAN** in partial fulfillment of the requirements for the degree of **Master of Science in Aerospace Engineering Department, Middle East Technical University** by,

Prof. Dr. Gülbin Dural Ünver
Dean, Graduate School of **Natural and Applied Sciences**

Prof. Dr. Ozan Tekinalp
Head of Department, **Aerospace Engineering**

Assist. Prof. Dr. Ercan Gürses
Supervisor, **Aerospace Engineering Dept., METU**

Examining Committee Members:

Prof. Dr. Yavuz Yaman
Aerospace Engineering Dept., METU

Assist. Prof. Dr. Ercan Gürses
Aerospace Engineering Dept., METU

Prof. Dr. Serkan Özgen
Aerospace Engineering Dept., METU

Assoc. Prof. Dr. Melin Şahin
Aerospace Engineering Dept., METU

Assist. Prof. Dr. Barış Sabuncuoğlu
Mechanical Engineering Dept., UTAA

Date:

26.01.2017

I hereby declare that all information in this document has been obtained and presented in accordance with academic rules and ethical conduct. I also declare that, as required by these rules and conduct, I have fully cited and referenced all material and results that are not original to this work.

Name, Last Name: Pınar Arslan

Signature :

ABSTRACT

OPTIMIZATION OF COMPLIANT PARTS OF A HYBRID TRAILING EDGE CONTROL SURFACE OF A MORPHING UNMANNED AERIAL VEHICLE

Arslan, Pınar

M.S., Department of Aerospace Engineering

Supervisor : Assist. Prof. Dr. Ercan Gürses

January 2017, 104 pages

In this thesis, optimization studies are conducted for compliant parts of a hybrid trailing edge control surface of an unmanned aerial vehicle (UAV).

The geometry of the control surface was taken from a previous study conducted in [1], and then regenerated parametrically through Design Modeler tool of ANSYS Workbench v15.0. The finite element model of the control surface is created by using ANSYS Workbench v15.0 Static Structural module. The optimization study of the compliant part is conducted by using Adaptive Multiple Objective method in Direct Optimization tool of ANSYS Design Exploration module. Two different control surface designs and four different hyperelastic materials for compliant parts are considered. The input parameters of the optimization are the dimensions of the compliant part of the control surface and the amount of actuations of the servo actuators. This optimization study is constrained by the limit torque of the servo actuators, the yield stress of the aluminum parts of the design and the minimum and maximum strain

values for the compliant parts. The tip deflection of the control surface required to provide the desired wing profile is specified as the target. According to the specified inputs, constraints and the target, optimal control surface design is selected from among the results of the optimization analyses.

Finally, the selected design is checked against aerodynamic loads calculated in a previous work [1].

Keywords: Direct Optimization Analyses, Compliant Materials, Hyperelastic Materials, Hybrid Control Surface, Finite Element Analysis

ÖZ

ŞEKİL DEĞİŞTİREBİLEN BİR İNSANSIZ HAVA ARACININ HİBRİT FİRAR KENARI KONTROL YÜZEYİNİN UYUMLU PARÇALARININ OPTİMİZASYONU

Arslan, Pınar

Yüksek Lisans, Havacılık ve Uzay Mühendisliği Bölümü

Tez Yöneticisi : Yrd. Doç. Dr. Ercan Gürses

Ocak 2017 , 104 sayfa

Bu tezde, bir insansız hava aracının (İHA) hibrit arka kenarı kontrol yüzeyinin esnek parçaları için optimizasyon çalışmaları yürütülmüştür.

Kontrol yüzeyinin geometrisi [1]'de gerçekleştirilen daha önceki bir çalışmadan alınmış ve daha sonra ANSYS Workbench v15.0'un Tasarım Modelleme aracı ile parametrik olarak yeniden oluşturulmuştur. Kontrol yüzeyinin sonlu elemanlar modeli ise ANSYS Workbench v15.0 Statik Yapısal modül kullanılarak üretilmiştir. Esnek parçaların optimizasyon çalışması, ANSYS Tasarım Araştırması modülünün Doğrudan Optimizasyon aracında Uyarlanabilir Çok Amaçlı yöntem kullanılarak gerçekleştirilmiştir. Optimizasyon çalışmasında, iki farklı kontrol yüzeyi tasarımı ve esnek parçalar için dört farklı hiperelastik malzeme incelenmiştir. Optimizasyonun girdi parametreleri, kontrol yüzeyinin esnek parçalarının boyutları ve servo motorların tahrik miktarlarıdır. Bu optimizasyon çalışması, servo motorların limit torku, tasarımın

alüminyum kısımlarının akma gerilmeleri ve esnek parçaların minimum ve maksimum gerinim değerleri ile sınırlandırılmıştır. İstenilen kanat profilini elde etmek için gereken kontrol yüzeyi uç sapması hedef olarak belirtilmiştir. Belirlenen girdilere, kısıtlara ve hedefe göre, optimizasyon analizlerinin sonuçları arasından optimum kontrol yüzeyi tasarımı seçilmiştir.

Son olarak, seçilen tasarım daha önce [1]'de gerçekleştirilen çalışmada hesaplanan aerodinamik yükler altında kontrol edilmiştir.

Anahtar Kelimeler: Doğrudan Optimizasyon Analizleri, Esnek Malzemeler, Hipere-
lastik Malzemeler, Hibrit Kontrol Yüzeyi, Sonlu Elemanlar Analizi

*To my father,
for leaving happy memories*

ACKNOWLEDGMENTS

I would like to express my greatest gratitude to my supervisor Asst. Prof. Dr. Ercan Gürses, for giving me an opportunity to work with him, his valuable comments and his endless patience throughout my study.

I am also thankful to my superiors within the CHANGE project, Prof. Dr. Yavuz Yaman, Assoc. Prof. Dr. Melin Şahin and Prof. Dr. Serkan Özgen for their supports during the studies.

I must also express my gratitude to my colleagues in CHANGE project İlhan Ozan Tunçöz, Uğur Kalkan, Harun Tıraş and Yosheph Yang. Without their help and patience, this study would not finished.

I also appreciate the support of my invaluable coworkers from Turkish Aerospace Industries Derya Gürak, Seyhan Gül and Fatih Mutlu Karadal for always promoting me and believing in me.

I would like to thank to my mother, my sister, my uncle Nazım Arslan and my primary school teacher Sabriye Arkat for their love, care and support. I also would like to express my thanks to Özgün Dülger, my love, for loving me and making each day of my life meaningful.

The work presented herein has been partially funded by the European Community's Seventh Framework Programme (FP7) under the Grant Agreement 314139. The CHANGE project ("Combined morphing assessment software using flight envelope data and mission based morphing prototype wing development") is a L1 project funded under the topic AAT.2012.1.1-2 involving nine partners. The project started in August, 1, 2012. The author gratefully acknowledges the support given.

TABLE OF CONTENTS

ABSTRACT	v
ÖZ	vii
ACKNOWLEDGMENTS	x
TABLE OF CONTENTS	xi
LIST OF TABLES	xv
LIST OF FIGURES	xviii
LIST OF ABBREVIATIONS	xxii
LIST OF SYMBOLS	xxiii
CHAPTERS	
1 INTRODUCTION	1
1.1 Background and Motivation to the Study	1
1.2 Scope of the Thesis	2
1.3 Limitations of the Thesis	3
2 REVIEW OF MORPHING AIRCRAFT	5
2.1 Introduction	5
2.2 Benefits of Morphing	7

2.3	Drawbacks of Morphing	8
2.4	Adaptive Control Surface Concepts (Camber Variable Wings)	9
2.5	Materials for Morphing Skin	15
3	PARAMETRIC MODELING OF THE CONTROL SURFACE AND THE DESCRIPTION OF THE OPTIMIZATION PROBLEM	17
3.1	Introduction	17
3.2	Mission Profile of the Morphing Wing	17
3.3	Design of the Hybrid Trailing Edge Control Surface	19
3.4	Input Parameters of Compliant Part Optimization	22
3.4.1	Materials of the Compliant Part	23
3.4.2	Dimensions of the Compliant Part	25
3.4.3	Rotation Angles Inputs to the Servo Actuators	26
3.5	Objective and Constraints of Compliant Part Optimization	28
3.6	Optimization Theory and Procedures	30
4	STRUCTURAL ANALYSES AND OPTIMIZATION OF THE COM- PLIANT PARTS OF THE CONTROL SURFACE IN-VACUO CON- DITION	37
4.1	Introduction	37
4.2	Finite Element Model of the Hybrid Control Surface	37
4.2.1	Finite Element Model of the Open Cell Control Surface	38
4.2.2	Finite Element Model of the Closed Cell Control Surface	42
4.3	Optimization Analyses	43

4.4	Results of Optimization Analyses	45
4.4.1	Results of Open Cell Control Surface Design	45
4.4.2	Results of Closed Cell Control Surface Design	47
4.5	Selection of Best Design Configuration	48
4.6	Analysis of Morphing from NACA 6510 to NACA 3510	51
4.7	Conclusion and Discussion	54
5	FINITE ELEMENT ANALYSIS OF THE OPTIMIZED HYBRID CONTROL SURFACE DESIGN UNDER AERODYNAMIC LOADS	57
5.1	Introduction	57
5.2	Aerodynamic Loads	57
5.3	Structural Analysis of the Optimized Control Surface Design under Aerodynamic Loads	59
5.3.1	Results of the Analysis of Maintaining NACA 6510 Airfoil Case	63
5.3.2	Results of the Analysis of Deflection to NACA 3510 Airfoil Case	65
5.3.3	Results of the Analysis of Deflection to NACA 2510 Airfoil Case	67
5.4	Conclusion and Discussion	69
6	CONCLUSION AND FUTURE WORK	71
6.1	Conclusion	71
6.2	Key Findings	72
6.3	Future Work	73
	REFERENCES	75

APPENDICES

A OPTIMIZATION RAW DATA 79

B EFFECT OF SAMPLE SIZE AND OPTIMIZATION METHOD ON
BEST CANDIDATE POINT 101

C VISUALIZATION OF PARETO FRONTS OF OBJECTIVE FUNC-
TIONS 103

LIST OF TABLES

TABLES

Table 3.1	Dimensions of the morphing wing and trailing edge control surface .	18
Table 3.2	Dimensions and materials of the hybrid trailing edge control surface	20
Table 3.3	Material properties of aluminum [34]	20
Table 3.4	The specifications of the servo actuator [36]	21
Table 3.5	Material constants of the hyperelastic materials	25
Table 3.6	Continuous input parameters of the optimization study	27
Table 3.7	Output parameters and their abbreviations	29
Table 3.8	Objectives and constraints of the optimization study	30
Table 4.1	Element types and sizes of the control surface parts [44]	39
Table 4.2	The input values of candidate points for neoprene rubber compliant part of the open cell control surface	46
Table 4.3	The output values of candidate points for neoprene rubber compliant part of the open cell control surface	46
Table 4.4	The input values of candidate points for sample elastomer-1 compliant part of the open cell control surface	46
Table 4.5	The output values of candidate points for sample elastomer-1 compliant part of the open cell control surface	47
Table 4.6	The input values of candidate points for neoprene rubber compliant part of the closed cell control surface	47
Table 4.7	The output values of candidate points for neoprene rubber compliant part of the closed cell control surface	48
Table 4.8	The input values of candidate points for sample elastomer-1 compliant part of the closed cell control surface	48

Table 4.9 The output values of candidate points for sample elastomer-1 compliant part of the closed cell control surface	48
Table 4.10 Factor of safety values of servo torque reactions and combined stress values of beams for best control surface design	50
Table 4.11 The input values of the selected simplified candidate design point for the analysis of morphing the control surface to NACA 2510 from NACA 6510	50
Table 4.12 The corresponding output values to the selected simplified candidate design point for the analysis of morphing the control surface to NACA 2510 from NACA 6510	50
Table 4.13 The input values of the selected simplified candidate design point for the analysis of morphing the control surface to NACA 3510 from NACA 6510	52
Table 4.14 The corresponding output values to the selected simplified candidate design point for the analysis of morphing the control surface to NACA 3510 from NACA 6510	52
Table 5.1 Input parameters for the CFD analyses	58
Table 5.2 The input values of the finite element analysis under aerodynamic loads	63
Table 5.3 Results of the finite element analysis of maintaining NACA 6510 airfoil profile under aerodynamic loads	64
Table 5.4 Results of the finite element analysis of the deflection to NACA 3510 airfoil under aerodynamic loads	65
Table 5.5 Results of the finite element analysis of the deflection to NACA 2510 airfoil under aerodynamic loads	67
Table 6.1 The dimensions of the compliant parts of the best control surface design	72
Table A.1 The input values of optimization design points for neoprene rubber compliant part of the open cell control surface	79
Table A.2 The corresponding output values to the input values of optimization design points for neoprene rubber compliant part of the open cell control surface	89

Table B.1	The properties of different optimization cases	101
Table B.2	The input values of each optimization analysis	102
Table B.3	The output values corresponds to the input data of each optimization analysis	102

LIST OF FIGURES

FIGURES

Figure 1.1	Definition schema of the CHANGE Project [2]	2
Figure 2.1	Timeline of fixed wing aircraft implementing morphing technologies [7]	7
Figure 2.2	Geometry of a sub-optimal morphing truss (red dotted lines represent SMA elements): a) upward deformed, b) downward deformed and c) undeformed [19]	10
Figure 2.3	Baseline elastomer skin–flexcore control surface structure [21] . . .	11
Figure 2.4	The morphing flap with eccentuator device: (a) inner part of the flap (b) downward deflected and (c) upward deflected [22]	11
Figure 2.5	DLR finger concept [26]	12
Figure 2.6	DLR belt rib concept [27]	13
Figure 2.7	Ball linkage mechanism for leading edge control surface [28] . . .	13
Figure 2.8	Straight guide system for trailing edge control system [28]	14
Figure 2.9	Morphing UAV designed by METU within the scope of TÜBİTAK Project 107M103 [29]	14
Figure 2.10	The Guide-Slide Assembly of the METU Hingeless Control System [30]	15
Figure 3.1	The base wing geometry and the trailing edge control surface [1] .	18
Figure 3.2	The mission profile of the morphing unmanned aerial vehicle [1] .	18
Figure 3.3	NACA airfoils and corresponding flight missions of Morphing Wing	19
Figure 3.4	Closed and open cell designs of hybrid control surface with transmission parts [1]	19

Figure 3.5	Moment arm, designed actuation rod, C part connector of Volz DA 13-05-60 servo actuator and full assembly of them [36] [1]	21
Figure 3.6	Placement of the servo actuators (top view) [1]	22
Figure 3.7	Placement of the servo actuators (side view) [1]	22
Figure 3.8	The uniaxial test data of the hyperelastic materials and their curve fit data	24
Figure 3.9	The parametric inputs of the control surface	25
Figure 3.10	The points where moment arm rotation angles applied on the control surface	27
Figure 3.11	The coordinate systems of the upper and lower compliant parts	29
Figure 3.12	The decision space and the objective space in multi-objective optimization problems [42]	33
Figure 3.13	Example of Pareto front [42]	34
Figure 3.14	The workflow schema of the Adaptive Multiple-Objective optimization method	36
Figure 4.1	General dimensions of the open cell control surface design [1]	38
Figure 4.2	Isometric view of the open cell hybrid control surface	38
Figure 4.3	Side view of the open cell hybrid control surface	39
Figure 4.4	Finite element model of the open cell control surface design (isometric view)	40
Figure 4.5	Finite element model of the open cell control surface design (side view)	40
Figure 4.6	Constrained nodes of the moment arms and actuation rods of the servo actuators	41
Figure 4.7	Bonded contact between actuation rods of the servo actuators and transmission parts of the control surface	41
Figure 4.8	Applied boundary conditions of the finite element model	42
Figure 4.9	Finite element model of the closed cell control surface design (isometric view)	43

Figure 4.10 Finite element model of the closed cell control surface design (side view)	43
Figure 4.11 Inputs distribution in Optimal Space Filling method [40]	44
Figure 4.12 Displacement of the control surface in z direction in case of morphing from NACA 6510 profile to NACA 2510 profile	50
Figure 4.13 Minimum combined beam stress distribution in case of morphing from NACA 6510 profile to NACA 2510 profile	51
Figure 4.14 Maximum combined beam stress distribution in case of morphing from NACA 6510 profile to NACA 2510 profile	51
Figure 4.15 Displacement of the control surface in z direction in case of morphing from NACA 6510 profile to NACA 3510 profile	52
Figure 4.16 Minimum combined beam stress distribution in case of morphing from NACA 6510 profile to NACA 3510 profile	53
Figure 4.17 Maximum combined beam stress distribution in case of morphing from NACA 6510 profile to NACA 3510 profile	53
Figure 5.1 Aerodynamic Mesh of the Morphing Wing and Hemisphere Outer Domain Mesh [1]	58
Figure 5.2 Imported pressure applied to the upper skin of the control surface in case of maintaining NACA 6510 profile	60
Figure 5.3 Imported pressure applied to the lower skin of the control surface in case of maintaining NACA 6510 profile	61
Figure 5.4 Imported pressure applied to the upper skin of the control surface in case of deflection to NACA 3510 profile	61
Figure 5.5 Imported pressure applied to the lower skin of the control surface in case of deflection to NACA 3510 profile	62
Figure 5.6 Imported pressure applied to the upper skin of the control surface in case of deflection to NACA 2510 profile	62
Figure 5.7 Imported pressure applied to the lower skin of the control surface in case of deflection to NACA 2510 profile	63
Figure 5.8 Displacement of the control surface in z direction while maintaining NACA 6510 profile under aerodynamic loads	64

Figure 5.9 Minimum combined beam stress distribution while maintaining NACA 6510 profile under aerodynamic loads	64
Figure 5.10 Maximum combined beam stress distribution while maintaining NACA 6510 profile under aerodynamic loads	65
Figure 5.11 Displacement of the control surface in z direction while morphing from NACA 6510 to NACA 3510 profile under aerodynamic loads	66
Figure 5.12 Minimum combined beam stress distribution while morphing from NACA 6510 to NACA 3510 profile under aerodynamic loads	66
Figure 5.13 Maximum combined beam stress distribution while morphing from NACA 6510 to NACA 3510 profile under aerodynamic loads	67
Figure 5.14 Displacement of the control surface in z direction while morphing from NACA 6510 to NACA 2510 profile under aerodynamic loads	68
Figure 5.15 Minimum combined beam stress distribution while morphing from NACA 6510 to NACA 2510 profile under aerodynamic loads	68
Figure 5.16 Maximum combined beam stress distribution while morphing from NACA 6510 to NACA 2510 profile under aerodynamic loads	69
Figure C.1 Comparison of raw data and Pareto Front for torque reaction of the servo to actuate the lower part and tip deflection of the control surface in z-direction	103
Figure C.2 Comparison of raw data and Pareto Front for torque reaction of the servo to actuate the upper part and tip deflection of the control surface in z-direction	104
Figure C.3 Comparison of raw data and Pareto Front for torque reactions of the servo to actuate the upper and lower parts	104

LIST OF ABBREVIATIONS

AMO	Adaptive Multiple-Objective
CFD	Computational Fluid Dynamics
CHANGE	Combined morphing Assessment software using flight Envelope data and mission based morphing prototype wing development
CP	Candidate Point
DARPA	Defense Advanced Research Program Agency
DLR	The German Aerospace Center
FEA	Finite Element Analysis
METU	Middle East Technical University
MOGA	Multi-Objective Genetic Algorithm
NASA	National Aeronautics and Space Administration
NSGA-II	Non-dominated Sorted Genetic Algorithm- II
OSF	Optimal Space Filling
RANS	Reynolds Averaged Navier-Stokes
RS	Response Surface
SMA	Shape Memory Alloys
SU2	Stanford University Unstructured
TAI	Turkish Aerospace Industries
TÜBİTAK	The Scientific and Technological Research Council of Turkey
UAV	Unmanned Aerial Vehicle
VGT	Variable Geometry Trusses

LIST OF SYMBOLS

d	Incompressibility Parameter
d_z	Tip Deflection of the Control Surface in Z-Direction
E	Young's Modulus
L_u	Length of Upper Compliant Part
L_l	Length of Lower Compliant Part
Q_l	Torque Reaction of the Servo to Actuate the Lower Part
Q_u	Torque Reaction of the Servo to Actuate the Upper Part
R_{y_u}	Rotation of Servo Actuators to Actuate the Upper Compliant Part
R_{y_l}	Rotation of Servo Actuators to Actuate the Lower Compliant Part
t_u	Thickness of Upper Compliant Part
t_l	Thickness of Lower Compliant Part
ϵ_{lmin}	Minimum Normal Elastic Strain of the Lower Compliant Part
ϵ_{umin}	Minimum Normal Elastic Strain of the Upper Compliant Part
ϵ_{lmax}	Maximum Normal Elastic Strain of the Lower Compliant Part
ϵ_{umax}	Maximum Normal Elastic Strain of the Upper Compliant Part
μ	Initial Shear Modulus
ν	Poisson's Ratio
ρ	Density
σ_{cmin}	Minimum Combined Stress of the Beams
σ_{cmax}	Maximum Combined Stress of the Beams

CHAPTER 1

INTRODUCTION

1.1 Background and Motivation to the Study

Conventional aircraft generally have been designed and optimized for the conditions which take most of the time of flight in terms of aerodynamic performance. Increasing the flight envelope of a conventional aircraft is possible by adding morphing features to the existing aircraft. By this way, morphing aircraft can be aerodynamically optimized for more than a single phase of a flight. The development of new flexible materials allows the use of compliant skins in morphing wing designs. For this reason, in this thesis different compliant materials and different geometries are examined for the optimization of the flexible skin parts in a hybrid trailing edge control surface.

An adaptive trailing edge control surface has been designed under the scope of the CHANGE Project (Combined morpHing Assessment software usiNG flight Envelope data and mission based morphing prototype wing development) which is a 7th Framework Programme Project of the European Commission. The aim of this project illustrated in Figure 1.1 is association of four different morphing mechanisms to one unmanned aerial vehicle and verify with flight and wind tunnel tests. Types of morphing studied in CHANGE project are telescopic, camber, twist and sweep variable wings. The responsibility of METU in this project was to design a morphing trailing edge control surface allowing the wing to change its camber [2]. To this end, a hybrid control surface consisting of aluminum and compliant parts was designed. The control surface is capable of morphing from NACA 6510 profile to NACA 3510 and NACA 2510 profiles.

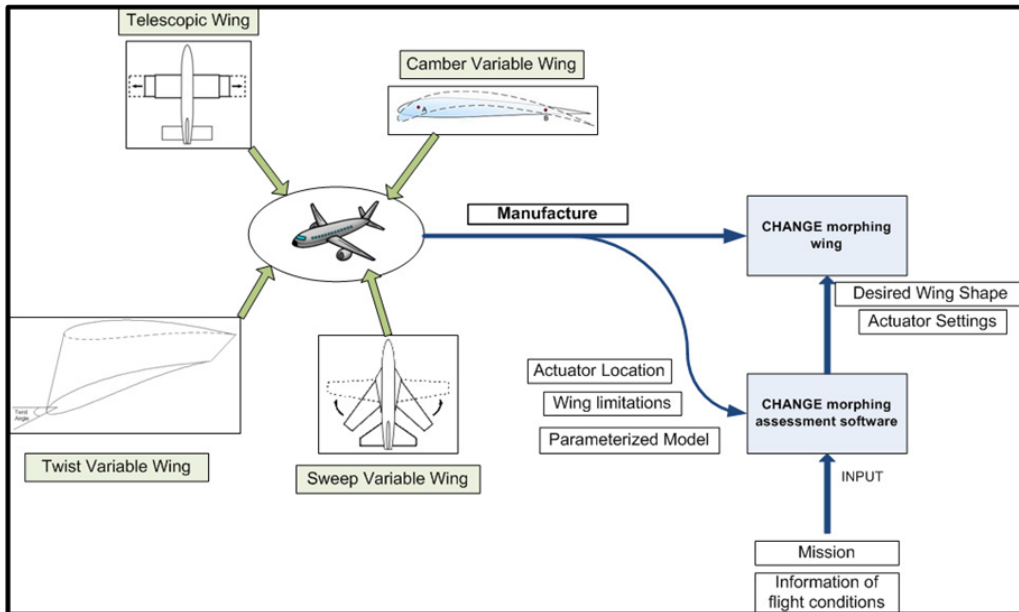


Figure 1.1: Definition schema of the CHANGE Project [2]

1.2 Scope of the Thesis

In this thesis, compliant parts of the hybrid control surface are optimized in terms of the materials used and geometric dimensions.

In chapter 2, the literature review about morphing wings is presented. First, the meaning, benefits and drawbacks of different morphing concepts are explained. Then, several camber variable wing designs examples are given. Finally, materials which can be used in morphing skins and their properties are addressed.

Chapter 3 is dedicated to the modeling of the control surface and the inputs of optimization study. In the first section, the mission profile of the adaptive wing is presented. In the second section, parametric modeling of the control surface is addressed. In the third section, input parameters, objectives and constraints of the optimization study conducted for compliant parts are presented. In the final section, the optimization procedure is explained.

In chapter 4, the optimization analyses of the compliant skin of the control surface are presented. First, finite element models of the open cell and closed cell control surface designs are explained, and the method of optimization analyses is addressed.

Then the results of these optimization analyses are presented and the selection of the optimum control surface design is explained. In addition, structural analysis of the selected best design, during the deflection of the control surface from NACA 6510 to NACA 3510 airfoil profile, is presented.

Chapter 5 is devoted to the structural analysis of the optimum control surface design under aerodynamic loads. Results are presented for the non-deflected control surface and the deflected control surface from base NACA 6510 profile to both NACA 3510 and NACA 2510 airfoil profiles.

In Chapter 6, the general conclusions obtained from this study and potential future works are given.

1.3 Limitations of the Thesis

This study is limited to the optimization of only the compliant parts of the hybrid trailing edge control surface. The locations and numbers of the servo actuators are not changed.

In this thesis, manufacturability concerns were not addressed. Therefore, connections between parts of the control surface are not considered. The connections of the control surface to the wing are not modeled. Additionally, the servo actuators are not considered in the finite element model.

Structural analyses under aerodynamic loads are conducted only for 1g aerodynamic loading. For this reason, maneuvers causing higher aerodynamic loads are not included in this thesis.

CHAPTER 2

REVIEW OF MORPHING AIRCRAFT

In this chapter, a literature review on fixed wing morphing aircraft is presented. First, a short introduction about morphing wings are given and benefits and drawbacks of the morphing aircraft are explained. Then, examples of the morphing control surfaces are given. Finally, necessary properties of skin materials which can be used in morphing wings are explained.

2.1 Introduction

In the world, the most sophisticated and elegant flying objects are birds. Therefore, human being has been fascinated by the birds' freedom and wanted to fly like them since their existence. Due to the thousands of year evolution, birds perform different missions in the same flight in a very efficient way. For example, they are able to change shape rapidly from loiter to abrupt maneuvering and descent to catch their prey [3]. By observing such abrupt maneuvers of the animal species, flying with ability to morph has attracted the mankind. Although, the first designs of flying machines were simple and rough compared to today's machines, nature has been continuing to teach us a lot more about efficiency, simplicity and elegance of the animals. In terms of morphing capabilities, the composition of the structure and function of birds' wings impress the designers in order to develop flying machines [4].

Morphing is similar to a short-term metamorphose. In the aviation field, Weisshaar defined morphing aircraft as "multi-role aircraft that change their external shape substantially to adapt to a changing mission environment during flight". Morphing aircraft are also known as variable geometry or polymorphous aircraft [5].

At first, the idea of changing the wing shape and geometry of the flying machines were considered in the design of The Wright Flyer in 1903. In the first design with an engine and heavier-than-air flying machine, The Wright Flyer, roll control was enabled by changing twist of its wing using cables by the pilot [6]. In the following years, applications of the morphing concepts have been added to this study. As indicated in Figure 2.1, Barbarino et al. gave a chronological summary of morphing technologies implemented on the fixed wings from 1903 to 2010 [7].

These morphing concepts can be classified into three different criteria in terms of a shape variation: planform change, out-of-plane transformation, and airfoil adjustment. Planform morphing involves change of span, chord and sweep of the aircraft. Out-of-plane transformation consists of wing twisting, chord-wise bending and span-wise bending. Airfoil adjustment is obtained by changing mainly camber and thickness of the airfoil. In most of the previous studies, only one of the morphing concepts defined above has been applied. However, the combination of several morphing concepts could be more advantageous to gain better aerodynamic efficiency during the mission. From Figure 2.1 it could be seen that sweep and span combinations have been used in morphing studies since 2006 [7].

Although shape changing components such as retractable flaps and slats, retractable landing gears, variable incidence noses have been used for aircraft in the past, nowadays more significant morphing capabilities such as changes in airfoil camber and wing surface area are aimed thanks to the development in smart materials and adaptive structures [5].

































1903	1931	1931	1932	1937	1947	1951
						
Wright Flyer <i>Twist</i>	Pterodactyl IV <i>Sweep</i>	MAK-10 <i>Span</i>	IS-1 <i>Bi-to monoplane</i>	LIG-7 <i>Chord</i>	MAK-123 <i>Span</i>	X 5 <i>Sweep</i>
1952	1964	1964	1966	1967	1967	1969
						
XF10F <i>Sweep</i>	F 111 <i>Sweep</i>	XB 70 <i>Span bending</i>	Su 17 IG <i>Sweep</i>	MIG 23 <i>Sweep</i>	SU 24 <i>Sweep</i>	Tu 22 M <i>Sweep</i>
1970	1972	1974	1974	1979	1981	1985
						
F 14 <i>Sweep</i>	FS 29 <i>Span</i>	B 1 <i>Sweep</i>	Tornado <i>Sweep</i>	AD 1 <i>Obliquing</i>	Tu 160 <i>Sweep</i>	AFTI/F 111 <i>M.A.W.</i>
1993	1994	2001	2002	2003	2004	2005
						
FLYRT <i>Span</i>	MOTHRA <i>Camber</i>	AAL <i>Pitch</i>	F/A 18 <i>A.A.W.</i>	Virginia Tech <i>Span</i>	Univ. of Florida <i>Twist</i>	Univ. of Florida <i>Gull</i>
2006	2006	2007	2007	2007	2008	2010
						
MFX 1 <i>Sweep & Span</i>	Univ. of Florida <i>Sweep</i>	Virginia Tech <i>Camber</i>	Univ. of Florida <i>Folding</i>	MFX 2 <i>Sweep & span</i>	Delft Univ. <i>Sweep</i>	Virginia tech <i>Camber</i>

Figure 2.1: Timeline of fixed wing aircraft implementing morphing technologies [7]

2.2 Benefits of Morphing

Mission adaptive wings have several advantages. They could expand aircraft's flight envelope by providing multirole capabilities to the aircraft. Morphing wings are designed to perform multiple missions with an optimized aerodynamic performance for each stage of the flight, whereas the aerodynamic performance of conventional control surfaces is optimized for a limited set of flight conditions [8, 9]. Moreover, hinged mechanisms create discontinuities in the wing surface of the traditional aircraft and cause additional drag while there are no discontinuities between the wing and control surfaces in the morphing aircraft. Thereby, aircraft with adaptive wing become

aerodynamically more favorable compared to traditional aircraft.

Changing external aerodynamic loads in an adaptive wing provides less fuel consumption. According to NASA Dryden Studies, in the US wide body transport aircraft would save \$140 million (at a fuel cost \$0.70 per a gallon) in one year with 1% reduction in airfoil drag [10]. Moreover, as a consequence of fuel saving in the mission adaptive aircraft, the spread of harmful gases to the environment is minimized.

Enhancing confidentiality of the military aircraft is also possible with the morphing technologies. Radar signature and visibility of the aircraft could be reduced due to lack of sharp edges and deflected surfaces on the mission adaptive wings. Also, since variable geometry aircraft have heavily distributed actuators, sufficient robustness could be provided against potential actuator failure [11].

Besides all the benefits mentioned above, several problems like shock waves during transonic region of the flight, turbulence, flow separation, vortices and flutter could be overcome by adapting the wing shape accordingly. Many studies aiming to deal with those problems are being carried on [12].

2.3 Drawbacks of Morphing

As well as morphing aircraft have several benefits, they also have some disadvantages. One of the drawbacks of large shape changing is a potential weight increase due to complexity of the morphing aircraft design [13]. Complexity also causes a cost increase in the production of the designed morphing wing.

Another disadvantage is related to the new design challenges that raise in the manufacture of mission adaptive aircraft. New deformable and adaptive structures are imposed by some requirements such as maintaining the structural integrity and load resistance capability. However, although adaptive and deformable materials exist in different environments, there is no systematic and well-developed methodology to create such morphing structures from these materials [14].

Another challenge is the high actuation forces to provide adequate power to actuators for significant shape changing. Moreover, for morphing wings, aerodynamic loading

and aerodynamic center changes more than those of conventional wings. Therefore, substantial shape changes require also complex control systems.

All the above mentioned problems could be remedied. Progress in lightweight, flexible and redundant materials allow us to reduce the weight of the morphing aircraft. According to Skillen and Crossley [15, 16], developments in the material world may be the solution to maintain the structural integrity under the aerodynamic loading. Moreover, with the help of smart materials and viable structural mechanization concepts, power consumption could be reduced by using distributed actuators for large shape changes [15, 16].

2.4 Adaptive Control Surface Concepts (Camber Variable Wings)

There are various forms of morphing as mentioned before. However, morphing based on camber adjustment is the focus of this study. During a design of a camber variable wing, three methods could be followed. These techniques are conventional hinged mechanisms, smart materials and compliant mechanisms [17]. The conventional hinged mechanism, which is the first and the most commonly used method, could not provide smooth shape changes along the wing surface due to the gap between the control surface and the wing. Smart or intelligent materials are defined by Georges Ackras as “materials that have the intrinsic and extrinsic capabilities, first, to respond to stimuli and environmental changes and, second, to activate their functions according to these changes” [18]. The second technique is based on the use of smart or intelligent materials in the design of a camber variable wing. The compliant mechanism, which can transmit motion and power with its own elastic deformation, is the third camber variation method. This structure is flexible and stiff enough to withstand external aerodynamic loads [17].

Barbarino et al. (2010) proposed a variable camber trailing edge control surface concept made of Variable Geometry Trusses (VGTs) which are defined as a structural truss system having a number of length-adjustable actuated members [19, 20]. The idea of using active truss elements is nothing new however; this study is one of the rare works about Shape Memory Alloys (SMA) rods within VGTs. With this ap-

proach, the high cost and the heavy weight problems arising from using conventional length-adjustable actuated members were eliminated. Moreover, the entire passive and active truss elements were pre-strained and hinged at both ends to allow SMA cyclic actuation, hence only tensile loads could be transferred. In Figure 2.2, upward deflected, downward deflected and undeformed shapes of the control surfaces with SMA truss ribs are shown [19].

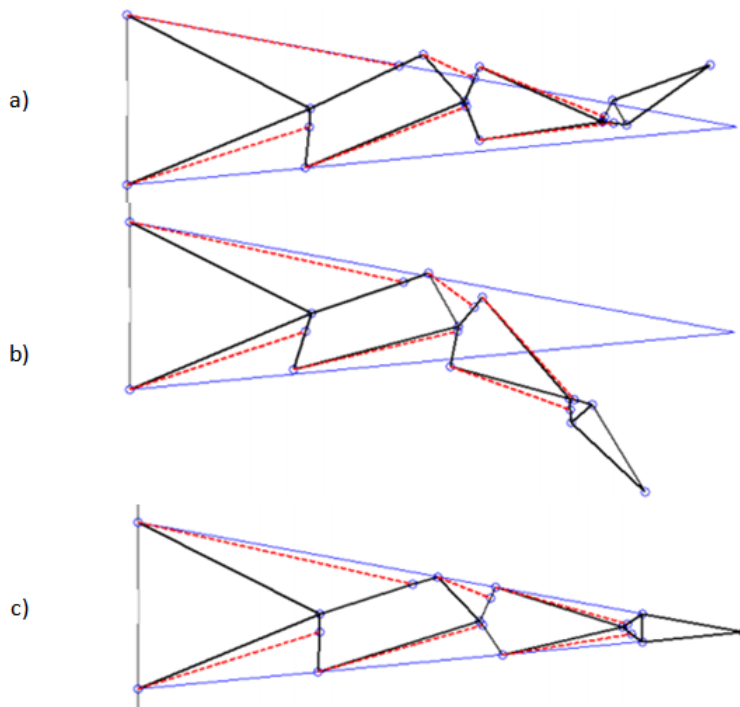


Figure 2.2: Geometry of a sub-optimal morphing truss (red dotted lines represent SMA elements): a) upward deflected, b) downward deflected and c) undeformed [19]

Smart Wing Program is one of the development programs to design morphing trailing edge control surface by using smart structures and materials. This program was funded by Defense Advanced Research Program Agency (DARPA). The trailing edge control surface shown in Figure 2.3 was developed under this program. It was designed as a combination of a flexible honeycomb, a fiberglass laminate as a center leaf of the honeycomb part, an elastomeric (silicone) outer skin and an aluminum tip. In this concept, although the adaptive control surface is exposed to large deformation, the elastomeric outer skin provides a smooth shape change. Additionally, while the flexible honeycomb part increases the resistance to vertical loads, the chord-wise

shape of the control surface is stabilized by the laminate part and aluminum tip [21].

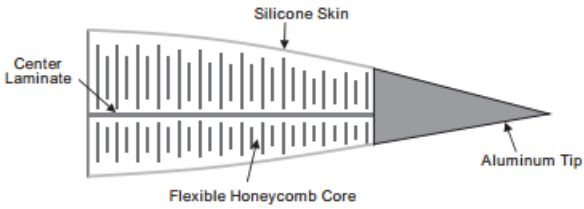


Figure 2.3: Baseline elastomer skin–flexcore control surface structure [21]

Another trailing edge device funded by DARPA is the eccentuator which is a bent beam. It converts the rotary motion into vertical and lateral translation along itself. As indicated in Figure 2.4, the beam is placed and moves between rectangular plates, upper and lower parts of the control surface. The direction of the eccentuator is changed in order to provide downward and upward deflections [22].

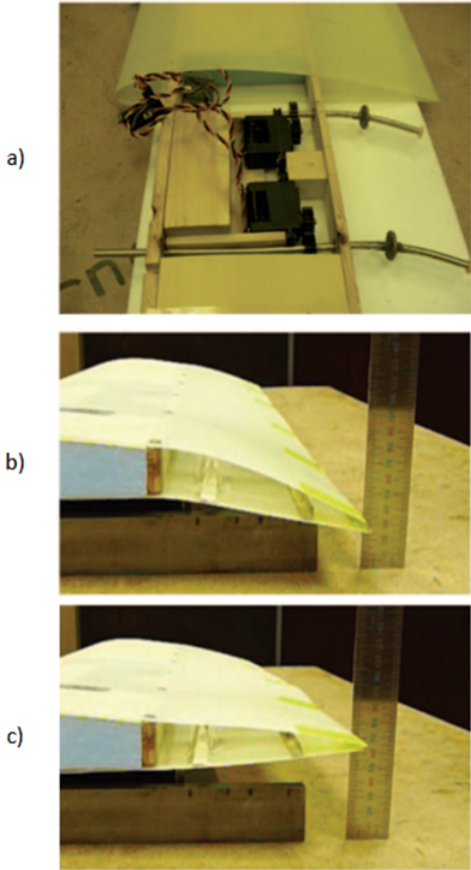


Figure 2.4: The morphing flap with eccentuator device: (a) inner part of the flap (b) downward deflected and (c) upward deflected [22]

Two different concepts for camber variation were investigated within the scope of adaptive trailing edge control surface by the German Aerospace Center (DLR). The first concept shown in Figure 2.5 is known as a finger concept which has a metallic flexible skin and aims achieving a smooth profile during shape change. The name of this concept comes from the separate plate-like elements which are combined with revolute joints used in modeling ribs of the control surface [23]. The ribs are connected with a transmission beam to reduce the number of actuators to be used. As a result, the finger concept control surface deforms like an arc [24]. DLR's second concept is the belt rib concept whose skin was designed like a belt and ribs were modeled like spokes as indicated in Figure 2.6. In this design, by changing the angle of the spokes which connect the upper and lower part of the belt, the desired camber alteration is achieved [25].

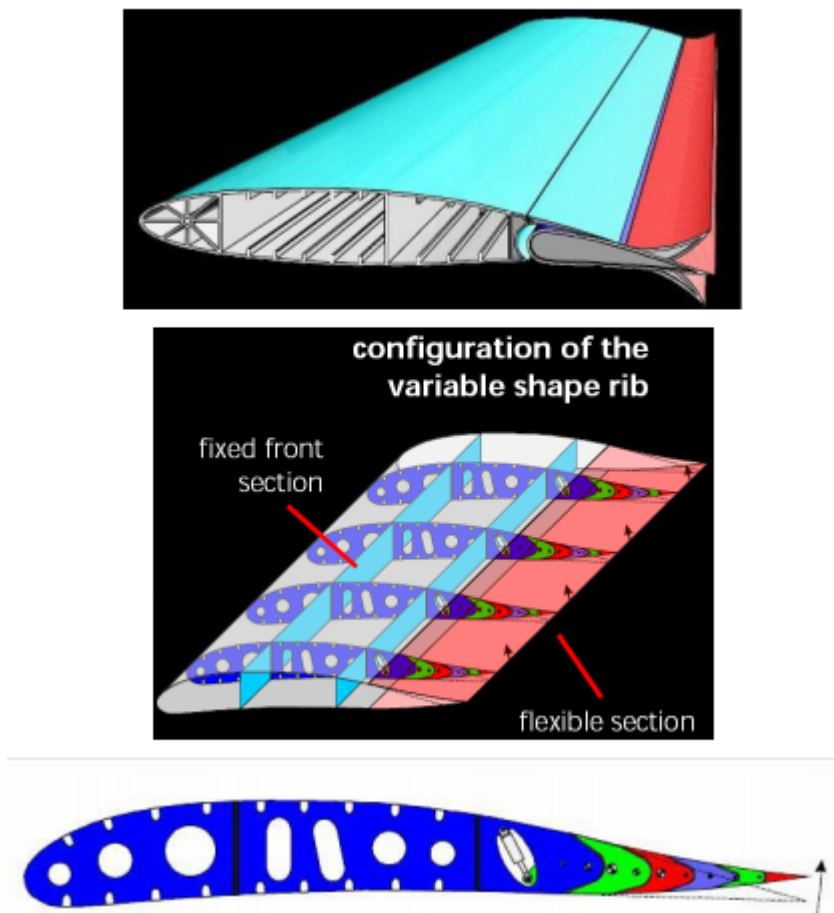


Figure 2.5: DLR finger concept [26]

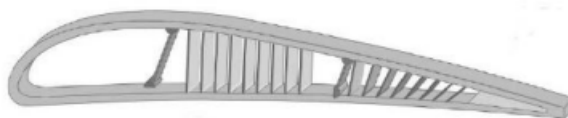


Figure 2.6: DLR belt rib concept [27]

Leading and trailing edge control surfaces were designed to control camber and twist capability in [28] by following a different approach. Two different design concepts were selected with trade-off analysis considering mass, manufacturing, skin and assembly. As a result, a ball linkage mechanism for leading edge and guide plate mechanism for trailing edge surfaces were found suitable among several concepts. Upper skins of both adaptive control surfaces are fixed to the wing, while their lower skins remains unconstrained in-plane motions to provide camber and twist change. The ball linkage system is presented in the Figure 2.7. In this concept, sets of push rods are connected to the spar with ball linkages. It provides acceptable rotation around the fixed end of ball joints for upward deflection and in-plane rotation for twist deformation [28]. Straight guide mechanism selected for the trailing edge adaptive control surface is shown in Figure 2.8. In this system, the lower guide plate acts like a slide bearing with two parallel plates and lower skin of the control surface is connected to it through slots in the skin. The guide plate and sliding joints accommodate the movements of the lower skin to back and forward to deflect the control surface downwards and upwards. Moreover, slots have sufficient margins to allow the side way movements of the lower skin during twist [28].

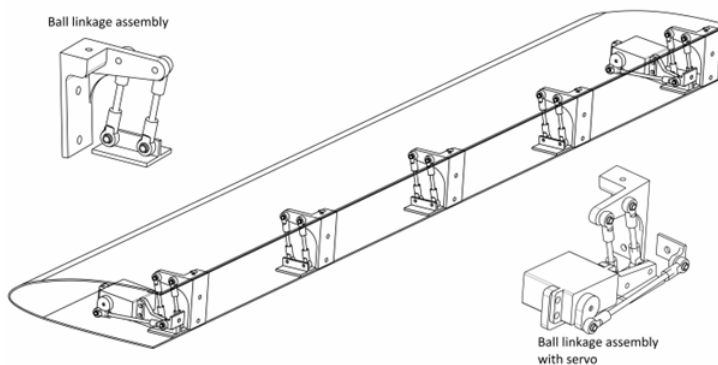


Figure 2.7: Ball linkage mechanism for leading edge control surface [28]

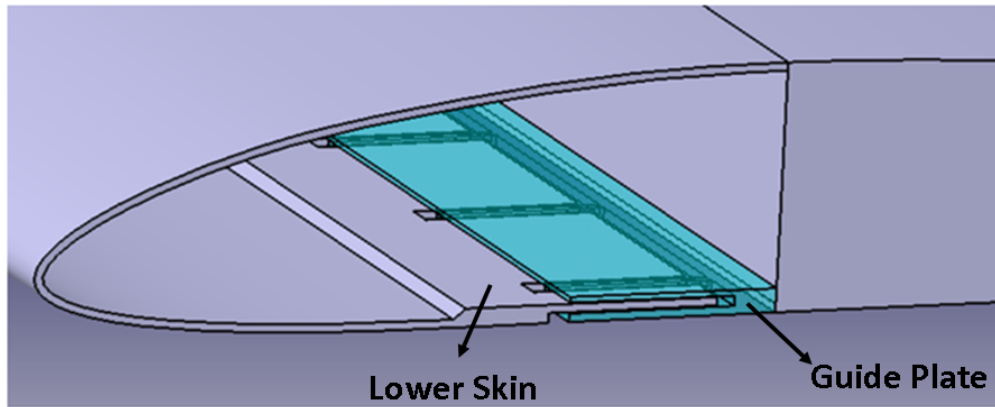


Figure 2.8: Straight guide system for trailing edge control system [28]

An unmanned air vehicle shown in the Figure 2.9 with camber morphing trailing edges was designed in Middle East Technical University [29]. In this concept, the trailing edge control surfaces with semi-open ends are able to change its camber and twist by sliding motion with guide-slide assembly between its upper and lower skin panels. The guide-slide assembly is shown in Figure 2.10 [30]. The air vehicle was manufactured by Turkish Aerospace Industries (TAI) and successful flight tests were also conducted [29].



Figure 2.9: Morphing UAV designed by METU within the scope of TÜBİTAK Project 107M103 [29]

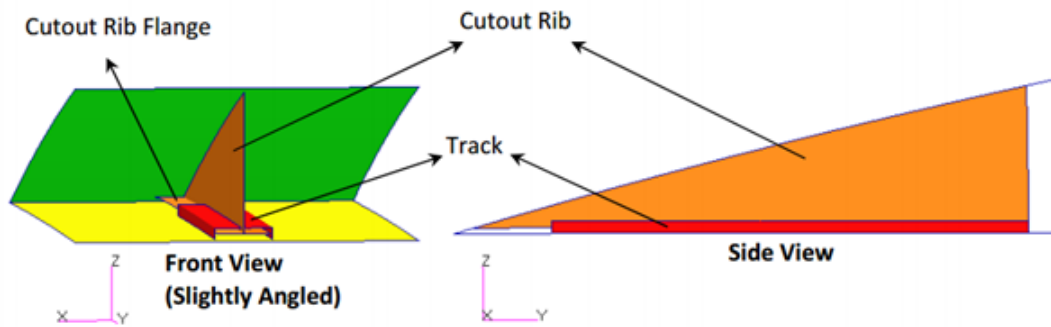


Figure 2.10: The Guide-Slide Assembly of the METU Hingeless Control System [30]

2.5 Materials for Morphing Skin

The most challenging step in developing morphing technologies is to find a convenient flexible material. However, there is limited number of studies related to this aspect of morphing technologies. One of the important investigations was made by [31]. Kikuta, who conducted the mentioned work, explains how the suitable material should achieve the desired efficiency and performance from mission adaptive wings. Firstly, the morphing wing skin material must be deformed easily in chord-wise direction while withstanding the aerodynamic loads in transverse direction. Moreover, the material has to be resistant to weather changing. In addition, the occurrence of the plastic deformation is not intended, when the material undergoes large deformations. Therefore, high strain recovery rate is also one of the desired properties of the plausible skin material. If it could not return to its original form, an additional drag could occur due to profile change.

In [31], polyurethanes, co-polyesters, shape memory materials and woven materials were tested for three different loading condition, namely, uniaxial tensile, biaxial tensile and pressure deflection. When the test results are reviewed, although none of the materials could meet the expectations completely, it was concluded that the best material is Tecoflex®80A, a type of medical thermoplastic polyurethane. Tecoflex®80A has acceptable strain capabilities, however, it could not handle high pressure loads. According to the author, woven materials provide strength to pressure loads, while

polyurethanes provide elasticity to structure. Hence, combining the woven materials like Spandura and polyurethane like Tecoflex could be the way to overcome obstacles to design morphing skins [31].

In the literature there are some satisfactory studies but detailed information about skin materials used in those studies were not presented. One of them is finger concept conducted by DLR. In this study, a flexible metallic skin was used to provide good aerodynamic profile during shape changes. Whereas the materials of the finger elements were represented as metal and carbon fibre reinforced plastic and metal, there was no information about the skin material [32]. Another study handled by DLR is the belt rib concept explained in the previous section. This design was manufactured by using a carbon fibre/epoxy resin composite. Although chord-wise elasticity was compared with standard airfoils, performance of the skin was not addressed [27, 25].

In all the researches about adaptive wing concepts, it is seen that materials do not fulfill completely the necessary requirements. The most challenging problem is combining flexibility and stiffness of the candidate materials. Another problem is that desired capabilities about fatigue, resistance to environmental and chemical changing were ignored during the design process. To conclude, heterogeneous structures with flexible skin materials could be promising in terms of development in the morphing wing designs [33].

CHAPTER 3

PARAMETRIC MODELING OF THE CONTROL SURFACE AND THE DESCRIPTION OF THE OPTIMIZATION PROBLEM

3.1 Introduction

This chapter presents the design of the hybrid trailing edge control surface and the description of the optimization problem. Firstly, the mission profile of the morphing wing possessing a hybrid control surface, and airfoils selected to perform its flight tasks are presented. Then, the dimensions of the control surface, numbers and places of the servo actuators are explained [1]. These design parameters are taken from [1] to concentrate only on materials and dimensions of the control surface in Finite Element Optimization Analysis. The hybrid control surface is created by CATIA V5-6R2012 package software. The fourth part describes the properties of the four different flexible materials used for the compliant part are explained. In the next part, parametric modeling of the each compliant part created by ANSYS Workbench v15.0 package software. Finally optimization procedure conducted by Design Exploration tool of ANSYS Workbench v15.0 software is explained.

3.2 Mission Profile of the Morphing Wing

The base wing geometry and trailing edge control surface studied in this thesis are shown in Figure 3.1. Baseline airfoil of this wing is defined as NACA 6510 and has no twist along its span. Moreover, it has no discontinuities at the intersection edge of the upper and lower skin at the trailing edge. Generic dimensions of the wing and the trailing edge control surface are shown in Table 3.1.

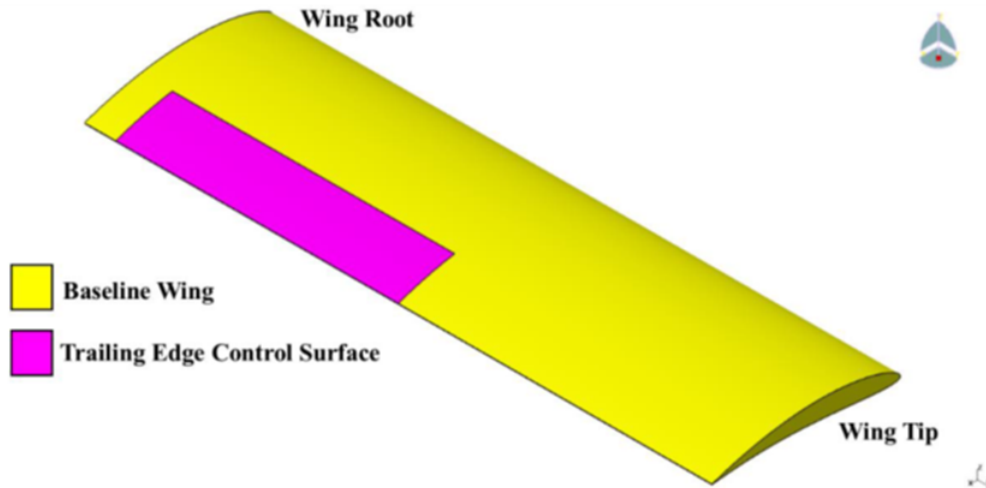


Figure 3.1: The base wing geometry and the trailing edge control surface [1]

The target mission profile of the morphing unmanned aerial vehicle is presented in Figure 3.2. Other profiles, NACA 2510 and NACA 3510, are obtained by the shape modification of the NACA 6510 base profile to perform the desired tasks during the flight. In Figure 3.3, NACA airfoil profiles and corresponding flight missions are represented.

Table 3.1: Dimensions of the morphing wing and trailing edge control surface

Wing Chord [mm]	600
Wing Span [mm]	2000
Control Surface Chord [mm]	180
Control Surface Span [mm]	900

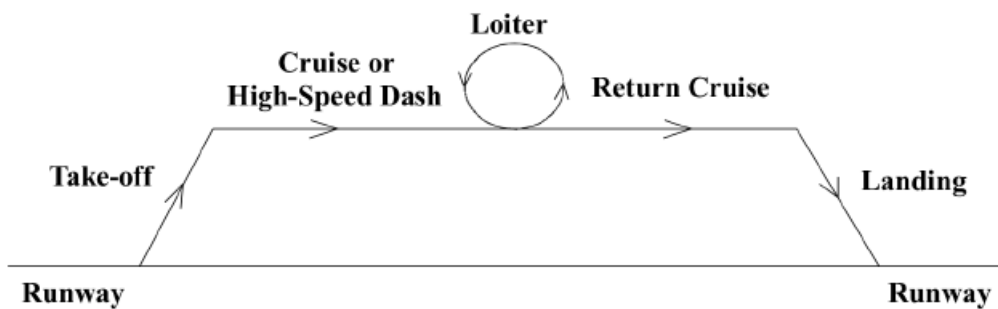


Figure 3.2: The mission profile of the morphing unmanned aerial vehicle [1]

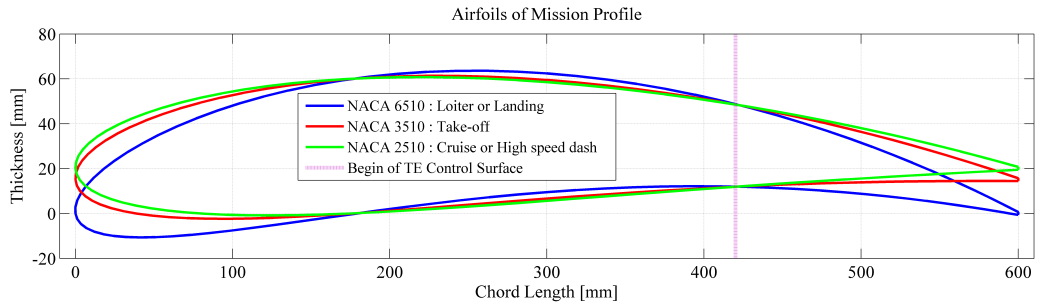


Figure 3.3: NACA airfoils and corresponding flight missions of Morphing Wing

3.3 Design of the Hybrid Trailing Edge Control Surface

In this section, background information about the design of the hybrid control surface is given. Two different designs of the hybrid trailing edge control surface are considered in this study. First of them is a closed cell design which has no gap in the transmission section of the rigid part as shown in Figure 3.4. The second called as open cell design which has an open section at the transmission part shown in Figure 3.4.

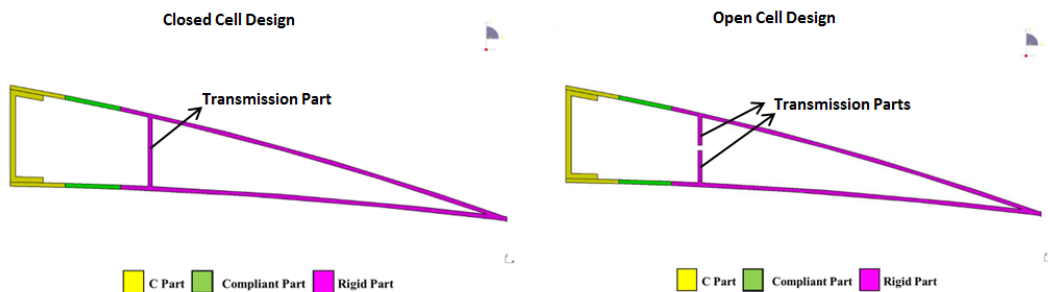


Figure 3.4: Closed and open cell designs of hybrid control surface with transmission parts [1]

These two designs contain same parts, namely a C part, a compliant part and a rigid part as shown in Figure 3.4. The C part includes three sub-sections that are C bar part, lower and upper skin parts. This part provides the connection between the wing and the control surface. Another common part of closed and open cell control surfaces is the compliant part which is made of a flexible material. The transition between NACA profiles can be achieved with deformation of the flexible material. To reach

the NACA 3510 and NACA 2510 profiles, baseline airfoil shape, NACA 6510, deflects upwards with the servo actuators selected by [1]. This is achieved by applying different actuation rotations to the upper and lower actuators such that compliant parts stay always in tension. This is needed to avoid any slacking in the compliant part which may disrupt the flow during the flight. It is assumed that the flexible skins are bonded to the other parts by adhesives. The last part of the control surface is the rigid part which is slightly different for closed cell and open cell designs as can be seen in Figure 3.4. These parts are made of aluminum and include transmission parts on themselves.

Design thicknesses and used materials of the hybrid control surface are presented in Table 3.2. These properties have already decided in [1]. However, in this thesis, different thicknesses, lengths and elastic materials are examined for the upper and lower compliant parts to make an optimum design. The properties of the C part and rigid part are taken directly from Table 3.2 and are not modified, while thickness of the compliant part is taken as initial condition for the optimization study. Material properties of aluminum shown in Table 3.3 are taken from ANSYS Material Library and they are very close to properties of Aluminum 6061-T6 material [34, 35].

Table 3.2: Dimensions and materials of the hybrid trailing edge control surface

	C Part		Compliant Part	Rigid Part
	C Bar Part	Skin Parts		
Material	Aluminum	Aluminum	Neoprene Rubber	Aluminum
Thickness [mm]	2.0	1.5	1.5	1.5

Table 3.3: Material properties of aluminum [34]

Density, ρ [kg/m ³] :	2770
Young's Modulus, E [GPa] :	71
Poisson's Ratio, ν [-] :	0.33
Tensile Yield Strength [MPa] :	280
Compression Yield Strength [MPa] :	280
Tensile Ultimate Strength [MPa] :	310

In this study, servo actuators are located inside the control surface and connected to the C part. It is difficult to find a servo actuator that can both fit inside the control surface and provide the required torque to morph the control surface. Volz DA 13-05-60 servo actuator is chosen with a research on the internet markets in [1]. The moment arm, actuation rod, C part connector and their full assembly with the selected servo actuator are given in Figure 3.5. Moreover, the specifications of the servo actuator Volz DA 13-05-60 are given in Table 3.4 [36]. Besides, length and radius of actuation rods are defined as 34.5 mm and 1.25 mm, respectively.

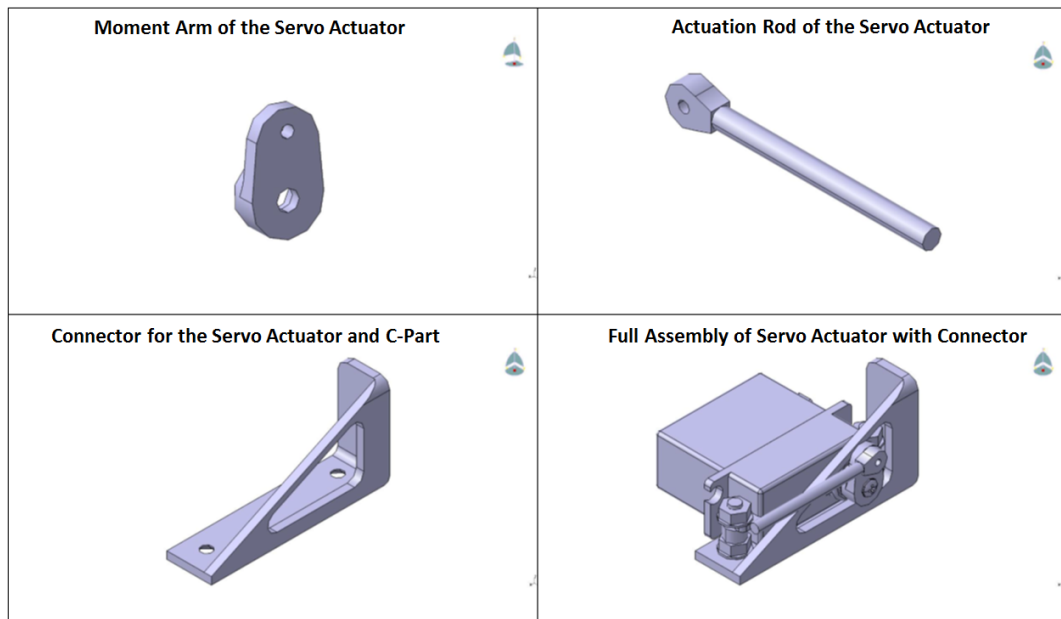


Figure 3.5: Moment arm, designed actuation rod, C part connector of Volz DA 13-05-60 servo actuator and full assembly of them [36] [1]

Table 3.4: The specifications of the servo actuator [36]

Operating Voltage [V]	5
Stall Torque [N-mm]	600
Weight [gr]	19
Dimensions [mm]	28.5 x 28.5 x 13

In this thesis, by using the selected servo actuator it is decided that two servos for the upper part and two servos for the lower part of the control surface are used. Locations

of these servos which have been studied in [1] are presented in Figure 3.6 from top view and Figure 3.7 from side view. However, only the moment arms and actuation rods are modeled in ANSYS, due to the complexity of servos. By this way, rotations are applied to the moment arm and motion of the control surface is provided.

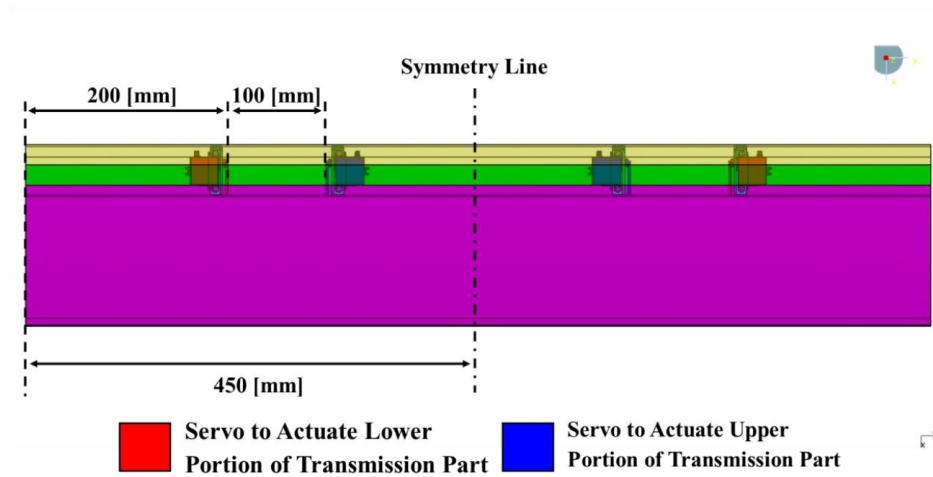


Figure 3.6: Placement of the servo actuators (top view) [1]

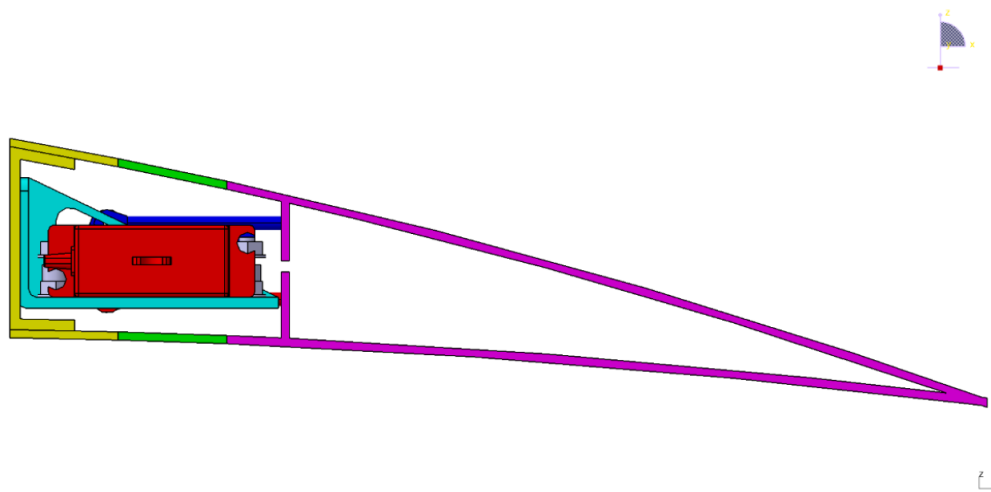


Figure 3.7: Placement of the servo actuators (side view) [1]

3.4 Input Parameters of Compliant Part Optimization

In this section, the parameters that enter into the optimization study conducted by Direct Optimization method of ANSYS v15.0 Design Exploration tool, are explained.

Dimensions of the compliant part and rotation angles to deflect control surface can be defined as parametric inputs. However, types of the materials cannot be inserted as parametric property in ANSYS. Therefore, optimization procedure is followed separately for the each of the four materials considered.

3.4.1 Materials of the Compliant Part

In this study, motion of the control surface is achieved by axial deformation of the compliant part. For this reason, the most important property of the materials used in the compliant part is the axial deformation behavior. Polymeric materials have the ability of undergoing large deformations under small loads. Moreover, many of them can retain their original shape after applied loads are removed. Therefore, they seem suitable to be used in the compliant part of the hybrid trailing edge control surface [37].

In ANSYS, several hyperelastic material models are available. In order to select the most suitable material model, hyperelastic curve fitting tool is used. This tool estimates the material coefficients for different hyperelastic models from the engineering stress-strain curves that can be imported to ANSYS. ANSYS also provides some example test data for uniaxial, biaxial and shear tests. Material curve fitting tool provides a comparison of the test data and the fit computed by the program.

In this thesis, four different hyperelastic materials are used for the compliant part of the control surface. These are neoprene rubber, sample elastomer-1, sample elastomer-2 and silicone. The first three materials are available in ANSYS material library. In ANSYS the uniaxial, biaxial, shear and volumetric test data are available for neoprene rubber [34]. The best fit to the test data of neoprene rubber is obtained with Neo-Hookean hyperelasticity model. Therefore, this model is selected from ANSYS hyperelastic tool and material constants of the model are obtained. The second material from ANSYS database is sample elastomer-1 which is designated to be used with Ogden material model. Uniaxial and shear test data are available for this material [34]. First order Ogden material model provides the best fit to the given test data. The third material from ANSYS database is sample elastomer-2 which is designated to be used with Neo-Hookean material model [34]. Neo-Hookean model is

used and the material parameters are obtained by fitting the test data. The fourth material is the silicone which is provided by INVENT Company, one of the project partners, from Germany [38]. Uniaxial test of this material was conducted at METU Aerospace Engineering Structure Laboratory. The uniaxial test data was imported to ANSYS Engineering Data tool and best fit was achieved for Ogden 1st order non-linear material model. In Figure 3.8, the uniaxial test data of the four materials and the corresponding fits are presented. Density information is not given for the materials taken from ANSYS library. Moreover, the density of silicone was not provided by INVENT. The density of neoprene rubber was found from literature as 1250 kg/m^3 [39]. Therefore, the densities were set to this value for all four materials.

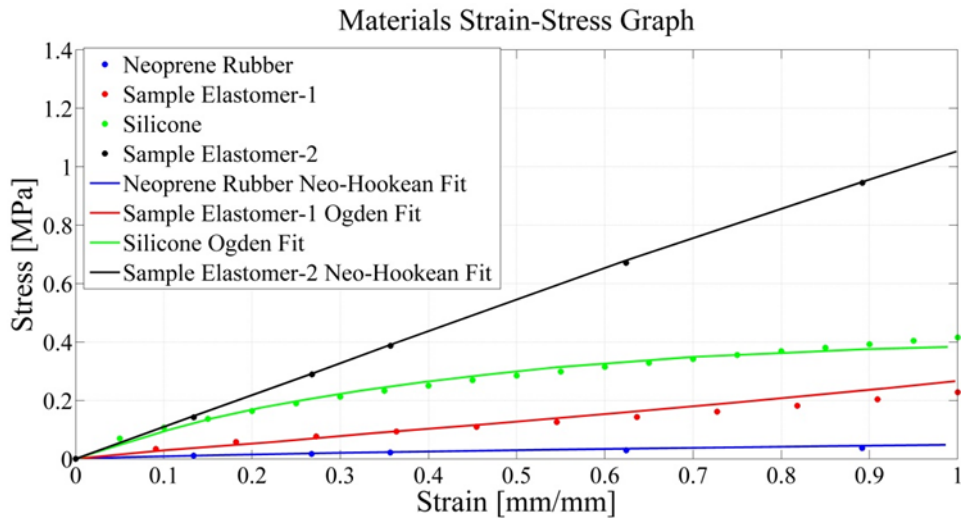


Figure 3.8: The uniaxial test data of the hyperelastic materials and their curve fit data

The initial shear modulus (μ) and the incompressibility parameter (d) of the materials (neoprene rubber and sample elastomer-2) are obtained with Neo-Hookean hyperelasticity model. By using Ogden 1st order hyperelasticity model, material constants (μ_1 and α_1) and the incompressibility parameter (d_1) of the materials (sample elastomer-1 and silicone) are also achieved. The material constants obtained by using Ogden 1st order model (μ_1 and α_1) are used to calculate the initial shear modulus of the materials. These material constants are given in the Table 3.5.

Table 3.5: Material constants of the hyperelastic materials

Materials	Hyperelastic Material Model	Material Constants		
		μ [Pa]	d [1/Pa]	
Neoprene Rubber	Neo-Hookean	$2.71 \cdot 10^4$	$1.44 \cdot 10^{-7}$	
Sample Elastomer-2	Neo-Hookean	$5.04 \cdot 10^5$	0	
		Material Constants		
		μ_1 [-]	α_1 [-]	d_1 [1/Pa]
Sample Elastomer-1	1 st order Ogden	$6.33 \cdot 10^4$	3.14	0
Silicone	1 st order Ogden	$3.05 \cdot 10^8$	$2.43 \cdot 10^{-3}$	0

3.4.2 Dimensions of the Compliant Part

Since the dimensions of the compliant parts of the trailing edge geometry are not fixed, they are modeled parametrically. The lengths of upper and lower compliant parts are two parametric geometric dimensions. Note that while the compliant parts (L_u and L_l) are extended, the rigid parts (r_u and r_l) are shortened or vice versa, and the total lengths (L_u+r_u and L_l+r_l) of the rigid and compliant parts remain equal. Moreover, the thicknesses of both lower and upper compliant parts (t_u and t_l) are able to change independently in finite element analysis. Figure 3.9 presents the parametric geometric dimensions of the compliant parts. C-part of the hybrid control surface is not modeled because it is known that it is very rigid and there is no significant effect of C-part on the results of FEA from the previous experiences [1].

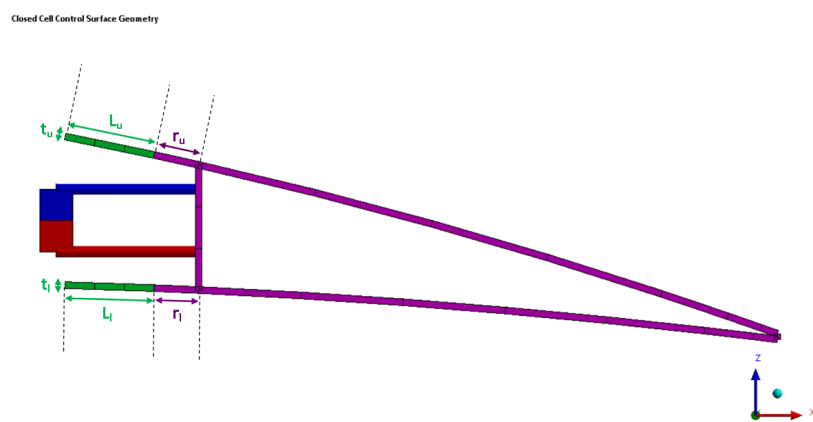


Figure 3.9: The parametric inputs of the control surface

3.4.3 Rotation Angles Inputs to the Servo Actuators

In this optimization study, the ultimate goal is to morph the trailing edge from NACA 6510 base profile to NACA 3510 and 2510 profiles with servo actuator torques as small as possible. As it can be seen from Figure 3.3, NACA 2510 profile is deflected upward more than NACA 3510 profile. For this reason, it is natural that transforming control surface from base to NACA 2510 profile requires more torque. Therefore, compliant part optimization is conducted for the finite element analysis of morphing from NACA 6510 to NACA 2510 profile. Afterwards only the rotations of the moment arms of the servo actuators are set as optimization input parameters for the analysis of deflection to NACA 3510 airfoil shape. Other input parameters, which are the dimensions and materials of the compliant parts, are taken from the previous optimization result. In the optimization problem lower and upper limits are set for the optimization variables. Lower and upper limits of input parameters are the same in the closed and open cell control surface designs, except the rotation angles of the moment arms due to the design differences of the transmission part. In Figure 3.10, it can be seen that points A and B are the moment arms of the servo actuators which actuate respectively the lower and upper parts of the control surface. Point C is constrained to the rotations of point A, while point D is constrained to the rotations of point B along all direction in ANSYS Mechanical. Therefore, the rotation angles read from points C and D are the same as the rotation angles of points A and B, respectively. The constraint equations are given in (3.1)-(3.2). In these equations the term R_{y_A} describes the rotation of point A around y axis. Rotations around x and z axes the rotations are set to zero for points A, B, C and D.

$$R_{y_A} - R_{y_C} = 0 \quad (3.1)$$

$$R_{y_B} - R_{y_D} = 0 \quad (3.2)$$

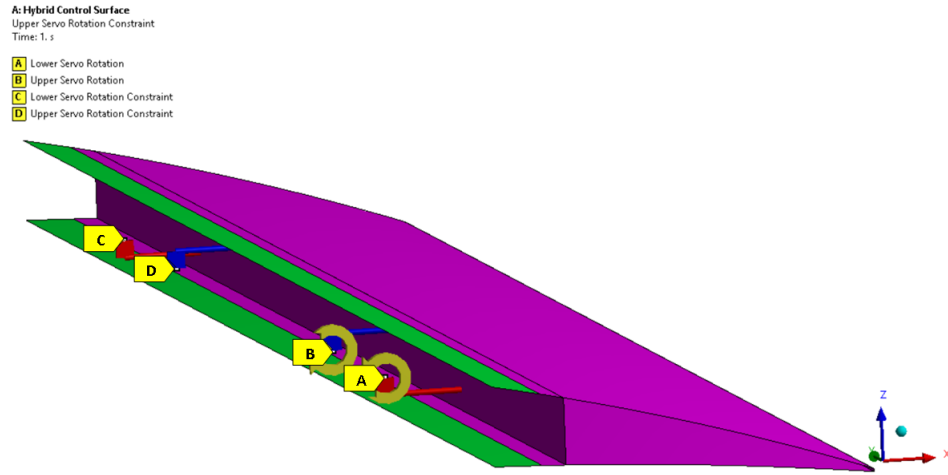


Figure 3.10: The points where moment arm rotation angles applied on the control surface

Table 3.6: Continuous input parameters of the optimization study

	Explanation	Design	Initial Value	Lower Bound	Upper Bound
L_u [mm]	Length of Upper Compliant Part	Open and Closed Cell	20.42	3.00	25.00
L_l [mm]	Length of Lower Compliant Part	Open and Closed Cell	20.01	15.00	25.00
t_u [mm]	Thickness of Upper Compliant Part	Open and Closed Cell	1.50	1.00	2.00
t_l [mm]	Thickness of Lower Compliant Part	Open and Closed Cell	1.50	1.00	2.00
R_{yu} [degree]	Rotation of Servo Actuators to Actuate the Upper Compliant Part	Open and Closed Cell	18.00	16.20	19.80
R_{yl} [degree]	Rotation of Servo Actuators to Actuate the Lower Compliant Part	Closed Cell	-32.50	-35.75	-29.25
		Open Cell	-35.00	-38.50	-31.50

All the input parameters of the optimization study and their initial, lower and upper

limits are presented in Table 3.6. These inputs are defined as continuous parameters and entered to the Direct Optimization Tool of the ANSYS. How the tool works is explained in Section 3.5. Initial values of all parameters are selected from [1] such that they morph the control surface from NACA 6510 to NACA 2510 base profile. In order to achieve morphing the control surface to the NACA 3510 and NACA 2510 profiles, the upward tip deflection of the control surface in z-direction must be 15.2 mm and 20.2 mm, respectively. In total eight discrete optimization studies are conducted to achieve the NACA 2510 profile from NACA 6510 profile for four different materials and two different (open cell and closed cell) designs.

3.5 Objective and Constraints of Compliant Part Optimization

In this part, objectives and constraints of the optimization process are explained. The first and the most important objective is to achieve the 20.2 mm tip deflection for the control surface which corresponds to change from base NACA6510 profile to NACA 2510. For this reason, importance of the objective is set to 'higher' in ANSYS Direct Optimization tool. The meaning of the 'higher' is explained in Section 3.6.

Second objective is to minimize the required torques of the servo actuators which actuate the upper and lower compliant parts of the control surface. It is also primary objective due to the physical limits of the servo actuators used. To this end, maximum torques are limited to 1200 Nmm and constraint handling is adjusted as 'strict'. The meaning of the 'strict' is also explained in Section 3.6. Constrained value of the torque of the servo actuator is twice of the limit servo torque presented in Table 3.4. This is due to the fact that the rotations of servos are constrained to each other and the moment reactions obtained from the program corresponds to the reaction of two actuators.

Another significant point is that the compliant part must not be subjected to compression during the flight. In other words, chordwise normal strains in upper and lower compliant parts must be positive. In order to compute chordwise (x direction of the local coordinate systems) normal strains of upper and lower compliant parts two local coordinate systems are generated as shown in Figure 3.11. Moreover, maximum

chordwise tensile strains in the compliant parts are limited to 1.

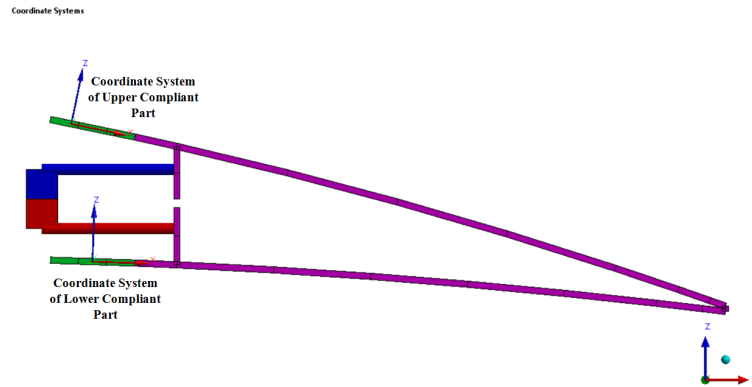


Figure 3.11: The coordinate systems of the upper and lower compliant parts

Finally, the last constraint of the optimization is about the moment arms and actuation rods of the servo actuators which are modeled with aluminum beam elements. To this end, maximum stress in the beams are limited to yield strength of aluminum. ANSYS gives two combined stress values, namely, the maximum combined stress and the minimum combined stress. The maximum and the minimum combined stresses are calculated by linear combinations of normal stresses caused by axial loads and normal stresses caused by bending moments. Since the yield strength of aluminum is 280 MPa, the maximum and the minimum combined stress values are limited to 280 MPa and -280 MPa, respectively.

The abbreviations used for the output parameters are given in Table 3.7. The objectives and the constraints of the optimization problem are presented in Table 3.8.

Table 3.7: Output parameters and their abbreviations

Output Parameters	Explanation
d_z	Tip deflection in z-direction
Q_l	Torque reaction of the servo to actuate the lower part
Q_u	Torque reaction of the servo to actuate the upper part
ϵ_{lmin}	Minimum normal elastic strain of the lower compliant part
ϵ_{umin}	Minimum normal elastic strain of the upper compliant part
ϵ_{lmax}	Maximum normal elastic strain of the lower compliant part
ϵ_{umax}	Maximum normal elastic strain of the upper compliant part
σ_{cmin}	Minimum combined stress of the beams
σ_{cmax}	Maximum combined stress of the beams

Table 3.8: Objectives and constraints of the optimization study

Output Parameters	Objective		Constraint		
	Type	Target	Type	Lower Bound	Upper Bound
d_z [mm]	Seek Target	20.20	—	—	—
Q_l [Nmm]	Minimize	—	Values \leq Upper Bound	—	1200
Q_u [Nmm]	Minimize	—	Values \leq Upper Bound	—	1200
ϵ_{lmin} [-]	—	—	Values \geq Lower Bound	0	—
ϵ_{umin} [-]	—	—	Values \geq Lower Bound	0	—
ϵ_{lmax} [-]	—	—	Values \leq Upper Bound	—	1
ϵ_{umax} [-]	—	—	Values \leq Upper Bound	—	1
σ_{cmin} [MPa]	—	—	Values \geq Lower Bound	-280	—
σ_{cmax} [MPa]	—	—	Values \leq Upper Bound	—	280

3.6 Optimization Theory and Procedures

In this section, Goal Driven Optimization tool of ANSYS and its operation procedure are introduced. It uses two different types of optimization techniques, namely Direct Optimization and Response Surface Optimization methods. Response surfaces describe output parameters in terms of input parameters with different approaches. They generate approximate output values and do not analyze the complete problem. Therefore, they are not always very accurate. Since the quality of the response surface directly affects the results of Response Surface Optimization, Direct Optimization method is preferred in this study.

Direct Optimization is a part of Design Exploration tool of ANSYS 15 Workbench. It can further use several methods for the solution of the multiple-objective optimization problems. These are Screening, Multi-Objective Genetic Algorithm (MOGA) and Adaptive Multiple-Objective (AMO) methods. Among these methods, AMO calcu-

lates the results iteratively and provides a more refined approach than the Screening Method that can be used for the preliminary design. Also, AMO Method uses the same technic with MOGA. However, it evaluates the results with Kriging error predictor and it reduces the necessary time to obtain an optimum. Therefore, in the optimization of the compliant part of the hybrid control surface, AMO is used [40].

The Multi-Objective Genetic Algorithm (MOGA) which is included in AMO method is an iterative optimization method. This method ranks the design points by using Non-dominated Sorted Genetic Algorithm-II (NSGA-II) as non - dominated and dominated. The non - dominated design points generate the Pareto front which is a convergence criterion. The process that MOGA uses to create a new population consists of two main steps which are crossover and mutation after sorting the design points by using NSGA-II. Crossover combines two chromosomes (parents) to produce a new chromosome (child). This stage may provide better chromosome than the parents. Mutation changes the value of one or more genes. This may result in the insertion of entirely new gene values into the gene pool. Moreover, it helps to find a global optima [40].

Kriging is a multidimensional interpolation method. In Kriging metamodel, response value of an unobserved point is globally estimated by a known polynomial and a random departure from the polynomial. It is represented by Equation (3.3) as follows [41]:

$$y(x) = f(x) + Z(x) \quad (3.3)$$

where:

$y(x)$ = the unknown function of interest,

$f(x)$ = a polynomial function of x ,

$Z(x)$ = the realization of normally distributed Gaussian random process with mean zero, variance σ^2 , and non-zero covariance.

Predicted error of an estimated response value for each design point can be obtained as a by-product with Kriging response surface model. Using this predicted error, as long as it is determined that the domination status (non-dominated and dominated)

of design points in the current generation is not changed because of using Kriging response, it is acceptable to use the Kriging model instead of analysis of this point by real solvers. Using Kriging response value makes the optimization faster, due to less computation in the solver. If the domination status is changed, then the design points are analyzed with real solvers [41].

Multi-objective problems involve two or more minimizing and maximizing objective functions together with constraints functions. Formal definition of multi-objective optimization problem is stated by Equation 3.4 as follows [[42]:

$$\begin{aligned}
& \min \text{ or } \max F(x) = [f_1(x), f_2(x), \dots, f_M(x)] \\
& \text{subject to } G(x) = [g_1(x), g_2(x), \dots, g_J(x)] \geq 0 \\
& \quad H(x) = [h_1(x), h_2(x), \dots, h_K(x)] = 0 \\
& \quad x_i^{(L)} \leq x_i \leq x_i^{(U)}, i = 1, \dots, N \\
& \text{such that } x \in X
\end{aligned} \tag{3.4}$$

where:

- $x = (x_1, x_2, \dots, x_N)^T$ is the vector of the N decision variables,
- M is the number of objectives f_i ,
- J is inequality and K is equality constraints,
- $x_i^{(L)}$ and $x_i^{(U)}$ are the lower and upper bound for each decision variables x_i , respectively and,
- X is the feasible set of decision vectors.

The feasible set is defined by some constraint functions ($G(x)$ and $H(x)$) and this set constitutes a feasible design variable space. In multiple objective optimization studies, there is M -dimensional objective space. For each x in the decision variable space X , there exists a point in the objective space Z denoted by z . In Figure 3.12, the decision space and the objective space are shown [42].

A vector $x^* \in X$ is called a feasible solution (feasible decision) and a vector $z^* \in Z$ which corresponds to the feasible solution (x^*) is called an objective vector (out-

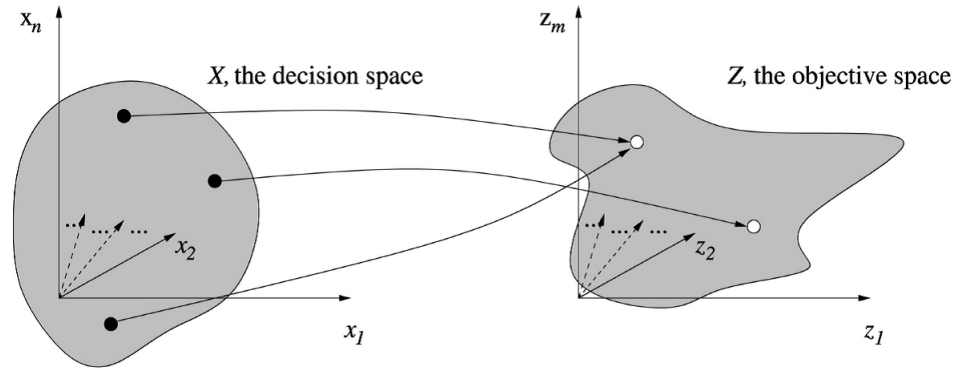


Figure 3.12: The decision space and the objective space in multi-objective optimization problems [42]

come). In multi-objective optimization problems, there are generally conflicting points between best solutions for each objective. Therefore, there is not usually a single best point for all objectives and constraints. In this case, instead of only one best solution, a group of non-dominated set becomes optimal design point for all the objectives together, not favoring only one of them. The non-dominated set is named as Pareto Optimal. If both the following conditions are true, solution x^1 is designated as Pareto Optimal [42]:

1. The solution x^1 is no worse than x^2 in all objectives,
2. The solution x^1 is strictly better than x^2 in at least one objective.

The set of Pareto Optimal outcomes $f(x^1)$ is called as Pareto front or non-dominated front. In order to explain the Pareto Front more clearly, Figure 3.13 shows the objective space of two minimizing functions, (f_1 and f_2). The circles show the corresponding outcome of the solutions (x_n). Yellow circle represents an unattainable best solution. Gray circles are not on the Pareto Front, because they are dominated by blue circles. Blue circles are not strictly dominated by any other, therefore they lie on the Pareto (non-dominated) front. Maximum Allowable Pareto Percentage is a convergence criterion, which represents the ratio of the number of Pareto fronts to the number of samples per iteration, in this thesis [40].

After optimization analysis is finished successfully, candidate points, which are the best solutions according to the rating of the Decision Support Process of ANSYS,

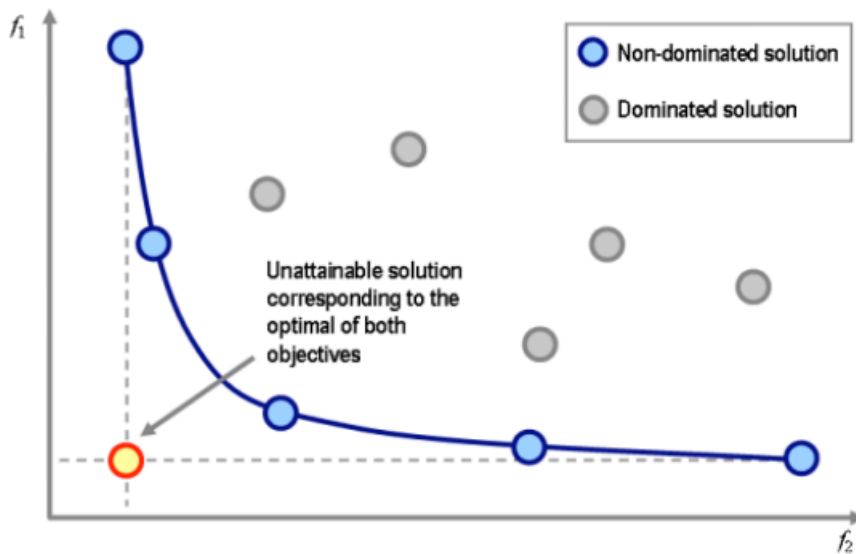


Figure 3.13: Example of Pareto front [42]

among a sample set are extracted by ANSYS Direct Optimization tool. For the multiple-objective optimization, the sample set corresponds to the final population of the optimization. The Decision Support Process sorts the points by using a cost function, which takes into account ‘Importance Level’ of objectives and constraints and the ‘Constraint Handling’ properties. In ANSYS different levels of importance can be assigned to defined objectives or constraints. They allow choosing the relative importance of assigned objectives or constraints according to the others. Available options for importance level are ‘default’, ‘higher’ and ‘lower’. Moreover, ANSYS allows specifying the constraint handling with two options, which are ‘relaxed’ and ‘strict’. When the ‘Constraint Handling’ property is set to ‘relaxed’, all unfeasible points are included in the sort. When the property is set to ‘strict’, all unfeasible points are removed from the sort [40].

The workflow of the Adaptive Multiple-Objective optimization method is shown in Figure 3.14. Adaptive Multiple-Objective optimization process is explained step by step as follows:

1. Initial sampling is obtained in order to construct Kriging response surface.
2. Finite Element Analyses are conducted for each sampling.

3. A Kriging response surface based on the first samples are built and improved during the optimization analysis by adding design points.
4. By using the Non-dominated Sorting Algorithm design points are separated as non-dominated and dominated.
5. Non-dominated design points are added to the next population directly. However; dominated design points are combined with non-dominated ones by using genetic operations (crossover and mutation) and by this way next population is created.
6. Each point in population is evaluated using Kriging error predictor. If error for the point is acceptable, step 7 is followed for this approximated point. If it is not, finite element analysis is conducted for this point and it improves the Kriging in order to generate the next population. In addition, step 7 is also followed for this point, together with acceptable design points, to check the convergence of the optimization problem
7. Convergence check for the optimization is performed. If the optimization has been converged, the process stops. It converges when the maximum allowable Pareto percentage have been achieved. If the optimization is not converged, the step 8 is followed.
8. Optimization is validated for whether the stopping criterion has been met or not, although the convergence has not been provided. If the maximum number of iterations has been reached, the process is stopped irrespective of the convergence. If the maximum number of iterations has not been reached, the process returns to step 4.
9. Until the optimization has converged or the stopping criteria have been achieved, the steps from 2 to 9 are repeated.

With the explained target, objectives and constraints in this chapter, eight discrete optimization analyses are conducted for four different materials and two different designs. Each optimization analysis consists of several finite element analyses. In the next chapter, the finite element models of the control surface designs and optimization analyses are presented.

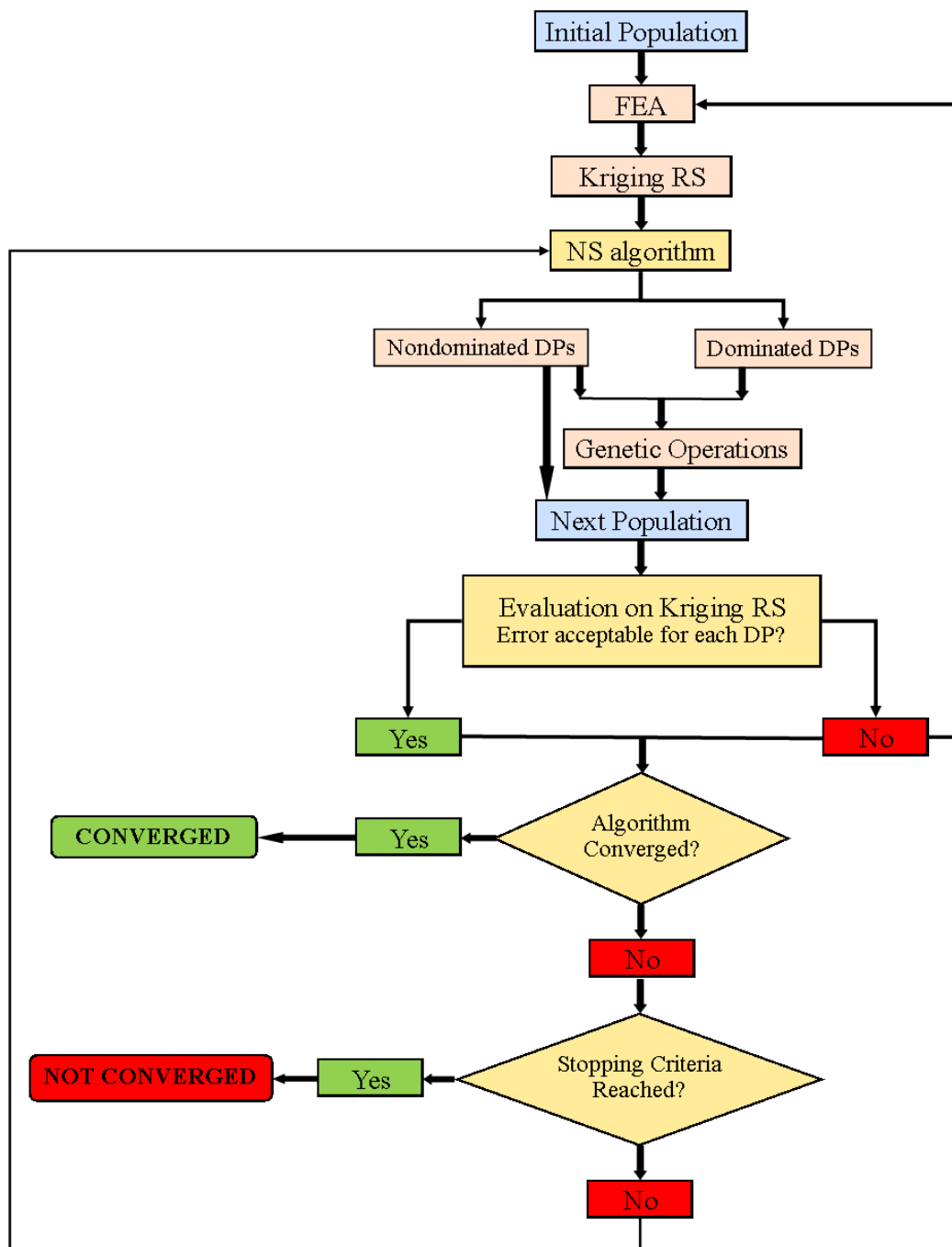


Figure 3.14: The workflow schema of the Adaptive Multiple-Objective optimization method

CHAPTER 4

STRUCTURAL ANALYSES AND OPTIMIZATION OF THE COMPLIANT PARTS OF THE CONTROL SURFACE IN-VACUO CONDITION

4.1 Introduction

In this chapter, finite element analyses of open cell and closed cell hybrid trailing edge control surface designs are presented. These analyses are conducted by using ANSYS v15.0 Static Structural module. After generation of the finite element models, optimization analyses of the compliant parts of the hybrid trailing edge control surface are conducted with Direct Optimization module of ANSYS v15.0 Design Exploration tool. In this chapter, analyses are conducted only in-vacuo condition, without aerodynamic loads.

In the first part, generation of the finite element model of the control surface designs is explained in detail. In the second part, the inputs which entered to the Direct Optimization tool are given. In the third section, candidate design points for designing the compliant parts are presented for the open and closed cell hybrid control surface designs for morphing from base profile to NACA 2510 profile. Finally, the selected design among the candidates is structurally analyzed for morphing the control surface from base profile to NACA 3510 profile and the results are presented.

4.2 Finite Element Model of the Hybrid Control Surface

In this section, generation of finite element models of the hybrid trailing edge control surface for the open and closed cell designs are explained. Information about geome-

tries, boundary conditions, inputs and analysis settings for the finite element analyses are given.

4.2.1 Finite Element Model of the Open Cell Control Surface

The finite element model of the open cell hybrid control surface is given in this part. Figure 4.1 shows the dimensions of the open cell control surface design. The yellow part, named as C part, is not modeled in ANSYS Static Structural module in order to simplify the model. This open cell control surface geometry is modeled in CATIA V5-6R2012 and imported to the ANSYS Static Structural tool Design Modeler part. Imported geometry is shown in Figure 4.2 from isometric view and in Figure 4.3 from side view. The moment arms and actuation rods of the servo actuators are shown as lines in these figures.

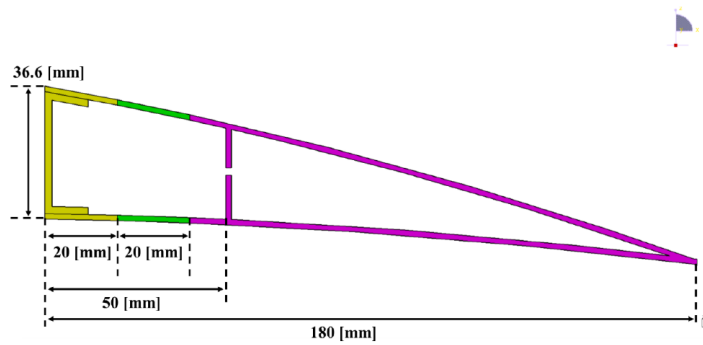


Figure 4.1: General dimensions of the open cell control surface design [1]

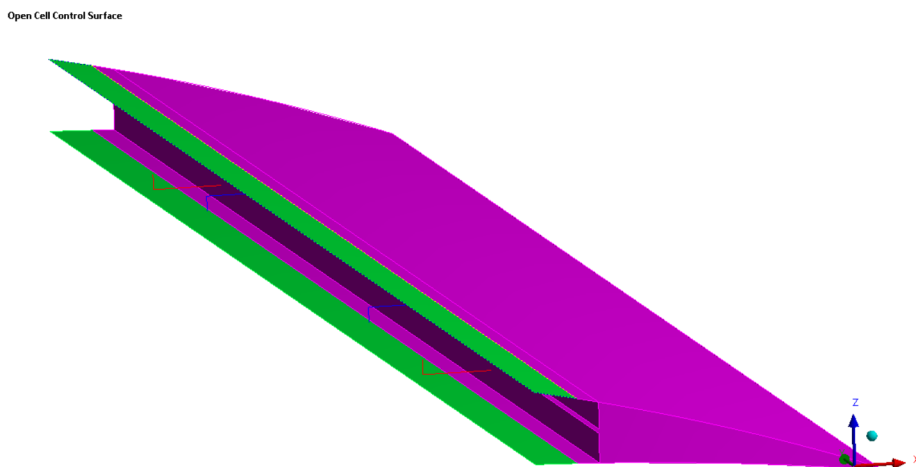


Figure 4.2: Isometric view of the open cell hybrid control surface

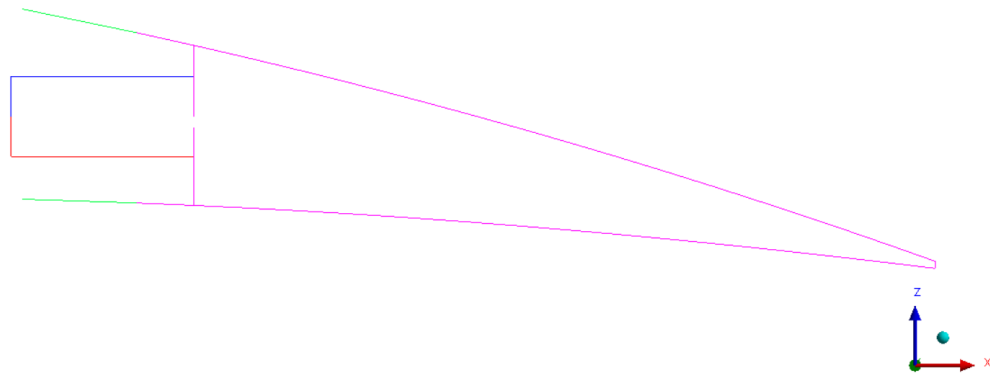


Figure 4.3: Side view of the open cell hybrid control surface

The upper and lower compliant parts (green) and rigid part (purple) are modeled as surface bodies, while the red and blue lines are modeled as beams. The long blue and red horizontal lines correspond to actuation rods of the servo actuator with circular cross-section, while blue and red vertical lines correspond to moment arms with rectangular cross section. The radius of the circular cross section is 1.25 mm, while the dimensions of the rectangular cross section are 7.4 mm x 1.9 mm. Initial thickness of the upper and lower compliant parts and the thickness of the rigid part are set as 1.5 mm.

During mesh generation, the element sizes are determined with a mesh convergence [43]. In Table 4.1, the element types used and the element sizes are given. The finite element model of the open cell control surface is shown in Figure 4.4 and Figure 4.5 as an isometric view and a side view, respectively.

Table 4.1: Element types and sizes of the control surface parts [44]

Control Surface Parts	Element Types	Element Size [mm]
Compliant Part	Quadrilateral SHELL 181	10
Skin of the Rigid Part	Quadrilateral SHELL 181	30
Transmission Part	Quadrilateral SHELL 181	10
Moment Arms and Actuation Rods of Servo Actuators	BEAM 188	20

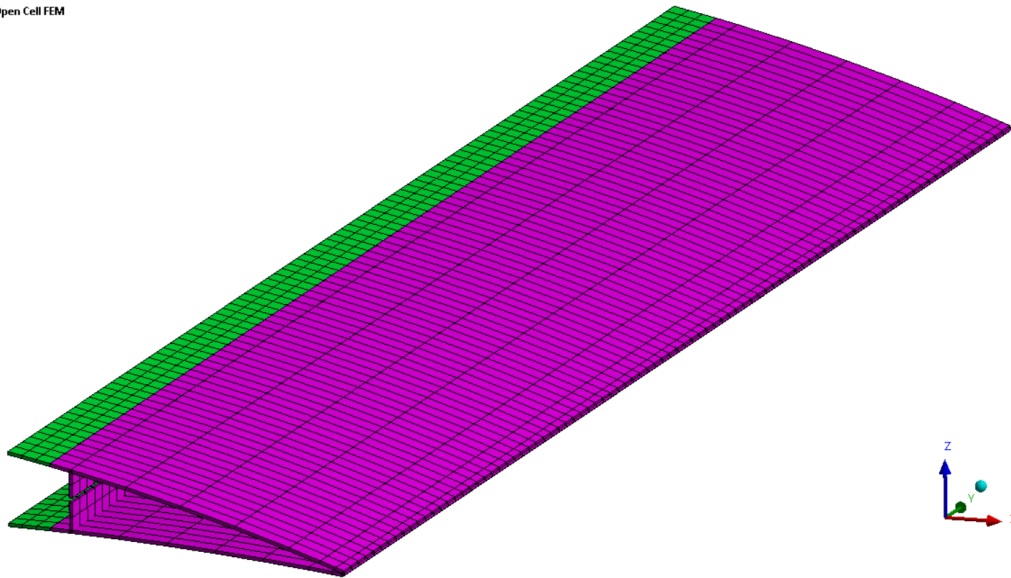


Figure 4.4: Finite element model of the open cell control surface design (isometric view)

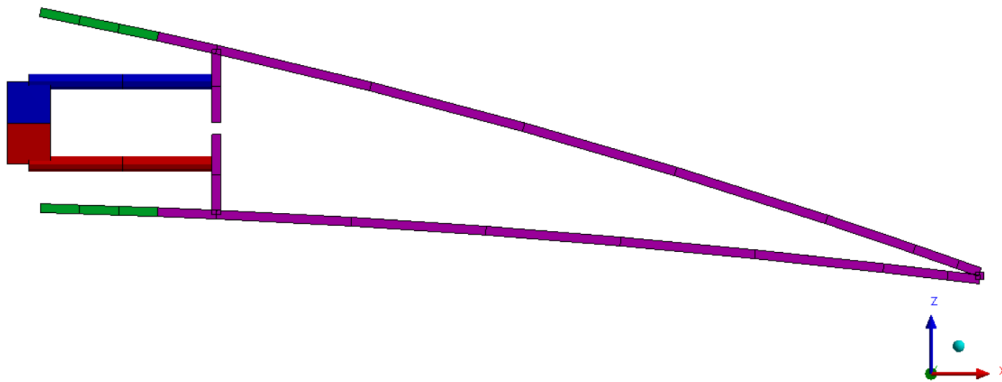


Figure 4.5: Finite element model of the open cell control surface design (side view)

The actuation rods are connected to the moment arms of servo actuators with pins. Due to pin connection the ends of the actuation rods and the moment arms are constrained in three displacement directions and rotations around two axes. Only the rotation around y axis is not constrained, see Figure 4.6. It is modeled with 'command' option by coupling the five degree of freedoms of the coinciding nodes of the actuation rods and moment arms in ANSYS Static Structural tool. The coinciding

nodes are depicted as green in Figure 4.6.

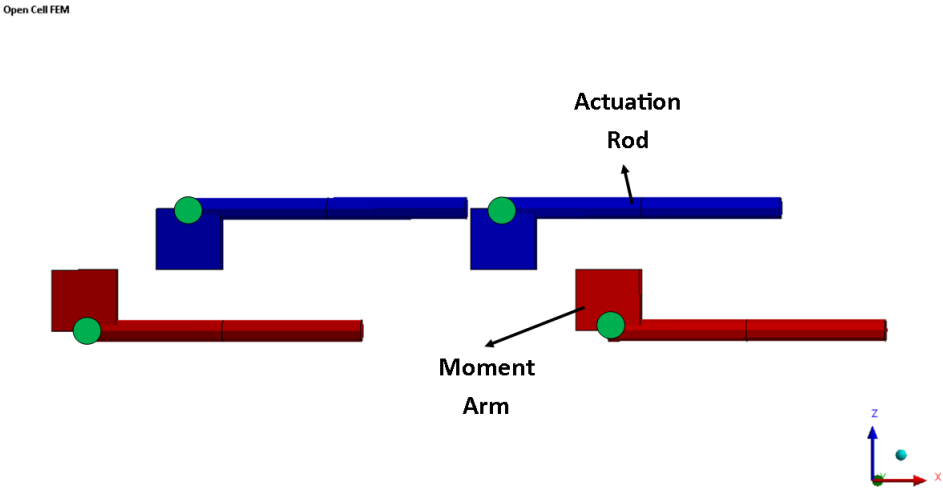


Figure 4.6: Constrained nodes of the moment arms and actuation rods of the servo actuators

As mentioned earlier, the control surface consists of different pieces named as rigid parts, compliant parts and transmission parts. In this study, it is assumed that these pieces are perfectly connected to each other. The actuation rods of the servo actuators are connected to transmission part with bonded contact option of ANSYS Static Structural. Figure 4.7 shows that the actuation rods of the upper servos and upper transmission part merge at points A and B, while the actuation rods of the lower servos and lower transmission part merge at points C and D.

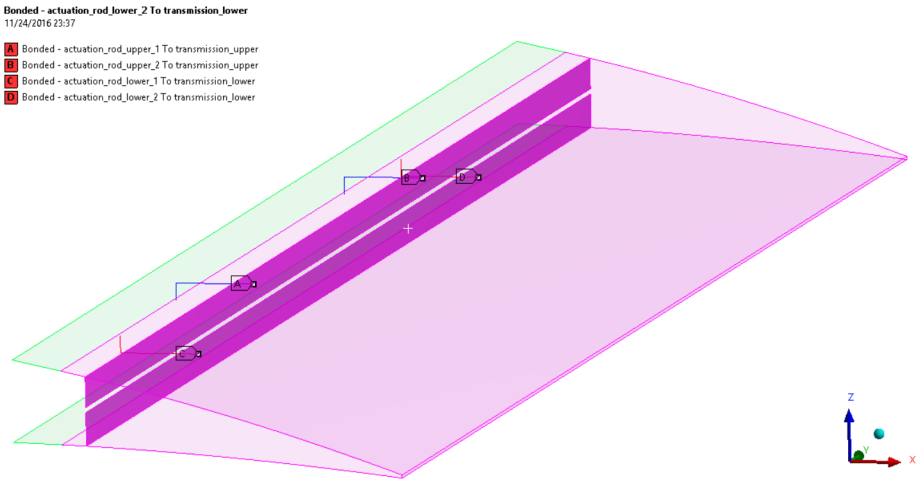


Figure 4.7: Bonded contact between actuation rods of the servo actuators and transmission parts of the control surface

In Finite Element Analysis, movement of the trailing edge control surface is provided by giving rotation angles to the nodes, denoted by points A and B, of the moment arms presented in Figure 3.10.

The hybrid trailing edge control surface is fixed at the edges shown with 'Fixed Support' tag in Figure 4.8. Also, in order to model the weight of the control surface 'standard earth gravity' presented in the same figure is applied to the finite element model.

In this study, due to large deflections and material nonlinearities of hyperelastic models, nonlinear finite element analyses need to be conducted. For this reason, 'large deflection' option is set as 'on' in the analyses. This option has to be on to conduct a nonlinear finite element analysis.

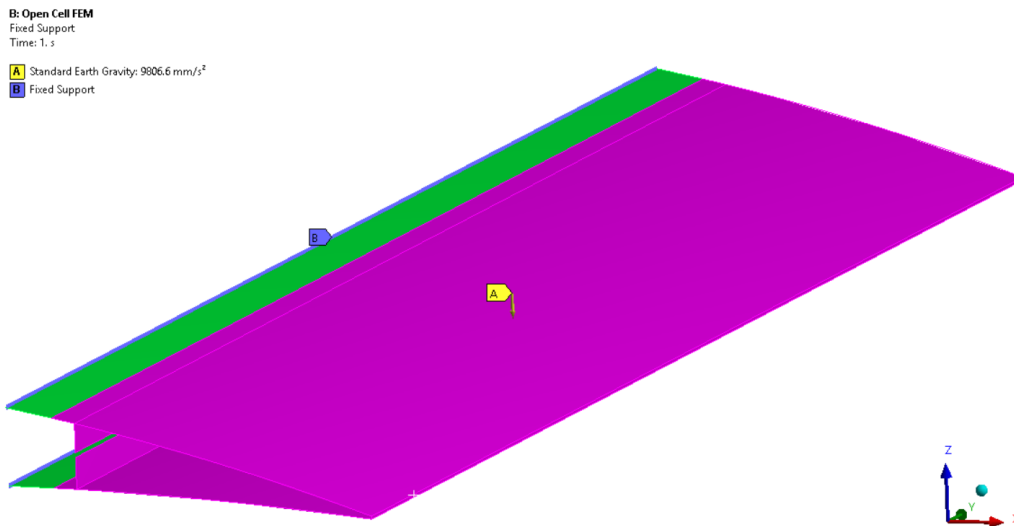


Figure 4.8: Applied boundary conditions of the finite element model

4.2.2 Finite Element Model of the Closed Cell Control Surface

Information about finite element model of the closed cell hybrid control surface is given in this part. The only difference between the closed cell and the open cell control surface is the design of the transmission part. Therefore, the finite element model of the closed cell control surface is generated by following the same steps followed in the open cell design. In Figure 4.9 and 4.10, the isometric view and the side view of the finite element model of the hybrid trailing edge control surface is

presented.

Closed Cell FEM

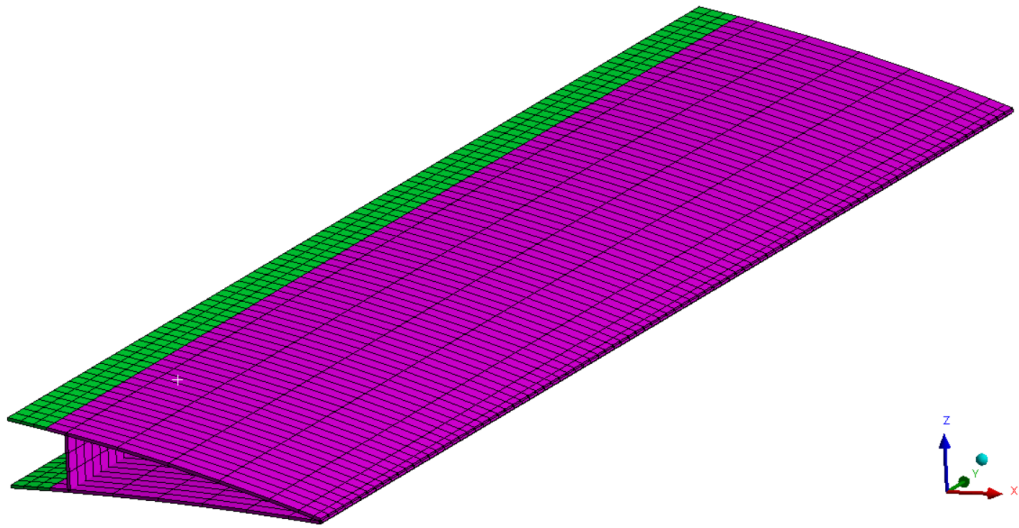


Figure 4.9: Finite element model of the closed cell control surface design (isometric view)

Closed Cell FEM

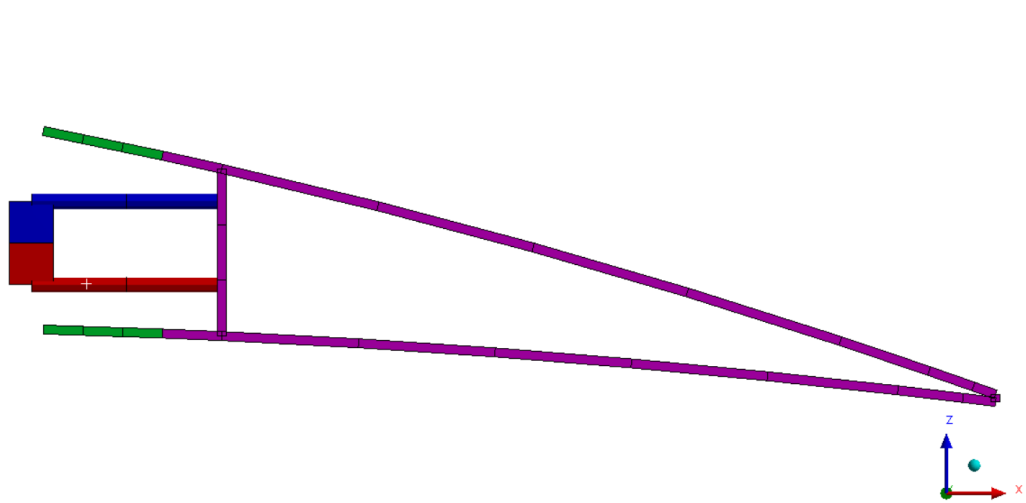


Figure 4.10: Finite element model of the closed cell control surface design (side view)

4.3 Optimization Analyses

In this section, the details of the optimization analysis is presented. The input parameters of the control surface in Table 3.6, the objectives and the constraints in Table

3.8 are entered to the Direct Optimization module of the ANSYS package program. There are several inputs for the optimization method as given below [40]:

- Method name: It specifies the method to be used for the optimization. In this study, it is selected as ‘Adaptive Multiple-Objective, due to the reasons which are explained in Section 3.6.
- Type of initial sampling: It defines how the sampling of inputs is made. It is selected as ‘Optimal Space Filling’ which can provide optimal spaces between inputs during sampling for the optimization. In Figure 4.11 shows how the optimal space filling method distributes the inputs without leaving the input field.

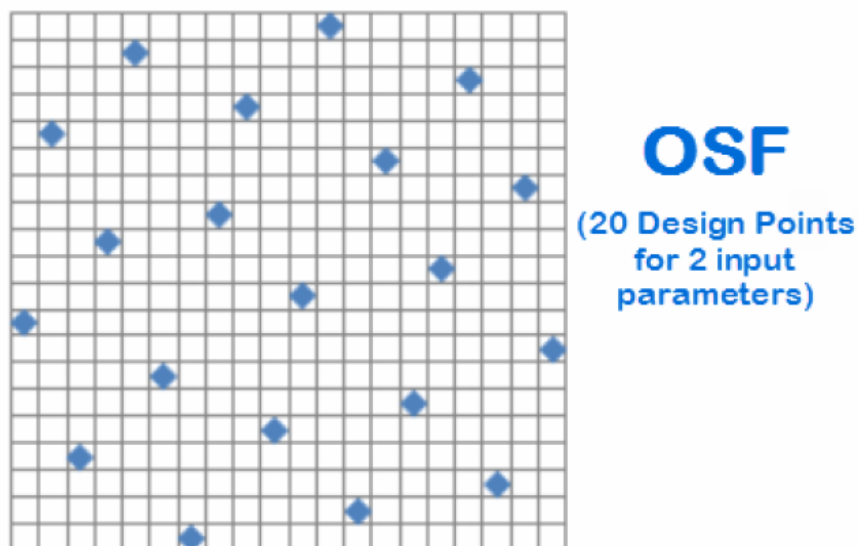


Figure 4.11: Inputs distribution in Optimal Space Filling method [40]

- Number of initial samples: It specifies the initial sample size in the optimization process. It must be higher than ten times of the number of input parameters. The number of initial samples is set as one hundred after conducting some trial optimization runs, see Appendix B.
- Number of samples per iteration: It defines the number of samples at each iteration in the optimization study. It has to be less than or equal to the number

of initial samples. In this study this value is set as fifty which is less than the number of initial samples after conducting some trial runs, see Appendix B.

- Maximum allowable Pareto percentage: It is a convergence criterion which is explained in the in Section 3.6. To find the best solution the number must be between 55 and 75. In this study, it is taken as 70 which is the default value.
- Convergence stability percentage: It is a convergence criterion calculated from the mean and the standard deviation of the solutions. It allows to decrease the number of iterations when the stability is achieved as stopping the optimization. In this study, convergence stability percentage is set as 2 percent which is the default value.
- Maximum number of iterations: It is a stopping criterion for optimization study without checking the convergence. It is set as 20 in this optimization study.
- Maximum number of candidates: It is the desired number of best solutions and corresponding input values. In this study, it is set as 3 which is the default value.

4.4 Results of Optimization Analyses

In this part, the candidate optimum design points which are the results of the direct optimization study are explained for each material and the two different control surface designs.

4.4.1 Results of Open Cell Control Surface Design

In the optimization of compliant parts of the open cell control surface design convergence is obtained only for the neoprene rubber and sample elastomer-1. Other materials, sample elastomer-2 and silicone, could not achieve the desired tip deflection with the available torque of the servo actuators. Therefore, candidate points for these materials could not be obtained.

Input values of the candidate points for neoprene rubber compliant parts of the open

cell control surface are presented in Table 4.2, while corresponding output values to these inputs are presented in Table 4.3. Similarly, input values for sample elastomer-1 and corresponding output values to these inputs are shown in Table 4.4 and Table 4.5, respectively.

Table 4.2: The input values of candidate points for neoprene rubber compliant part of the open cell control surface

Name	R_{y_l} [degree]	R_{y_u} [degree]	t_l [mm]	t_u [mm]	L_l [mm]	L_u [mm]
CP1	-35.60	18.91	1.00	1.92	21.36	3.10
CP2	-36.04	19.62	1.04	1.87	20.80	3.48
CP3	-33.93	17.56	1.21	1.89	24.20	3.18

Table 4.3: The output values of candidate points for neoprene rubber compliant part of the open cell control surface

Name	d_z [mm]	Q_l [Nmm]	Q_u [Nmm]	σ_{cmin} [MPa]	σ_{cmax} [MPa]	ϵ_{umin} [-]	ϵ_{lmin} [-]	ϵ_{umax} [-]	ϵ_{lmax} [-]
CP1	20.47	491.31	165.54	-52.05	36.07	0.19	0.17	0.26	0.22
CP2	19.93	501.78	172.47	-54.88	38.48	0.20	0.17	0.26	0.23
CP3	19.97	526.65	226.58	-43.36	26.34	0.16	0.14	0.23	0.20

Table 4.4: The input values of candidate points for sample elastomer-1 compliant part of the open cell control surface

Name	R_{y_l} [degree]	R_{y_u} [degree]	t_l [mm]	t_u [mm]	L_l [mm]	L_u [mm]
CP4	-34.91	18.66	1.16	1.58	23.79	4.10
CP5	-33.70	17.32	1.07	1.58	22.51	3.76
CP6	-33.69	17.33	1.06	1.56	22.39	3.80

Table 4.5: The output values of candidate points for sample elastomer-1 compliant part of the open cell control surface

Name	d_z [mm]	Q_l [Nmm]	Q_u [Nmm]	σ_{cmin} [MPa]	σ_{cmax} [MPa]	ϵ_{umin} [-]	ϵ_{lmin} [-]	ϵ_{umax} [-]	ϵ_{lmax} [-]
CP4	20.42	743.39	169.69	-23.38	19.28	0.12	0.15	0.19	0.20
CP5	20.53	760.28	83.19	-23.81	19.82	0.10	0.15	0.17	0.21
CP6	20.47	760.36	74.79	-23.81	19.82	0.10	0.15	0.17	0.21

4.4.2 Results of Closed Cell Control Surface Design

In the optimization of compliant parts of the closed cell control surface design convergence is obtained only for the neoprene rubber and sample elastomer-1 as in the case of open cell control surface. Other materials, sample elastomer-2 and silicone, could not achieve the desired tip deflection with the available torque of the servo actuators. Therefore, no candidate point could be found.

Input values of the candidate points for neoprene rubber compliant parts of the closed cell control surface design are presented in Table 4.6, while corresponding output values to these inputs are presented in Table 4.7. Similarly, input values for sample elastomer-1 and corresponding output values to these inputs are shown in Table 4.8 and Table 4.9, respectively.

Table 4.6: The input values of candidate points for neoprene rubber compliant part of the closed cell control surface

Name	R_{y_l} [degree]	R_{y_u} [degree]	t_l [mm]	t_u [mm]	L_l [mm]	L_u [mm]
CP7	-34.16	19.67	1.23	1.94	24.12	3.04
CP8	-34.18	19.67	1.23	1.93	19.98	3.03
CP9	-32.78	19.61	1.23	1.93	24.02	3.04

Table 4.7: The output values of candidate points for neoprene rubber compliant part of the closed cell control surface

Name	d_z [mm]	Q_l [Nmm]	Q_u [Nmm]	σ_{cmin} [MPa]	σ_{cmax} [MPa]	ϵ_{umin} [-]	ϵ_{lmin} [-]	ϵ_{umax} [-]	ϵ_{lmax} [-]
CP7	20.20	555.63	104.96	-241.07	224.97	0.16	0.15	0.29	0.20
CP8	20.20	587.31	117.99	-242.63	225.47	0.16	0.19	0.29	0.23
CP9	18.37	518.64	52.26	-224.90	209.93	0.19	0.14	0.31	0.19

Table 4.8: The input values of candidate points for sample elastomer-1 compliant part of the closed cell control surface

Name	R_{y_l} [degree]	R_{y_u} [degree]	t_l [mm]	t_u [mm]	L_l [mm]	L_u [mm]
CP10	-32.93	18.81	1.07	1.64	21.78	5.50
CP11	-31.26	16.65	1.13	1.60	23.78	3.92
CP12	-32.86	18.27	1.34	1.89	20.42	7.66

Table 4.9: The output values of candidate points for sample elastomer-1 compliant part of the closed cell control surface

Name	d_z [mm]	Q_l [Nmm]	Q_u [Nmm]	σ_{cmin} [MPa]	σ_{cmax} [MPa]	ϵ_{umin} [-]	ϵ_{lmin} [-]	ϵ_{umax} [-]	ϵ_{lmax} [-]
CP10	19.77	856.09	64.78	-205.79	179.52	0.07	0.16	0.17	0.21
CP11	20.34	876.36	26.57	-198.24	171.57	0.05	0.14	0.17	0.19
CP12	20.10	1165.97	208.58	-218.30	181.93	0.04	0.17	0.12	0.23

4.5 Selection of Best Design Configuration

As it can be seen from Tables 4.3, 4.5, 4.7 and 4.9, all the candidate points provide nearly 20.2 mm trailing edge tip deflection of the control surface. This value is requested for deflection of the control surface from NACA 6510 to NACA 2510 airfoil profile. Moreover, torque values of the servo actuators are lower than the maximum

torque obtained from selected servo actuator. Besides, the minimum and the maximum combined stress values of the actuation rods and the moment arms of the servo actuators are lower than the yield stress of the aluminum presented in Table 3.3. In addition to these results, minimum normal strains of the compliant parts of the control surface are bigger than zero, indicating that compliant parts are not compressed. The maximum normal strain results of the compliant parts are under one hundred percent. This means that strains do not exceed the maximum normal strain limit in the optimization.

All candidate optimized design points are given in Tables 4.3, 4.5, 4.7 and 4.9. However, one of the candidate points must be selected as the best design point to design the control surface. For this reason, the best design point is chosen by looking at the required torque values, since other constraints and objectives are already met. Note that the combined beam stresses are lower in the open cell design. Therefore, the CP1 is selected as best design point. Because, smallest torque values of the servo actuators are provided in CP1 to deflect the hybrid trailing edge control surface from base profile to NACA 2510 airfoil shape. In addition to this, CP1 is chosen by looking at the torque of the servo actuators to actuate the lower part. Because this torque is greater than the torque value needed for the servo actuators to actuate the upper part of the control surface in all candidate points. This best point belongs to the open cell design of the control surface with the compliant parts which is made of neoprene rubber material. Moreover, factor of safety values of the servo torque requirements and combined stresses of actuation rods and moment arms for the best design configuration are much higher than 1.5 which is specified by [45], according to Table 4.10. Also, Pareto fronts of three objective functions are presented in Figures C.1 - C.3 with two dimensional plots together with the optimization raw data for the optimization analysis which includes this best design point. Then, the inputs of the best design points are rounded and simplified by considering manufacturability of the control surface.

Simplified inputs of the best design are presented in Table 4.11. The corresponding output values to these inputs obtained by a finite element analysis are shown in Table 4.12. In Figure 4.12, the deflection of the control surface in z direction during morphing from base profile to NACA 2510 airfoil profile is depicted. Moreover, minimum and maximum combined stress of the moment arms and actuation rods are presented

for the same analysis in Figure 4.13 and Figure 4.14.

Table 4.10: Factor of safety values of servo torque reactions and combined stress values of beams for best control surface design

	Q_l	Q_u	σ_{cmin}	σ_{cmax}
CP1	2.44	7.25	5.96	8.59

Table 4.11: The input values of the selected simplified candidate design point for the analysis of morphing the control surface to NACA 2510 from NACA 6510

Name	R_{y_l} [degree]	R_{y_u} [degree]	t_l [mm]	t_u [mm]	L_l [mm]	L_u [mm]
Simplified CP	-35.50	19.00	1.00	1.90	21.00	3.00

Table 4.12: The corresponding output values to the selected simplified candidate design point for the analysis of morphing the control surface to NACA 2510 from NACA 6510

Name	d_z [mm]	Q_l [Nmm]	Q_u [Nmm]	σ_{cmin} [MPa]	σ_{cmax} [MPa]	ϵ_{umin} [-]	ϵ_{lmin} [-]	ϵ_{umax} [-]	ϵ_{lmax} [-]
Simplified CP	20.26	485.15	150.17	-52.00	36.24	0.20	0.17	0.27	0.22

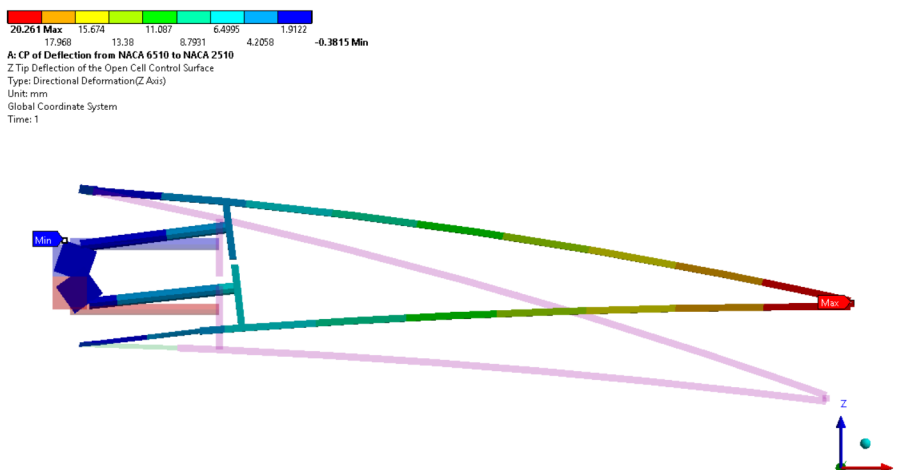


Figure 4.12: Displacement of the control surface in z direction in case of morphing from NACA 6510 profile to NACA 2510 profile

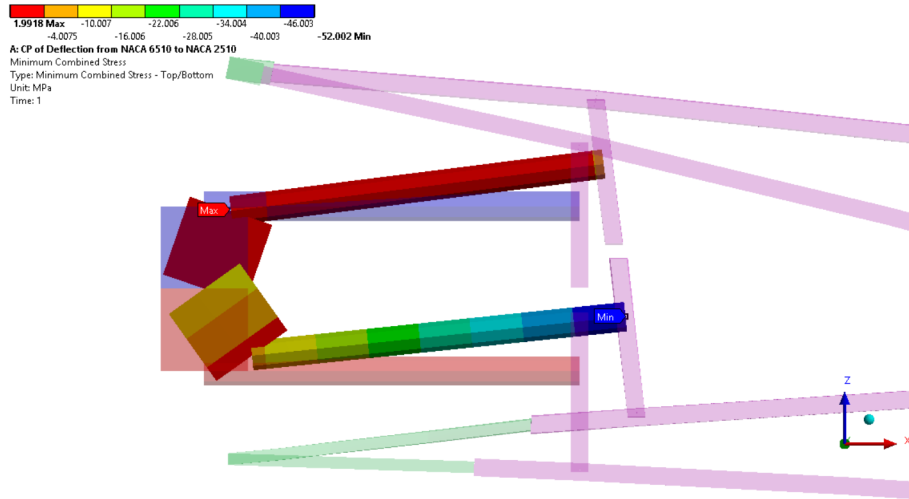


Figure 4.13: Minimum combined beam stress distribution in case of morphing from NACA 6510 profile to NACA 2510 profile

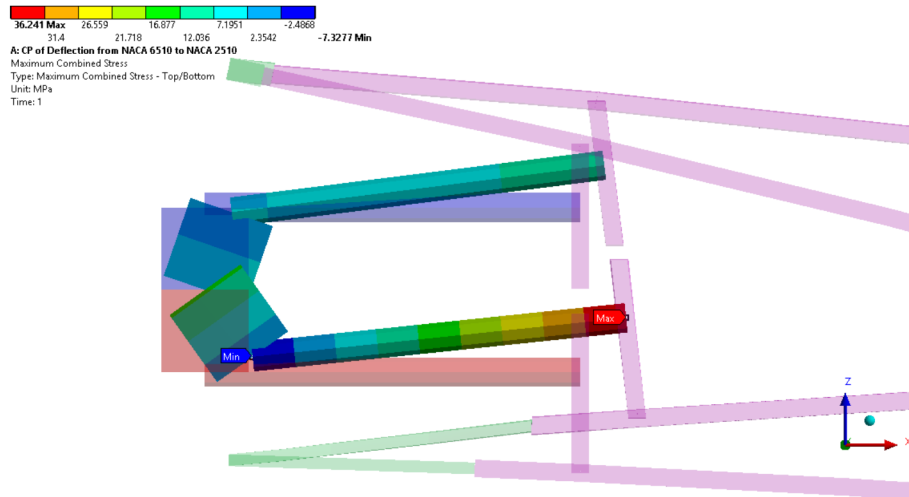


Figure 4.14: Maximum combined beam stress distribution in case of morphing from NACA 6510 profile to NACA 2510 profile

4.6 Analysis of Morphing from NACA 6510 to NACA 3510

In this part, the selected best design is analyzed for the deflection of the control surface from base profile to NACA 3510 airfoil profile. Except the rotation angles applied to moment arms all other parameters are the same as given in 4.11. The rotation angles are obtained by an optimization analysis of the open cell control surface design using the lengths and thicknesses in Table 3.6 for the deflection of control

surface from NACA 6510 to NACA 3510 airfoil profile. Input values of the analysis are shown in Table 4.13, while the corresponding output values to these inputs are presented in Table 4.14.

Table 4.13: The input values of the selected simplified candidate design point for the analysis of morphing the control surface to NACA 3510 from NACA 6510

Name	R_{y_l} [degree]	R_{y_u} [degree]	t_l [mm]	t_u [mm]	L_l [mm]	L_u [mm]
Simplified CP	-30.5	18.00	1.00	1.90	21.00	3.00

Table 4.14: The corresponding output values to the selected simplified candidate design point for the analysis of morphing the control surface to NACA 3510 from NACA 6510

Name	d_z [mm]	Q_l [Nmm]	Q_u [Nmm]	σ_{cmin} [MPa]	σ_{cmax} [MPa]	ϵ_{umin} [-]	ϵ_{lmin} [-]	ϵ_{umax} [-]	ϵ_{lmax} [-]
Simplified CP	15.34	415.53	39.13	-40.45	27.30	0.27	0.15	0.32	0.19

In Figure 4.15, the deflection of the control surface in z direction during morphing from base to NACA 3510 airfoil profile is presented. Moreover, minimum and maximum combined stress of the moment arms and actuation rods are presented in Figure 4.16 and Figure 4.17.

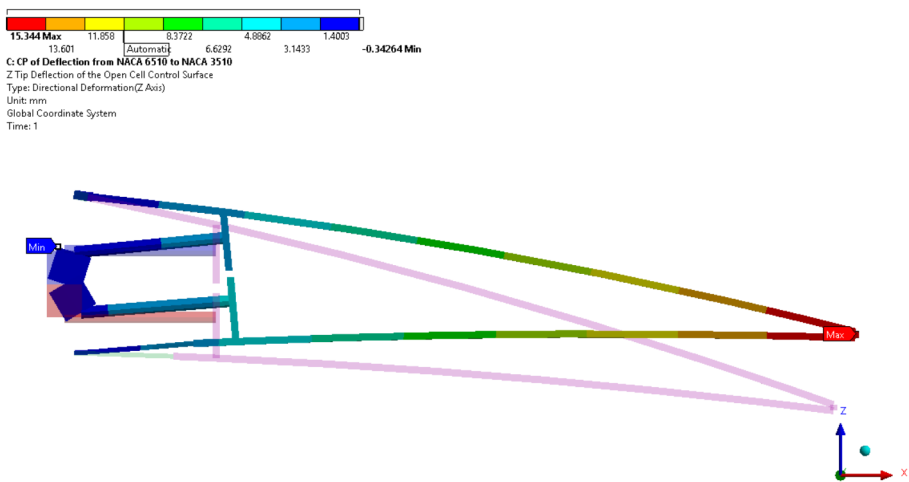


Figure 4.15: Displacement of the control surface in z direction in case of morphing from NACA 6510 profile to NACA 3510 profile

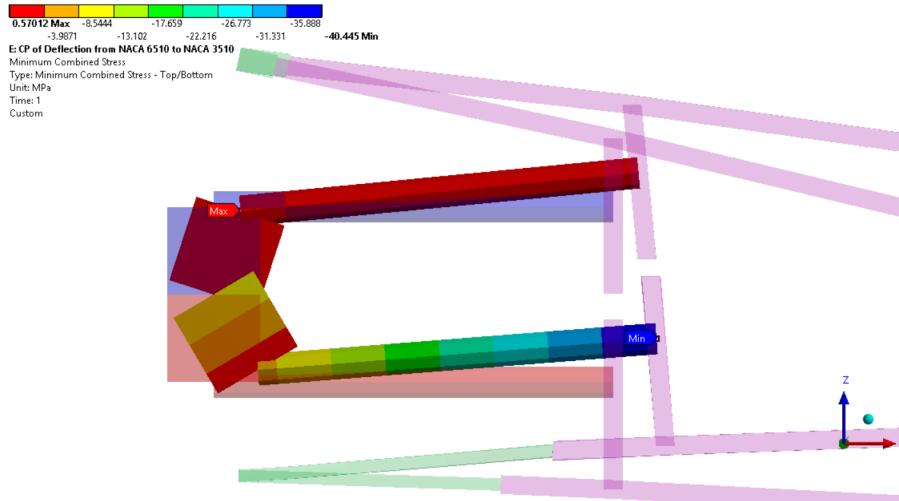


Figure 4.16: Minimum combined beam stress distribution in case of morphing from NACA 6510 profile to NACA 3510 profile

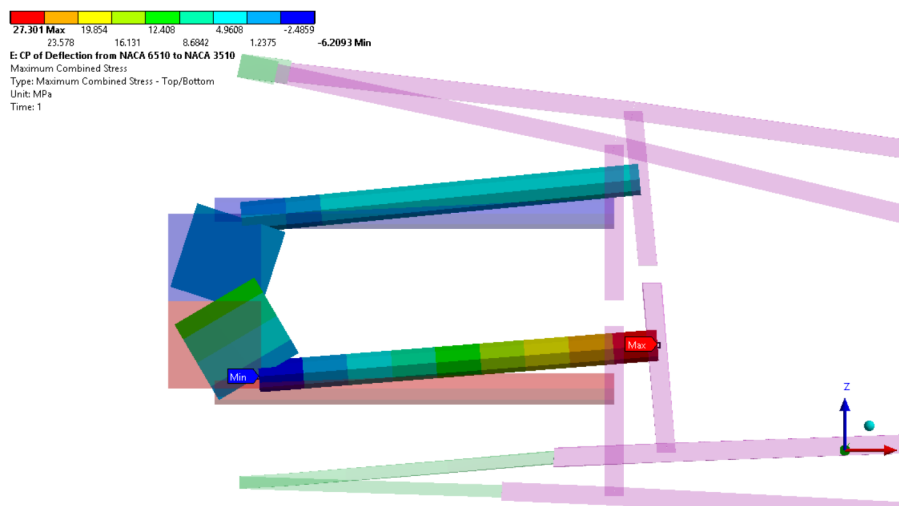


Figure 4.17: Maximum combined beam stress distribution in case of morphing from NACA 6510 profile to NACA 3510 profile

As it can be seen from Table 4.14, the best design provides nearly 15.2 mm trailing edge tip deflection on the control surface. This value is requested for deflection of the control surface from NACA 6510 airfoil to NACA 3510 airfoil profile. Moreover, torque values of the servo actuators are lower than the maximum torque limits of the selected servo actuator. Besides, minimum and maximum combined stress values of the actuation rods and the moment arms of the servo actuators are lower than the yield stress of the aluminum presented in Table 3.3. In addition to these results, minimum

normal strains of the compliant parts of the control surface are greater than zero, indicating that compliant parts are in tension.

4.7 Conclusion and Discussion

In this chapter, optimization analyses of the compliant parts on the hybrid trailing edge control surface are conducted for the open cell and the closed cell designs in-vacuo condition.

Firstly, the finite element models of open cell and closed cell control surfaces are explained. Then, inputs of the optimization performed with ANSYS Direct Optimization tool are described. After that, results of the optimization analysis for both open cell and closed cell designs are presented. As a result of this optimization analysis, desired tip deflection of the control surface is not obtained for the sample elastomer-2 and silicone with the available torque limits of the selected servo actuator, while neoprene rubber and sample elastomer-1 could provide the requested tip deflection. This is due to the relative stiffnesses of considered four materials, see Figure 3.8. Therefore, for the desired amount of deflection at the tip of the control surface, more servo torque is needed and the selected servo actuator could not provide this torque value for the compliant parts made of sample elastomer-2 and silicone.

In the next part, the optimal design point for all the constraints and objectives is selected among the candidate points resulting from the optimization analysis, considering the required smallest servo torque for the actuation. The optimum design belongs to the open cell control surface design. As can be seen from the results of candidate points, the stresses on the actuation mechanisms are much lower than the closed cell design, since open transmission parts have low stiffness than the closed one. In order to generate more elongation with fewer forces, long and thin compliant parts are needed. In this study, the aim is to deflect the control surface in upward direction. As expected, the lower compliant part of the best design is longer and thinner than the upper compliant part according to the results of structural analysis of best design point. Then, this optimal design point is analyzed for the deflection of the control surface from base profile to NACA 3510 profile by changing only the rotation

angles of moment arms.

Finally, it is shown that morphing the hybrid control surface from NACA 6510 profile to both NACA 3510 and NACA 2510 profiles is possible with the proposed design considering all the constraints and objectives in the optimization analysis. However, this best control surface design should be checked under the aerodynamic loads that the control surface is exposed to in the desired flight tasks. In the next section, structural analyzes under aerodynamic loads are explained for each flight condition.

CHAPTER 5

FINITE ELEMENT ANALYSIS OF THE OPTIMIZED HYBRID CONTROL SURFACE DESIGN UNDER AERODYNAMIC LOADS

5.1 Introduction

In this section, the optimum design of the hybrid control surface found in the previous section is analyzed structurally under the aerodynamic loads and results are interpreted.

In the first part, the calculation method of the aerodynamic loads that are applied to the control surface are explained. Moreover, the inputs of the Computational Fluid Dynamics (CFD) analyses are given for different flight conditions. In the second part, finite element analyses of the hybrid control surface under the obtained aerodynamic loads are presented. In the third part, results of the structural analysis are interpreted.

5.2 Aerodynamic Loads

In this thesis, loiter or landing, take-off and cruise or high speed dash flight phases are considered for the optimization of the compliant parts of the control surface. To this end, aerodynamic loads are obtained using a CFD program namely, Stanford University Unstructured (SU2) V3.2.03 package program for these phases. Computation of aerodynamic loads have been done in [1]. The aerodynamic mesh used in CFD analyses of the wing is generated by using Pointwise V17.2R2 package program. The generated aerodynamic mesh and the hemisphere outer domain mesh of the wing are shown in Figure 5.1. All the CFD analyses are conducted for the whole wing, not

for the control surface. Then, the aerodynamic loads acting on the control surface are considered only and structural analyzes are carried out. In addition, only 1g flight cases are considered in this project.

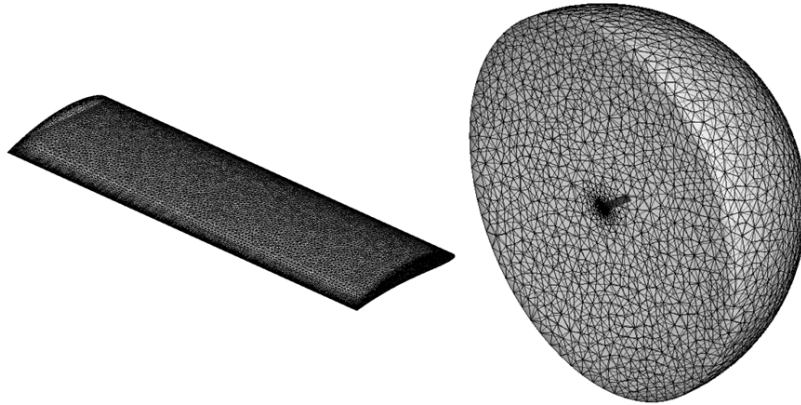


Figure 5.1: Aerodynamic Mesh of the Morphing Wing and Hemisphere Outer Domain Mesh [1]

In the CFD analyses, the parameters defined by CHANGE project in Table 5.1 are entered to the SU2 open-source program [2]. Flow in the CFD analyses is assumed as incompressible due to low Mach number presented in Table 5.1. Also, the flow is modeled as viscous using Reynolds Averaged Navier-Stokes (RANS) method. This method is combined with the Spallart Almaras turbulence model in the CFD analyses. Then, CFD analyses are conducted for the wings which have the NACA 6510 (base profile), NACA 3510 and NACA 2510 airfoil profiles in order to compute the aerodynamic loads. As a result of the analyses, the pressure distributions over the wing for these airfoil profiles are obtained.

Table 5.1: Input parameters for the CFD analyses

	Loiter or Landing	Take-off Phase	Cruise or High Speed Dash Phase
Flight speed [m/s]	13.24	21.15	30.56
Angle of attack [degree]	6.37	1.71	1.06
Density [kg/m ³]	1.19	1.23	1.19
Altitude [ft]	1000.00	0.00	1000.00
Mach number	0.04	0.06	0.09
Reynolds number	524536.00	857990.00	1210135.00

5.3 Structural Analysis of the Optimized Control Surface Design under Aerodynamic Loads

In this section, the purpose of the structural analyses is to check whether the optimum control surface withstands to the aerodynamic loads that are exposed during different flight tasks explained in Section 3.2. In order to perform the flight tasks, control surface must maintain own base profile, NACA 6510, and deflect from NACA 6510 to NACA 3510 and NACA 2510 airfoil profiles. For the above mentioned profiles, aerodynamic loads are obtained. Finite element model of the hybrid control surface is the same as in Section 4.2. The only difference between finite element models is aerodynamic loads which are imported to the control surface geometry. These aerodynamic loads are applied to the hybrid trailing edge control surface as pressure. ANSYS Static Structural module is able to map the aerodynamic mesh to the structural mesh with 'imported load' option.

The control surface exposed to the imported pressure while maintaining the base profile is shown in Figure 5.2 and Figure 5.3 for the upper and lower parts of the control surface, respectively. Moreover, imported pressure applied to the deflected control surface having NACA 3510 profile is shown in Figure 5.4 and Figure 5.5 for the upper part and lower part of the control surface, respectively. Similarly, Figure 5.6 and Figure 5.7 present the imported pressure applied to the control surface for the deflected NACA 2510 profile.

In this part, structural analyses of the control surface under the aerodynamic loads are conducted for non-deflected and deflected control surface profiles. For the non-deflected control surface case, no rotation is applied to the servo actuators. The aerodynamic loads obtained for the loiter or landing phase of the flight (NACA 6510 airfoil profile) are imported to the control surface. Then, the control surface is structurally analyzed under these aerodynamic loads. Due to the applied aerodynamic loads, the control surface deflects in small amount. In order to bring back the control surface to the NACA 6510 airfoil profile, some trial error analyses have been conducted to with changing the rotations of the servo actuator. As a result of these analyses, the rotation angles in Table 5.2 are found in order to maintain NACA 6510 airfoil profile of the control surface. For the deflected control surface cases, two anal-

yses are conducted. These are the analyses of morphing from NACA 6510 to NACA 3510 and NACA 2510 airfoil profiles, respectively. In order to conduct the two analyses, different rotations and different aerodynamic loadings are used. The rotation angles in Table 4.13 and Table 4.11 are applied to the servo actuators for the deflection of the control surface from NACA 6510 to NACA 3510 and NACA 2510 airfoil profiles, respectively. The aerodynamic loads obtained for the take-off (NACA 3510) and the cruise or high speed dash (NACA 2510) phases of the flight are imported to the control surface. Then, the control surface is structurally analyzed under these two aerodynamic loadings. In order to achieve the same deflection required for NACA 3510 and NACA 2510 profiles in control surface, the rotation angles of the servo actuators are regulated by small angle changes. The rotation angles are presented in Table 5.2 with the dimensions of the optimum control surface design found in the previous chapter. In the subsections, the results of the structural analyses are given.

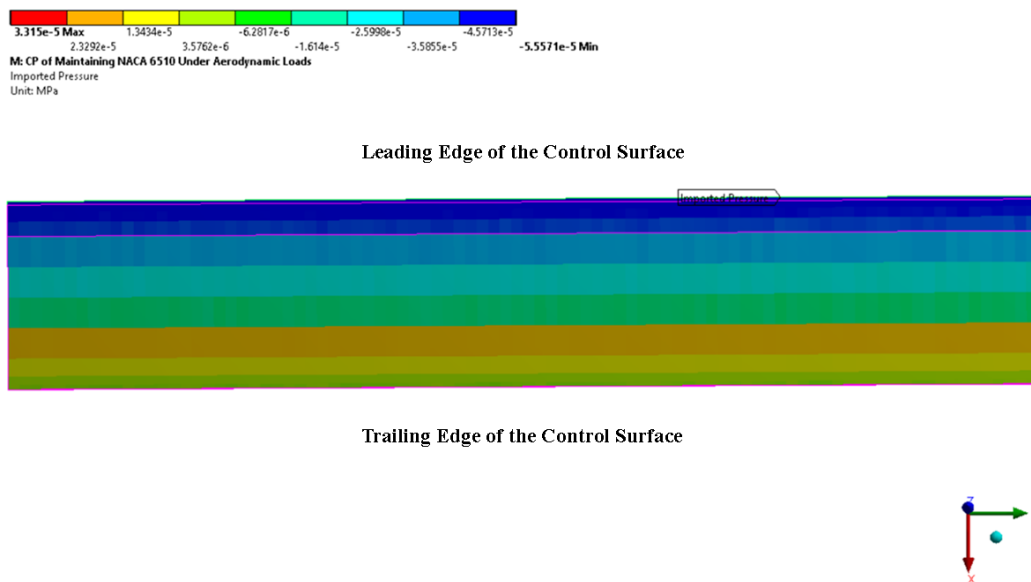
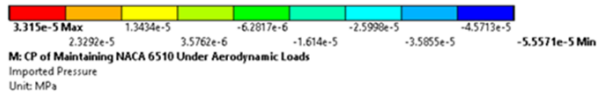
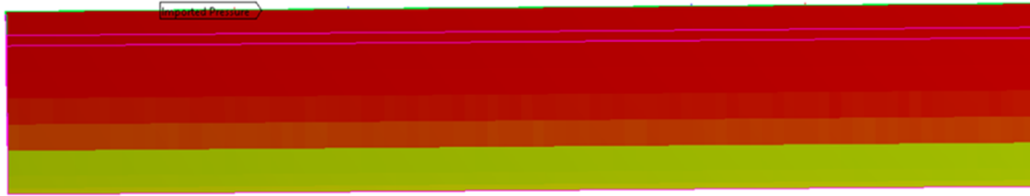


Figure 5.2: Imported pressure applied to the upper skin of the control surface in case of maintaining NACA 6510 profile



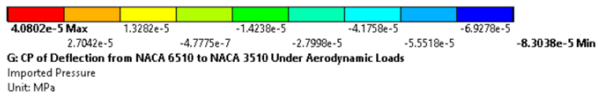
Leading Edge of the Control Surface



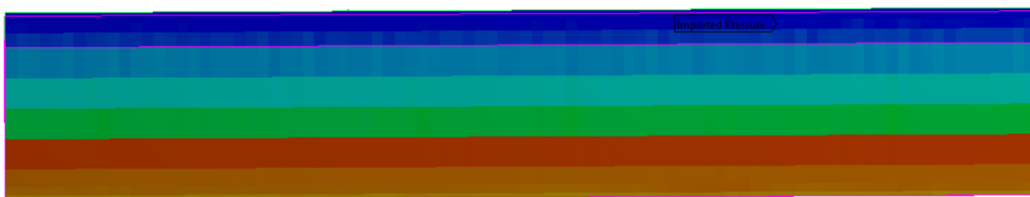
Trailing Edge of the Control Surface



Figure 5.3: Imported pressure applied to the lower skin of the control surface in case of maintaining NACA 6510 profile



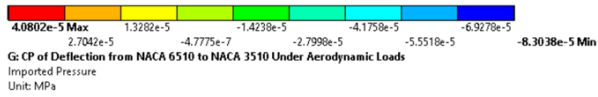
Leading Edge of the Control Surface



Trailing Edge of the Control Surface



Figure 5.4: Imported pressure applied to the upper skin of the control surface in case of deflection to NACA 3510 profile



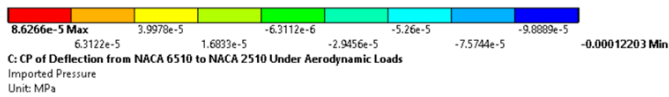
Leading Edge of the Control Surface



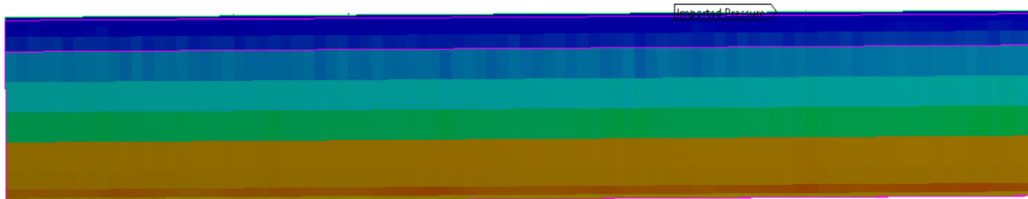
Trailing Edge of the Control Surface



Figure 5.5: Imported pressure applied to the lower skin of the control surface in case of deflection to NACA 3510 profile



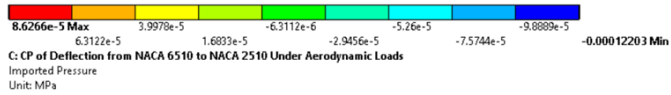
Leading Edge of the Control Surface



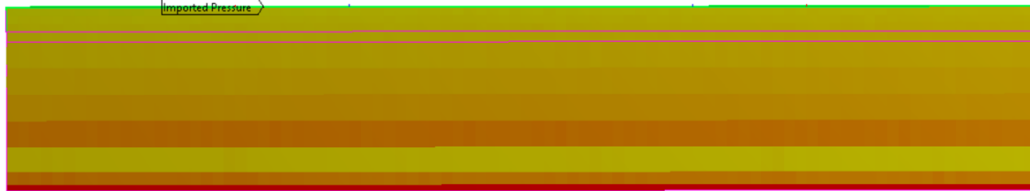
Trailing Edge of the Control Surface



Figure 5.6: Imported pressure applied to the upper skin of the control surface in case of deflection to NACA 2510 profile



Leading Edge of the Control Surface



Trailing Edge of the Control Surface



Figure 5.7: Imported pressure applied to the lower skin of the control surface in case of deflection to NACA 2510 profile

Table 5.2: The input values of the finite element analysis under aerodynamic loads

Analyzed Cases	R_{y_l} [degree]	R_{y_u} [degree]	t_l [mm]	t_u [mm]	L_l [mm]	L_u [mm]
Maintaining NACA 6510	-4.50	3.50	1.00	1.90	21.00	3.00
Deflection to NACA 3510	-26.50	15.00	1.00	1.90	21.00	3.00
Deflection to NACA 2510	-33.00	17.50	1.00	1.90	21.00	3.00

5.3.1 Results of the Analysis of Maintaining NACA 6510 Airfoil Case

In this part, the results of the structural analysis of the optimum control surface design under aerodynamic loads are presented and interpreted. The analysis is conducted to maintain the base airfoil profile, NACA 6510, of the wing under aerodynamic loads. Results of this analysis are shown in Table 5.3.

Table 5.3: Results of the finite element analysis of maintaining NACA 6510 airfoil profile under aerodynamic loads

Airfoil Profile	d_z [mm]	Q_l [Nmm]	Q_u [Nmm]	σ_{cmin} [MPa]	σ_{cmax} [MPa]	ϵ_{umin} [-]	ϵ_{lmin} [-]	ϵ_{umax} [-]	ϵ_{lmax} [-]
NACA 6510	0.58	253.75	101.66	-25.35	28.29	0.12	0.02	0.14	0.04

In Figure 5.8, the deflection of the control surface in z direction while maintaining NACA 6510 airfoil profile is depicted. Moreover, minimum and maximum combined stress of the moment arms and actuation rods are presented for the same analysis in Figure 5.9 and Figure 5.10, respectively.

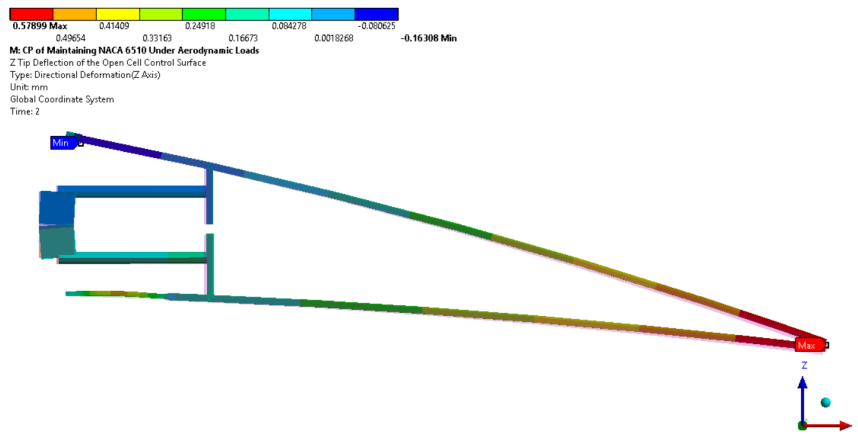


Figure 5.8: Displacement of the control surface in z direction while maintaining NACA 6510 profile under aerodynamic loads

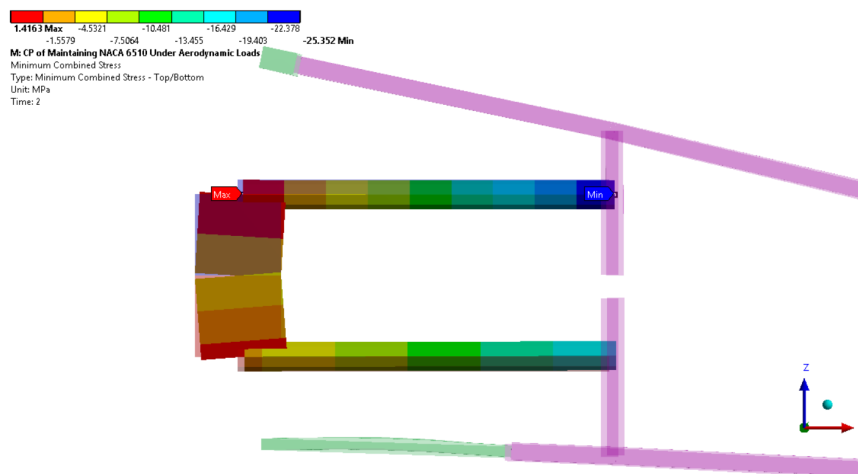


Figure 5.9: Minimum combined beam stress distribution while maintaining NACA 6510 profile under aerodynamic loads

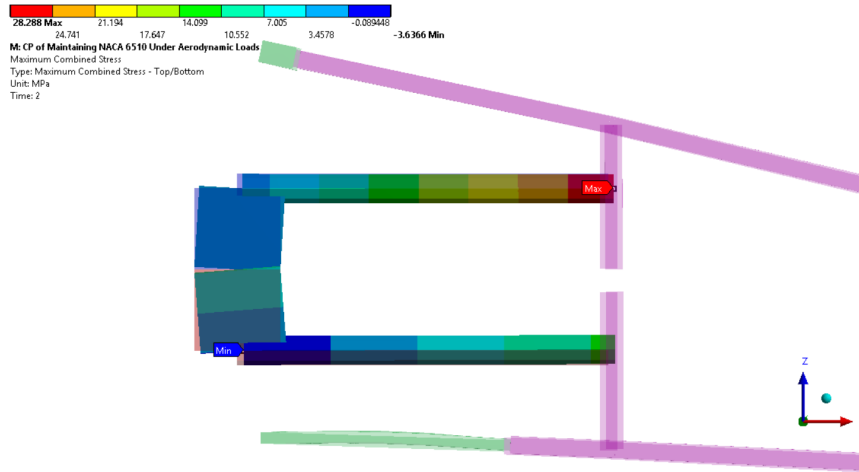


Figure 5.10: Maximum combined beam stress distribution while maintaining NACA 6510 profile under aerodynamic loads

As it can be seen from Table 5.3, the best control surface design is able to maintain the base profile under aerodynamic loading. Moreover, torque values of the servo actuators are lower than the maximum torque limits of the selected servo actuator. Besides, minimum and maximum combined stress values of the actuation rods and the moment arms of the servo actuators are lower than the yield stress of the aluminum presented in Table 3.3. In addition to these results, minimum normal strains of the compliant parts of the control surface are greater than zero, indicating that compliant parts are in tension.

5.3.2 Results of the Analysis of Deflection to NACA 3510 Airfoil Case

In this part, the analysis is conducted for the deflection of the control surface from NACA 6510 to NACA 3510 airfoil profile. Results of this analysis are shown in Table 5.4.

Table 5.4: Results of the finite element analysis of the deflection to NACA 3510 airfoil under aerodynamic loads

Airfoil Profile	d_z [mm]	Q_t [Nmm]	Q_u [Nmm]	σ_{cmin} [MPa]	σ_{cmax} [MPa]	ϵ_{umin} [-]	ϵ_{lmin} [-]	ϵ_{umax} [-]	ϵ_{lmax} [-]
NACA 3510	15.07	263.16	38.72	-18.24	17.16	0.15	0.13	0.24	0.18

In Figure 5.11, the deflection of the control surface in z direction while morphing from base to NACA 3510 airfoil profile is presented for the best design under the aerodynamic loads. Moreover, minimum and maximum combined stress of the moment arms and actuation rods are presented for the same analysis in Figure 5.12 and Figure 5.13, respectively.

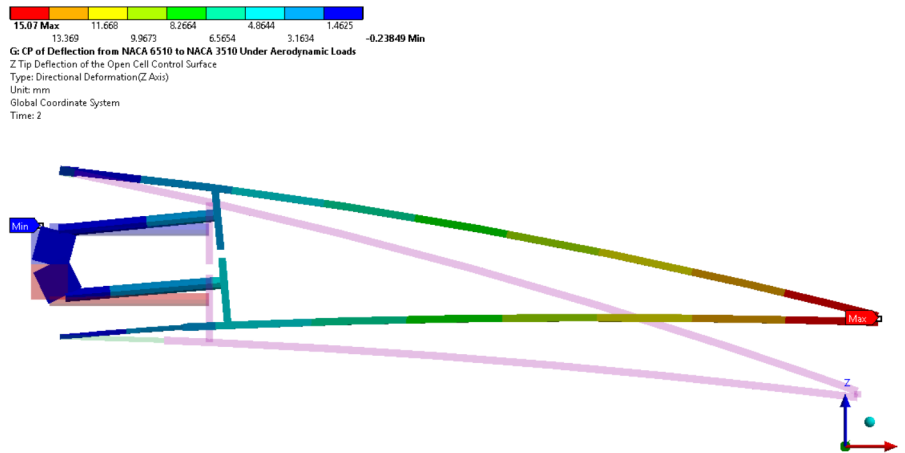


Figure 5.11: Displacement of the control surface in z direction while morphing from NACA 6510 to NACA 3510 profile under aerodynamic loads

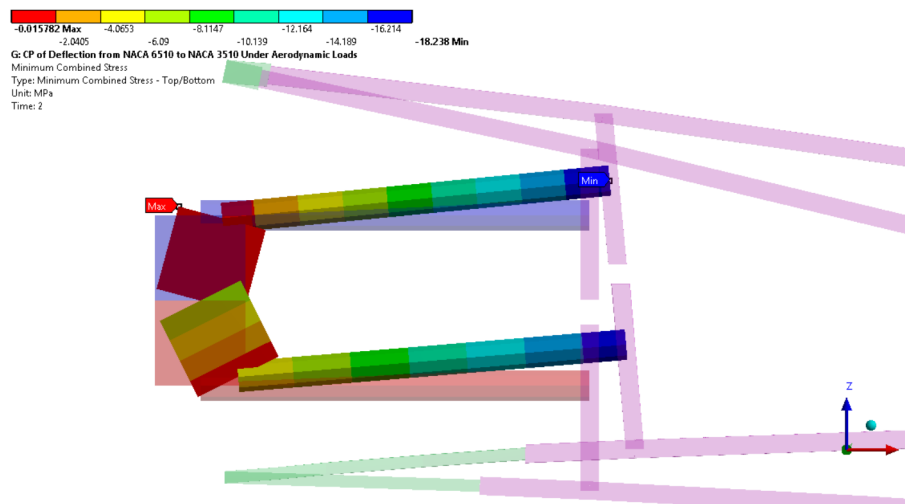


Figure 5.12: Minimum combined beam stress distribution while morphing from NACA 6510 to NACA 3510 profile under aerodynamic loads

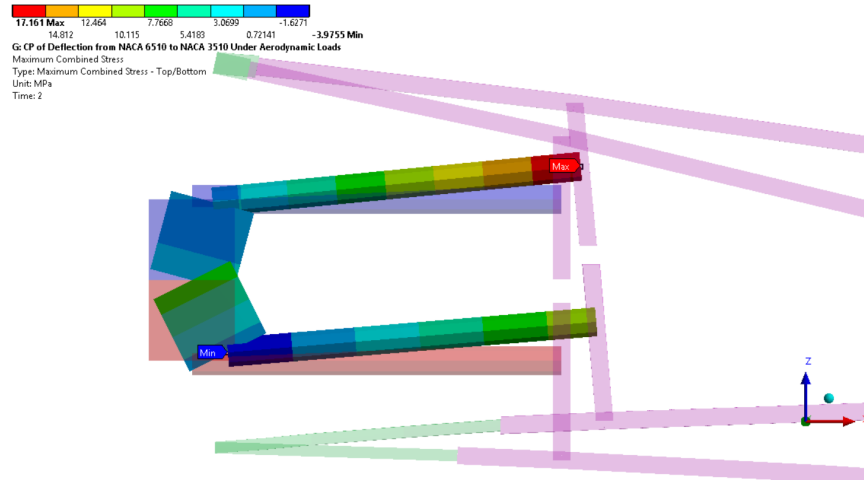


Figure 5.13: Maximum combined beam stress distribution while morphing from NACA 6510 to NACA 3510 profile under aerodynamic loads

As it can be seen from Table 5.4, the best design provides nearly 15.2 mm trailing edge tip deflection on the control surface. This value is requested for deflection of the control surface from NACA 6510 airfoil to NACA 3510 airfoil profile. Moreover, torque values of the servo actuators are lower than the maximum torque limits of the selected servo actuator. Besides, minimum and maximum combined stress values of the actuation rods and the moment arms of the servo actuators are lower than the yield stress of the aluminum presented in Table 3.3. In addition to these results, minimum normal strains of the compliant parts of the control surface are greater than zero, indicating that compliant parts are in tension.

5.3.3 Results of the Analysis of Deflection to NACA 2510 Airfoil Case

In this part, the analysis is conducted for the deflection of the control surface from NACA 6510 to NACA 2510 airfoil profile. Results of this analysis are shown in Table 5.5.

Table 5.5: Results of the finite element analysis of the deflection to NACA 2510 airfoil under aerodynamic loads

Deflected Airfoil	d_z [mm]	Q_t [Nmm]	Q_u [Nmm]	σ_{cmin} [MPa]	σ_{cmax} [MPa]	ϵ_{umin} [-]	ϵ_{lmin} [-]	ϵ_{umax} [-]	ϵ_{lmax} [-]
NACA 2510	20.52	257.07	36.04	-40.87	40.06	0.09	0.16	0.23	0.22

In Figure 5.14, the deflection of the control surface in z direction while morphing from base to NACA 2510 airfoil profile is presented for the finite element analysis of best design under the aerodynamic loads. Moreover, minimum and maximum combined stress of the moment arms and actuation rods are presented for the same analysis in Figure 5.15 and Figure 5.16, respectively.

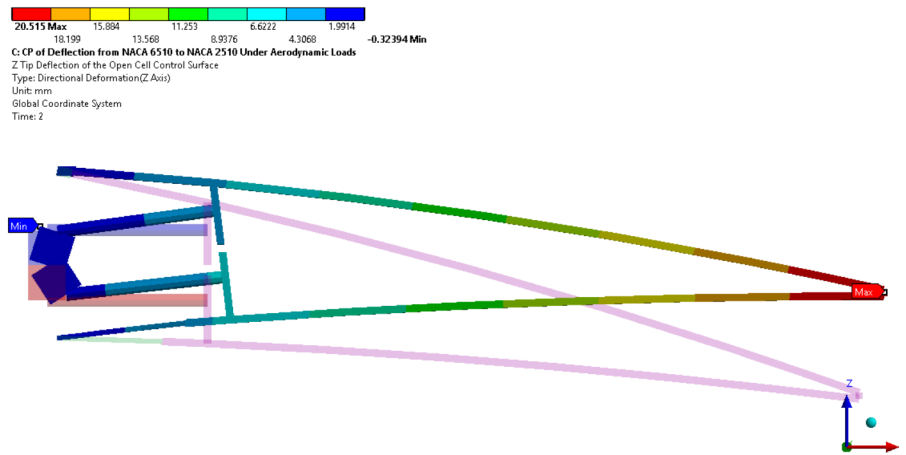


Figure 5.14: Displacement of the control surface in z direction while morphing from NACA 6510 to NACA 2510 profile under aerodynamic loads

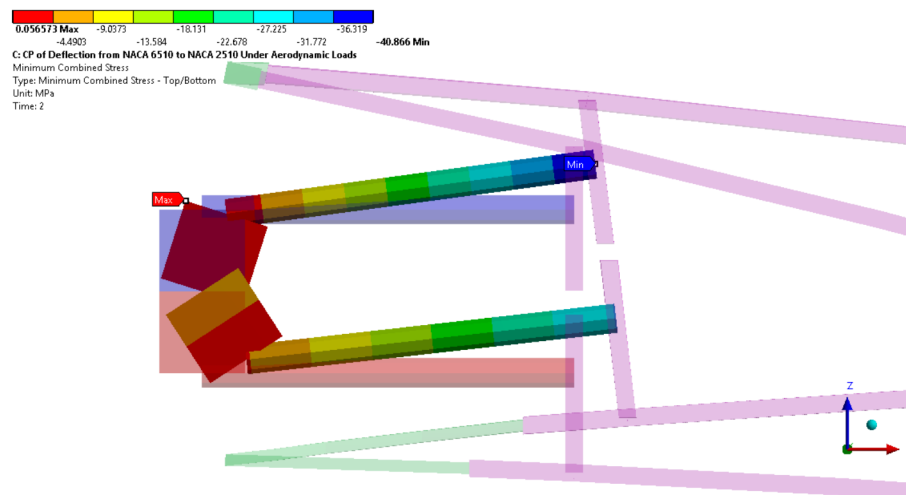


Figure 5.15: Minimum combined beam stress distribution while morphing from NACA 6510 to NACA 2510 profile under aerodynamic loads

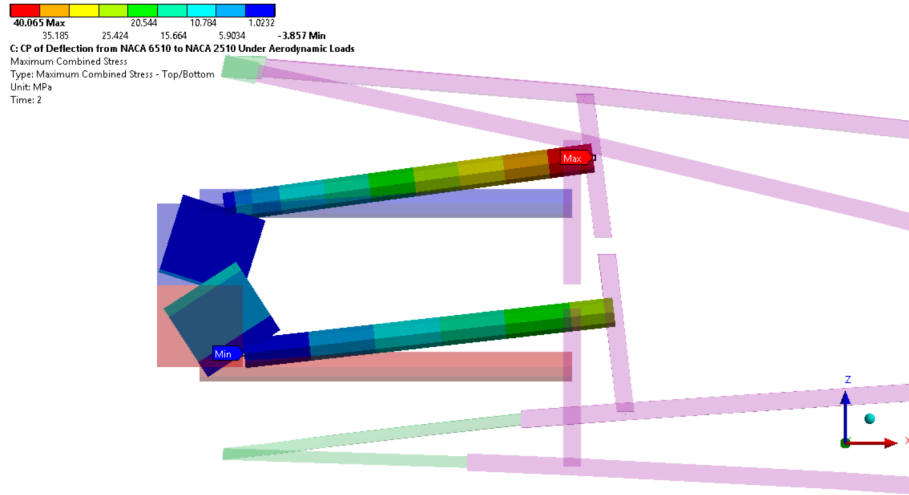


Figure 5.16: Maximum combined beam stress distribution while morphing from NACA 6510 to NACA 2510 profile under aerodynamic loads

As it can be seen from Table 5.5, the best design provides nearly 20.2 mm trailing edge tip deflection on the control surface. This value is requested for deflection of the control surface from NACA 6510 airfoil to NACA 2510 airfoil profile. Moreover, torque values of the servo actuators are lower than the maximum torque limits of the selected servo actuator. Besides, minimum and maximum combined stress values of the actuation rods and the moment arms of the servo actuators are lower than the yield stress of the aluminum presented in Table 3.3. In addition to these results, minimum normal strains of the compliant parts of the control surface are greater than zero, indicating that compliant parts are in tension.

5.4 Conclusion and Discussion

In this chapter, the optimum hybrid trailing edge control surface design is structurally analyzed under the aerodynamic loads. Three different analyses are considered in this part, due to the aimed flight cases of the unmanned aerial vehicle. First of them is the structural analysis of the control surface during maintaining the base profile, NACA 6510, of the wing under aerodynamic loads. Others are the analyses of the morphing of the control surface from NACA 6510 to NACA 3510 and NACA 2510 airfoil profiles. For this reason, pressure distributions are obtained for NACA 6510,

NACA 3510 and NACA 2510 airfoil profiles.

In the first section, calculation method of the aerodynamic loads, [1], is explained. Input parameters for the CFD analyses are given in the same section.

In the second section, the finite element analyses of the hybrid control surface under the aerodynamic loads are explained and the results are presented. The results show that the rotation applied to the servo actuators are lower than those in-vacuo conditions. This is because the generated lift force from flight and the deflection of the control surface are in the same direction. This situation makes the upward deflection of the control surface easier, so, decreases the rotation angle values.

Finally, it is shown that maintaining the NACA 6510 airfoil profile of the control surface and morphing it from NACA 6510 to both NACA 3510 and NACA 2510 are possible for the optimum design considering all the constraints and objectives in the optimization analysis under the aerodynamic loads.

CHAPTER 6

CONCLUSION AND FUTURE WORK

6.1 Conclusion

In this thesis, optimization analyses of the compliant parts of the hybrid control surface are presented. The base model of this control surface is taken from [1]. The control surface is modeled parametrically in Design Modeler tool of ANSYS Workbench v15.0. The optimization analyses of the model are conducted in Design Exploration tool of ANSYS Workbench v15.0.

Firstly, the compliant parts of the control surface is optimized for a morphing from NACA 6510 to NACA 2510 airfoil profile in terms of servo power, combined stresses of the beams and normal strains of the compliant parts. The maximum shape change is required for the deflection of the control surface from base profile to NACA 2510 airfoil profile. Therefore, the first optimization is conducted for this case as eight separate discrete optimizations. These discrete optimizations are for the open cell and closed cell designs with four different hyperelastic materials, neoprene rubber, sample elastomer-1, sample elastomer-2 and silicone. As a result of the optimization analyses, desired shape change of the control surface is not obtained for the sample elastomer-2 and silicone with the available torque of the selected servo actuator, while neoprene rubber and sample elastomer-1 can provide the requested shape change at this torque. This is due to relative stiffnesses of these materials as can be seen from Figure 3.8. According to the results of the optimization analyses which provide the desired tip deflection, compliant parts made from neoprene rubber require lower torque values than the compliant parts made from sample elastomer-1 due to the uniaxial stress strain behavior of these materials. Moreover, combined

beam stress values of the open cell control surface design are lower than the combined beam stress of the closed cell control surface design. For this reason, the open cell control surface design with compliant parts made from neoprene rubber material is chosen as the optimum design. The dimensions of the compliant parts of this best design can be seen from Table 6.1.

Table 6.1: The dimensions of the compliant parts of the best control surface design

t_l [mm]	t_u [mm]	L_l [mm]	L_u [mm]
1.00	1.90	21.00	3.00

Secondly, the optimum control surface design is structurally analyzed during the deflection of the control surface from NACA 6510 to NACA 3510 profile. Angle of rotations applied to the moment arms of the servo actuators are obtained from separate optimization analysis. In this optimization analysis, only rotation angles of the servo actuators for the upper and lower skin of the control surfaces are considered as variables. It was shown that the optimum design can successfully morph into NACA 3510 profile as well.

Thirdly, the optimum control surface design is structurally analyzed under the aerodynamic loads calculated in [1]. The analyses are conducted for the deflection of the control surface from NACA 6510 to both NACA 3510 and NACA 2510.

In conclusion, the selected control surface is capable of doing loiter, landing, take-off and cruise or high speed dash flight with a most efficient way in terms of torque of the servo actuators and combined beam stresses.

6.2 Key Findings

The aim of this study is to deflect the control surface in upward direction with a most efficient way. Therefore, the torque requirements of lower servo actuators are more than the upper servo actuators. According to the optimum design inputs and outputs, the torque results of the servo actuators decrease, when the lower compliant skin is

thinner and the upper compliant skin is thicker. The torque values also decrease when the upper compliant part is shorter and the lower compliant part is longer. With this deduction, it can be said that to generate more elongation with fewer forces, long and thin compliant parts are needed as expected.

Moreover, it is concluded that the neoprene rubber material is the most flexible and appropriate material among the considered materials to be use in the compliant skin for this design.

In addition, the optimum design belongs to the open cell control surface design. As can be seen from the results of candidate points, the stresses on the actuation mechanisms are much lower than the closed cell design, since open transmission parts have low stiffness than the closed one.

6.3 Future Work

In order to reduce the total weight, different materials such as composite materials can be used in the design of the rigid part and C-part of the control surface.

Compliant parts of the control surface can be designed by using shape memory materials. Because these materials are able to undergo large deformations like hyperelastic materials and recover their original shape at certain characteristic temperature [46].

Different maneuvering cases can be analyzed by using different aerodynamic loading.

Optimization of the locations and numbers of the servo actuators can be conducted. Also, different servo actuators can be tried. Servo actuators can be placed outside the torque box of the control surface instead of inside the torque box of the control surface as in this thesis.

REFERENCES

- [1] Tunçöz, İ. O., *Design and Analysis of a Hybrid Trailing Edge Control Surface of a Fully Morphing Unmanned Aerial Vehicle Wing*, Master's thesis, Middle East Technical University, 2015.
- [2] "CHANGE Project Summary," <http://change.tekever.com/partnership>, 2012, [Online; accessed 16-November-2016].
- [3] Abdulrahim, M. and Lind, R., "Using avian morphology to enhance aircraft maneuverability," AIAA Atmospheric Flight Mechanics Conference and Exhibit, Keystone, Colorado, 2006.
- [4] Bowman, J., Sanders, B., and Weisshaar, T., "Evaluating the impact of morphing technologies on aircraft performance," *AIAA paper*, Vol. 1631, 2002, pp. 2002.
- [5] Weisshaar, T. A., "Morphing aircraft technology-new shapes for aircraft design," Tech. rep., DTIC Document, 2006.
- [6] Eggleston, G., Hutchison, C., Johnston, C., Koch, B., Wargo, G., and Williams, K., "Morphing aircraft design team," *Virginia Tech Aerospace Engineering Senior Design Project*, 2002.
- [7] Barbarino, S., Bilgen, O., Ajaj, R. M., Friswell, M. I., and Inman, D. J., "A review of morphing aircraft," *Journal of Intelligent Material Systems and Structures*, Vol. 22, No. 9, 2011, pp. 823–877.
- [8] Smith, S. B. and Nelson, D. W., "Determination of the aerodynamic characteristics of the mission adaptive wing," *Journal of Aircraft*, Vol. 27, No. 11, 1990, pp. 950–958.
- [9] THORNTON, S., "Reduction of structural loads using maneuver load control on the Advanced Fighter Technology Integration(AFTI)/F-111 mission adaptive wing," 1993.
- [10] Gilyard, G. B., Georgie, J., and Barnicki, J. S., *Flight test of an adaptive configuration optimization system for transport aircraft*, Vol. 99, National Aeronautics and Space Administration, Dryden Flight Research Center, 1999.
- [11] Gern, F., Inman, D. J., and Kapania, R. K., "Computation of actuation power requirements for smart wings with morphing airfoils," *AIAA journal*, Vol. 43, No. 12, 2005, pp. 2481–2486.

- [12] Stanewsky, E., “Adaptive wing and flow control technology,” *Progress in Aerospace Sciences*, Vol. 37, No. 7, 2001, pp. 583–667.
- [13] Bowman, J., Sanders, B., Cannon, B., Kudva, J., Joshi, S., and Weisshaar, T., “Development of next generation morphing aircraft structures,” *AIAA*, Vol. 1730, 2007, pp. 2007.
- [14] Singh, V., Skiles, S. M., Krager, J. E., Wood, K. L., Jensen, D., and Sierakowski, R., “Innovations in design through transformation: A fundamental study of transformation principles,” *Journal of Mechanical Design*, Vol. 131, No. 8, 2009, pp. 081010.
- [15] Skillen, M. D. and Crossley, W. A., “Developing Morphing Wing Weight Predictors with Emphasis on the Actuating Mechanism,” *Proceedings of 47th AIAA/ASME/ASCE/AHS/ASC Structures, Structural Dynamics, and Materials Conference*, Vol. 1, No. 4, 2006, pp. 2006–2042.
- [16] Skillen, M. D. and Crossley, W. A., “Morphing Wing Weight Predictors and their Application in a Template-Based Morphing Aircraft Sizing Environment II, Part II: Morphing Aircraft Sizing via Multi-Level Optimization,” *NASA Report, CR-2008-214903*, 2008.
- [17] Shili, L., Wenjie, G., and Shujun, L., “Optimal design of compliant trailing edge for shape changing,” *Chinese Journal of Aeronautics*, Vol. 21, No. 2, 2008, pp. 187–192.
- [18] Akhras, G., “Smart materials and smart systems for the future,” *Canadian Military Journal*, Vol. 1, No. 3, 2000, pp. 25–31.
- [19] Barbarino, S., Dettmer, W. G., and Friswell, M. I., “Morphing trailing edges with shape memory alloy rods,” *Proceedings of 21st international conference on adaptive structures and technologies (ICAST)*, Vol. 4, No. 6, 2010.
- [20] Miura, K., Furuya, H., and Suzuki, K., “Variable geometry truss and its application to deployable truss and space crane arm,” *Acta Astronautica*, Vol. 12, No. 7, 1985, pp. 599–607.
- [21] Bartley-Cho, J. D., Wang, D. P., Martin, C. A., Kudva, J. N., and West, M. N., “Development of high-rate, adaptive trailing edge control surface for the smart wing phase 2 wind tunnel model,” *Journal of Intelligent Material Systems and Structures*, Vol. 15, No. 4, 2004, pp. 279–291.
- [22] Li, D., Guo, S., and Xiang, J., “Modeling and nonlinear aeroelastic analysis of a wing with morphing trailing edge,” *Proceedings of the Institution of Mechanical Engineers, Part G: Journal of Aerospace Engineering*, Vol. 227, No. 4, 2013, pp. 619–631.

- [23] Sinapius, M., Monner, H. P., Kintscher, M., and Riemenschneider, J., “DLR’s Morphing Wing Activities within the European Network,” *Procedia IUTAM Mechanics for the World: Proceedings of the 23rd International Congress of Theoretical and Applied Mechanics, ICTAM2012*, Vol. 10, 2014, pp. 416–426.
- [24] Hilbig, H. and Wagner, H., “Variable wing camber control for civil transport aircraft,” *Proceedings of the 15th Congress of the International Council of the Aeronautical Sciences*, 1984, pp. 107–112.
- [25] Campanile, L. and Sachau, D., “The belt-rib concept: a structronic approach to variable camber,” *Journal of Intelligent Material Systems and Structures*, Vol. 11, No. 3, 2000, pp. 215–224.
- [26] Ricci, S., “Adaptive camber mechanism for morphing-experiences at DIA-PoliMi,” *Advanced Course on Morphing Aircraft, Mechanisms and Systems, Lisbon, Portugal*, 2008.
- [27] Campanile, L. F. and Anders, S., “Aerodynamic and aeroelastic amplification in adaptive belt-rib airfoils,” *Aerospace Science and Technology*, Vol. 9, No. 1, 2005, pp. 55–63.
- [28] Spirlet, G., *Design of Morphing Leading and Trailing Edge Surfaces for Camber and Twist Control*, Ph.D. thesis, TU Delft, Delft University of Technology, 2015.
- [29] Seber, G., Sakarya, E., Insuyu, T. E., Unlusoy, L., Sahin, M., Ozgen, S., and Yaman, Y., “Aeroservoelastic Analysis of the Effects of Camber and Twist on Tactical UAV Mission-Adaptive Wings,” http://http://ae.metu.edu.tr/~yyaman/LabCapabilities/TUBITAK_107M103.pdf, 2011, [Online; accessed 03-April-2016].
- [30] Seber, G., Sakarya, E., Insuyu, T. E., Sahin, M., Ozgen, S., and Yaman, Y., “Evaluation of a Camber Morphing Concept Based on Controlled Flexibility,” 2009, IFASD2009, International Forum on Aeroelasticity and Structural Dynamics, 21-25 June 2009, Seattle, Washington, USA.
- [31] Kikuta, M. T., *Mechanical properties of candidate materials for morphing wings*, Ph.D. thesis, Virginia Polytechnic Institute and State University, 2003.
- [32] Monner, H., Breitbach, E., Bein, T., and Hanselka, H., “Design aspects of the adaptive wing-the elastic trailing edge and the local spoiler bump,” *Aeronautical Journal*, Vol. 104, No. 1032, 2000, pp. 89–95.
- [33] Thill, C., Etches, J., Bond, I., Potter, K., and Weaver, P., “Morphing skins,” *The Aeronautical Journal*, Vol. 112, No. 1129, 2008, pp. 117–139.
- [34] ANSYS, “Workbench, Material Library,” *ANSYS Inc., Canonsburg, PA*, 2015.
- [35] “Clinton Aluminum,” <http://www.clintonaluminum.com/wp-content/uploads/2014/08/Grade-6061-T6-T651-Text-Data1.pdf>.

- [36] “Volz Servos,” <http://www.volz-servos.com/English/13mmClass/>, [Online; accessed 05-December-2014].
- [37] ANSYS, “ANSYS Mechanical APDL Material Reference,” *ANSYS Inc., Canonsburg, PA*, 2015.
- [38] “INVENT GmbH,” <http://www.invent-gmbh.de/>.
- [39] “Cambridge University Engineering Department, Materials Data Book,” <http://www-mdp.eng.cam.ac.uk/web/library/enginfo/cueddatabooks/materials.pdf>, [Online; accessed 24-February-2014].
- [40] ANSYS, “ANSYS Design Exploration Users Guide,” *ANSYS Inc., Canonsburg, PA*, 2015.
- [41] Li, M., Li, G., and Azarm, S., “A kriging metamodel assisted multi-objective genetic algorithm for design optimization,” *Journal of Mechanical Design*, Vol. 130, No. 3, 2008, pp. 031401.
- [42] “Multi-Objective Optimization,” <http://cims.nyu.edu/~gn387/glp/lec1.pdf>, [Online; accessed 14-November-2016].
- [43] Arslan, P., Kalkan, U., Tıraş, H., Tunçöz, İ. O., Yang, Y., Gürses, E., Şahin, M., Özgen, S., and Yaman, Y., “Structural Analysis of an Unconventional Hybrid Control Surface of a Morphing Wing,” *ICAST2014: 25th International Conference on Adaptive Structures and Technologies*, 2014, pp. 06–08.
- [44] ANSYS, “ANSYS Workbench Help Documentation,” *ANSYS Inc., Canonsburg, PA*, 2015.
- [45] *Certification Specifications for Large Aeroplanes CS-25*, European Aviation Safety Agency Amendment 3, 2007.
- [46] Barbarino, S., Flores, E. S., Ajaj, R. M., Dayyani, I., and Friswell, M. I., “A review on shape memory alloys with applications to morphing aircraft,” *Smart Materials and Structures*, Vol. 23, No. 6, 2014, pp. 063001.

APPENDIX A

OPTIMIZATION RAW DATA

In this part, the raw data of the optimization study is given for the open cell control surface design with compliant parts made of neoprene rubber. The best design configuration has been chosen from these data by ANSYS package software. These data contains all the inputs and outputs of the optimization study from beginning. Table A.1 presents the values of input parameters of this raw data. Table A.2 shows the values of outputs corresponds to the input data which is given in Table A.1.

Table A.1: The input values of optimization design points for neoprene rubber compliant part of the open cell control surface

Design Point	R_{y_l} [degree]	R_{y_u} [degree]	t_l [mm]	t_u [mm]	L_l [mm]	L_u [mm]
1	-31.67	18.88	1.18	1.47	22.35	18.95
2	-36.02	17.01	1.04	1.69	24.05	14.77
3	-34.41	19.10	1.55	1.55	15.85	3.77
4	-32.51	17.51	1.35	1.77	24.95	13.01
5	-34.75	18.13	1.52	1.04	18.25	3.33
6	-33.42	17.30	1.75	1.91	19.25	23.57
7	-33.84	19.06	1.85	1.81	24.15	11.47
8	-33.35	19.17	1.89	1.42	15.55	14.99
9	-34.06	17.23	1.33	1.90	16.85	5.53
10	-31.75	17.41	1.72	1.50	16.75	6.63
11	-33.56	17.05	1.99	1.54	16.45	17.41
12	-36.51	19.64	1.77	1.72	20.05	5.97
13	-36.71	17.66	1.94	1.14	16.95	11.69
14	-32.79	18.63	1.70	1.19	24.65	16.09
15	-38.40	17.44	1.08	1.29	20.35	13.23

Table A.1 continued

Design Point	R_{y_l} [degree]	R_{y_u} [degree]	t_l [mm]	t_u [mm]	L_l [mm]	L_u [mm]
16	-32.58	16.29	1.14	1.56	20.55	15.43
17	-37.98	17.19	1.60	1.66	19.55	3.55
18	-34.47	16.94	1.97	1.73	23.55	16.97
19	-32.86	18.95	1.09	1.44	21.45	5.75
20	-36.23	18.02	1.25	1.00	23.15	8.83
21	-35.10	19.49	1.20	1.34	24.45	14.33
22	-34.20	16.97	1.06	1.16	22.55	18.73
23	-35.03	18.34	1.01	1.58	22.45	23.35
24	-35.66	18.45	1.03	1.92	20.85	7.73
25	-35.59	17.95	1.66	1.43	15.35	24.67
26	-33.70	17.33	1.79	1.62	23.85	4.43
27	-37.91	17.37	1.91	1.25	21.55	19.17
28	-32.65	17.87	1.76	1.03	17.25	17.19
29	-34.27	19.03	1.26	1.84	18.45	24.23
30	-31.95	19.28	1.38	1.80	17.75	10.15
31	-35.52	16.40	1.93	1.68	18.85	8.39
32	-37.48	17.73	1.21	1.53	15.65	7.07
33	-37.06	16.43	1.67	1.48	24.35	12.35
34	-36.92	18.52	1.78	1.59	24.75	20.49
35	-32.38	16.47	1.65	1.89	20.65	12.13
36	-35.17	16.79	1.62	1.37	15.25	6.19
37	-35.81	18.74	1.84	1.06	19.05	22.25
38	-31.88	16.58	1.80	1.31	21.15	11.25
39	-32.23	18.27	1.25	1.26	15.45	10.59
40	-33.63	19.71	1.27	1.83	22.95	13.45
41	-35.73	16.22	1.75	1.27	18.05	20.93
42	-34.55	18.09	1.81	2.00	17.85	6.85
43	-33.98	18.16	1.00	1.75	16.05	13.89
44	-33.14	18.49	1.59	1.78	23.95	23.13
45	-36.30	16.25	1.12	1.70	18.95	9.71
46	-35.31	19.46	1.98	1.33	22.65	14.55
47	-33.28	18.31	1.13	1.21	17.35	22.47
48	-36.16	17.80	1.31	1.09	15.05	15.65

Table A.1 continued

Design Point	R_{y_l} [degree]	R_{y_u} [degree]	t_l [mm]	t_u [mm]	L_l [mm]	L_u [mm]
49	-38.33	16.65	1.41	1.64	21.25	20.27
50	-32.30	17.08	1.23	1.52	19.95	4.21
51	-34.89	17.15	1.02	1.20	18.15	7.51
52	-37.13	16.51	1.63	1.75	16.15	16.75
53	-36.99	17.26	1.37	1.05	19.75	22.91
54	-37.84	19.24	1.10	1.65	21.75	15.87
55	-36.09	17.59	1.16	1.50	23.75	3.99
56	-36.64	19.53	1.30	1.86	17.15	10.37
57	-32.93	19.75	1.74	1.51	20.45	21.37
58	-36.37	19.60	1.64	1.94	20.95	18.51
59	-32.72	17.12	1.36	1.23	24.55	9.49
60	-32.02	16.90	1.45	1.36	19.65	23.79
61	-31.81	18.59	1.87	1.87	19.85	14.11
62	-31.60	18.38	1.51	1.60	16.55	21.59
63	-38.12	16.61	1.54	1.17	18.35	11.03
64	-33.49	18.67	1.47	1.88	21.95	3.11
65	-37.34	17.91	1.96	1.85	21.85	10.81
66	-34.61	16.54	1.48	1.63	23.25	24.01
67	-37.63	18.23	1.86	1.67	15.95	9.93
68	-33.91	18.81	1.44	1.12	22.25	24.45
69	-35.95	16.83	1.11	1.45	17.05	21.81
70	-32.44	17.84	1.95	1.40	21.35	22.03
71	-34.96	19.31	1.58	1.25	23.45	4.65
72	-37.77	18.05	1.83	1.28	22.85	6.41
73	-37.41	19.13	1.46	1.49	21.05	24.89
74	-36.78	19.42	1.92	1.61	17.95	19.61
75	-38.05	19.21	1.61	1.15	22.75	15.21
76	-33.77	18.56	2.00	1.41	19.15	5.09
77	-37.27	17.55	1.88	1.79	19.45	22.69
78	-31.54	18.92	1.68	1.39	22.05	7.29
79	-35.88	16.69	1.50	1.95	23.05	8.61
80	-35.38	19.35	1.05	1.30	17.65	7.95
81	-33.21	16.36	1.40	1.11	17.55	13.67

Table A.1 continued

Design Point	R_{y_l} [degree]	R_{y_u} [degree]	t_l [mm]	t_u [mm]	L_l [mm]	L_u [mm]
82	-34.34	19.78	1.28	1.46	16.25	18.29
83	-35.24	16.87	1.24	1.97	18.55	21.15
84	-33.07	16.72	1.43	1.74	15.15	16.31
85	-36.58	17.98	1.39	1.98	23.65	19.83
86	-38.19	18.99	1.29	1.38	20.15	5.31
87	-36.44	19.39	1.19	1.08	19.35	18.07
88	-37.56	18.77	1.49	1.76	24.25	8.17
89	-35.45	16.33	1.50	1.22	21.65	4.87
90	-37.20	17.62	1.34	1.24	24.85	19.39
91	-36.85	19.57	1.71	1.18	17.45	9.05
92	-34.82	18.70	1.69	1.96	15.75	17.85
93	-32.16	18.20	1.22	1.01	20.75	12.79
94	-33.00	19.67	1.56	1.10	18.65	11.91
95	-34.68	17.48	1.90	1.02	22.15	9.27
96	-34.13	16.76	1.73	1.13	23.35	20.05
97	-32.09	17.77	1.15	1.93	20.25	16.53
98	-38.26	17.69	1.42	1.99	18.75	12.57
99	-37.70	18.41	1.17	1.71	16.65	20.71
100	-38.47	18.85	1.53	1.35	16.35	17.63
101	-34.96	19.31	1.58	1.24	23.45	4.32
102	-37.84	19.24	1.10	1.65	21.75	16.20
103	-33.66	18.95	1.08	1.44	21.45	5.40
104	-32.84	19.71	1.28	1.83	22.95	13.80
105	-35.66	18.45	1.05	1.92	20.85	7.95
106	-37.41	19.13	1.44	1.49	21.05	24.67
107	-36.04	16.82	1.08	1.69	17.75	9.99
108	-31.93	19.47	1.34	1.82	24.05	14.93
109	-36.85	17.22	1.02	1.19	17.94	6.88
110	-34.97	18.46	1.78	1.59	24.96	21.12
111	-33.91	17.23	1.22	1.90	16.85	5.53
112	-32.45	17.08	1.33	1.52	19.95	4.21
113	-31.67	18.66	1.18	1.47	21.97	3.21
114	-33.49	18.88	1.47	1.88	22.33	18.85

Table A.1 continued

Design Point	R_{y_l} [degree]	R_{y_u} [degree]	t_l [mm]	t_u [mm]	L_l [mm]	L_u [mm]
115	-33.88	17.22	1.35	1.77	24.95	6.21
116	-32.69	17.52	1.33	1.90	16.85	12.33
117	-33.63	19.72	1.28	1.81	23.05	13.74
118	-34.31	16.92	1.38	1.72	17.75	10.15
119	-32.12	19.30	1.97	1.81	23.55	16.97
120	-35.54	18.15	1.00	1.75	16.05	7.72
121	-34.11	18.46	1.03	1.92	20.85	13.90
122	-36.12	18.02	1.25	1.00	23.15	8.83
123	-31.64	18.92	1.68	1.39	22.05	7.29
124	-37.84	18.96	1.10	1.43	21.42	15.87
125	-32.86	19.24	1.09	1.65	21.78	5.75
126	-37.13	17.07	1.46	1.48	21.05	6.84
127	-34.34	19.26	1.33	1.90	16.85	23.58
128	-33.63	19.71	1.27	1.34	23.17	13.49
129	-35.10	19.49	1.20	1.82	24.23	14.29
130	-35.64	18.45	1.04	1.43	20.85	5.79
131	-32.89	18.95	1.08	1.92	21.45	7.69
132	-34.82	17.16	1.05	1.18	18.15	7.51
133	-31.82	17.40	1.69	1.51	16.75	6.63
134	-37.84	19.24	1.07	1.65	21.60	15.87
135	-34.47	16.94	1.99	1.73	23.70	16.97
136	-34.47	16.94	1.56	1.56	23.55	4.37
137	-34.41	19.10	1.96	1.72	15.85	16.37
138	-34.64	17.77	1.15	1.93	20.25	16.54
139	-31.93	16.94	1.97	1.73	23.55	16.96
140	-36.51	18.68	1.48	1.72	20.06	5.97
141	-33.49	19.63	1.76	1.87	21.94	3.11
142	-36.88	16.94	1.69	1.15	16.90	16.9
143	-34.47	19.57	1.98	1.75	24.10	9.05
144	-36.94	19.57	1.58	1.18	17.77	9.05
145	-34.88	19.31	1.70	1.25	23.13	4.65
146	-35.10	18.62	1.19	1.83	21.78	3.62
147	-33.49	19.54	1.47	1.87	24.40	13.77

Table A.1 continued

Design Point	R_{y_l} [degree]	R_{y_u} [degree]	t_l [mm]	t_u [mm]	L_l [mm]	L_u [mm]
148	-32.45	16.99	1.34	1.52	19.95	3.23
149	-33.49	18.76	1.46	1.88	21.95	4.09
150	-33.71	17.31	1.47	1.66	21.95	3.10
151	-33.49	18.69	1.78	1.83	23.85	4.43
152	-33.49	17.05	1.76	1.87	21.92	3.15
153	-34.20	19.55	1.06	1.16	22.56	18.69
154	-35.10	17.34	1.20	1.82	23.84	14.29
155	-33.70	19.49	1.79	1.62	24.24	4.43
156	-33.90	17.25	1.22	1.90	16.85	3.01
157	-33.51	18.64	1.47	1.88	21.95	5.62
158	-33.91	17.15	1.22	1.22	16.85	5.53
159	-34.82	17.23	1.05	1.85	18.15	7.51
160	-38.19	17.70	1.15	1.39	20.15	5.31
161	-36.09	18.87	1.30	1.49	23.75	3.99
162	-34.88	18.98	1.07	1.26	21.44	4.65
163	-33.66	19.29	1.72	1.42	23.14	5.40
164	-36.74	18.45	1.03	1.92	20.85	7.73
165	-35.43	19.64	1.77	1.72	20.05	5.97
166	-32.72	17.06	1.35	1.17	24.55	3.06
167	-33.49	18.72	1.47	1.93	21.95	9.54
168	-37.56	18.77	1.49	1.76	16.87	5.42
169	-33.91	17.23	1.22	1.90	24.23	8.28
170	-32.45	17.08	1.33	1.55	19.95	4.18
171	-37.51	19.25	1.05	1.65	21.75	15.87
172	-33.82	19.62	1.81	1.87	21.94	3.11
173	-35.93	16.99	1.01	1.69	24.05	14.77
174	-35.66	18.44	1.04	1.44	20.82	7.95
175	-36.09	16.92	1.16	1.53	17.96	3.99
176	-34.31	17.59	1.38	1.70	23.54	10.15
177	-35.51	18.15	1.00	1.75	16.05	8.55
178	-34.01	18.16	1.00	1.75	16.05	13.07
179	-33.50	18.67	1.33	1.52	19.96	3.14
180	-32.44	17.08	1.46	1.88	21.94	4.18

Table A.1 continued

Design Point	R_{y_l} [degree]	R_{y_u} [degree]	t_l [mm]	t_u [mm]	L_l [mm]	L_u [mm]
181	-34.41	17.22	1.32	1.55	15.85	3.74
182	-34.06	19.11	1.56	1.90	16.85	5.56
183	-34.41	16.94	1.23	1.53	19.63	4.37
184	-32.37	17.08	1.56	1.56	23.87	4.21
185	-32.89	17.25	1.03	1.18	21.45	7.53
186	-34.89	18.87	1.08	1.93	18.15	7.68
187	-33.32	19.72	1.00	1.75	21.69	8.25
188	-35.70	17.27	1.05	1.85	18.17	7.52
189	-34.79	18.41	1.05	1.92	20.83	7.93
190	-35.64	18.45	1.04	1.42	20.85	5.79
191	-32.88	19.67	1.74	1.87	21.92	7.50
192	-35.39	18.45	1.03	1.92	20.85	3.06
193	-33.00	17.06	1.35	1.17	24.55	7.73
194	-35.61	17.14	1.05	1.16	20.84	3.03
195	-32.78	18.38	1.35	1.92	24.56	7.97
196	-35.70	18.67	1.06	1.88	20.75	3.70
197	-33.46	18.45	1.44	1.92	22.05	7.14
198	-35.30	18.27	1.00	1.65	21.78	5.72
199	-33.07	19.12	1.09	1.75	16.05	8.58
200	-35.64	18.45	1.04	1.43	20.85	5.79
201	-35.64	18.45	1.04	1.43	20.85	5.79
202	-32.86	18.96	1.09	1.91	21.48	3.95
203	-36.09	17.59	1.16	1.50	23.75	5.79
204	-35.66	17.40	1.03	1.92	20.85	5.46
205	-34.06	18.27	1.33	1.90	16.85	7.80
206	-33.49	18.75	1.47	1.88	22.12	3.22
207	-36.05	17.25	1.22	1.51	16.49	3.00
208	-33.94	17.59	1.16	1.89	24.20	4.00
209	-35.66	18.48	1.03	1.65	20.85	5.61
210	-32.86	19.21	1.09	1.92	21.78	7.87
211	-35.67	18.98	1.07	1.24	20.83	4.65
212	-34.87	18.45	1.03	1.93	21.45	7.73
213	-33.87	19.24	1.10	1.66	21.78	3.02

Table A.1 continued

Design Point	R_{y_l} [degree]	R_{y_u} [degree]	t_l [mm]	t_u [mm]	L_l [mm]	L_u [mm]
214	-32.90	17.25	1.21	1.89	16.85	5.74
215	-35.65	18.62	1.19	1.46	20.79	3.62
216	-35.09	18.45	1.04	1.80	21.84	5.79
217	-35.56	18.67	1.47	1.88	20.76	3.13
218	-33.50	18.91	1.11	1.92	21.46	3.30
219	-35.39	17.36	1.79	1.62	21.37	4.48
220	-33.43	18.24	1.00	1.65	24.26	5.67
221	-35.51	18.18	1.01	1.74	16.11	3.25
222	-33.50	19.60	1.76	1.88	21.87	8.41
223	-33.50	18.91	1.11	1.92	21.47	3.30
224	-36.23	17.30	1.22	1.53	16.85	3.01
225	-35.65	18.15	1.00	1.72	16.05	7.91
226	-35.52	18.45	1.05	1.94	20.85	8.58
227	-32.79	18.40	1.05	1.44	24.51	5.71
228	-33.94	17.59	1.35	1.89	24.20	3.96
229	-35.30	18.25	1.00	1.91	21.78	5.61
230	-33.94	17.65	1.01	1.63	21.52	4.00
231	-35.30	18.21	1.15	1.91	24.46	5.72
232	-36.09	18.87	1.30	1.86	23.73	4.00
233	-33.92	17.59	1.35	1.89	24.05	4.00
234	-35.70	18.49	1.03	1.60	20.85	3.63
235	-35.67	18.65	1.06	1.92	20.75	5.67
236	-35.10	18.67	1.46	1.83	21.78	3.61
237	-34.46	18.87	1.32	1.49	23.75	3.99
238	-35.64	18.45	1.03	1.92	20.85	7.95
239	-33.49	17.60	1.01	1.63	21.50	3.01
240	-35.30	18.45	1.04	1.92	20.85	3.06
241	-35.70	17.21	1.06	1.88	20.75	3.70
242	-33.78	17.25	1.35	1.90	16.85	3.06
243	-35.25	18.77	1.19	1.83	21.78	3.62
244	-33.36	19.42	1.76	1.87	22.03	3.11
245	-33.90	17.25	1.15	1.90	16.85	3.06
246	-33.92	17.25	1.38	1.90	16.85	3.10

Table A.1 continued

Design Point	R_{y_l} [degree]	R_{y_u} [degree]	t_l [mm]	t_u [mm]	L_l [mm]	L_u [mm]
247	-33.90	17.34	1.16	1.88	16.85	3.10
248	-36.09	18.87	1.80	1.86	23.73	4.00
249	-35.65	18.42	1.02	1.87	21.94	3.11
250	-33.92	17.25	1.37	1.90	16.85	3.06
251	-33.60	19.58	1.76	1.90	22.03	3.11
252	-33.93	17.56	1.21	1.89	24.20	3.18
253	-35.70	18.67	1.10	1.88	21.85	3.10
254	-33.48	17.25	1.19	1.89	16.85	3.10
255	-33.92	17.25	1.37	1.90	16.85	3.06
256	-33.90	18.62	1.38	1.89	21.93	3.11
257	-33.78	17.25	1.35	1.90	21.99	3.06
258	-35.10	18.63	1.16	1.87	21.78	3.62
259	-36.04	19.62	1.04	1.87	20.80	3.48
260	-33.90	17.24	1.00	1.83	16.85	3.01
261	-35.10	18.62	1.16	1.88	21.78	3.62
262	-35.56	18.45	1.03	1.92	20.85	7.73
263	-35.26	17.25	1.19	1.83	21.78	3.09
264	-35.21	18.25	1.04	1.88	16.87	5.61
265	-33.90	17.25	1.32	1.90	21.76	3.06
266	-33.90	17.14	1.00	1.90	16.85	3.00
267	-33.90	17.25	1.01	1.83	16.85	3.06
268	-35.65	18.42	1.02	1.87	16.94	3.11
269	-33.90	17.25	1.35	1.90	21.84	3.06
270	-35.10	18.63	1.19	1.89	21.78	3.62
271	-33.50	18.91	1.00	1.73	16.00	3.18
272	-33.94	18.62	1.16	1.88	21.46	3.12
273	-35.60	18.91	1.00	1.92	21.36	3.10
274	-33.55	18.40	1.04	1.43	20.84	5.79
275	-35.71	18.45	1.03	1.92	21.06	3.01
276	-33.85	17.25	1.36	1.89	21.85	7.76
277	-33.94	18.62	1.00	1.88	17.79	3.12
278	-33.76	17.25	1.16	1.90	21.01	3.38
279	-33.92	18.63	1.19	1.89	21.95	3.10

Table A.1 continued

Design Point	R_{y_l} [degree]	R_{y_u} [degree]	t_l [mm]	t_u [mm]	L_l [mm]	L_u [mm]
280	-33.52	18.90	1.00	1.92	21.36	3.11
281	-35.23	17.25	1.00	1.90	16.84	3.02
282	-33.98	18.45	1.04	1.92	20.86	3.42
283	-35.60	18.45	1.03	1.92	20.85	3.01
284	-33.96	17.24	1.01	1.83	16.85	7.73
285	-33.50	18.91	1.00	1.92	21.36	3.10
286	-33.50	18.91	1.00	1.92	21.57	3.10
287	-35.66	18.45	1.03	1.92	21.06	7.71
288	-33.90	17.24	1.35	1.90	16.85	3.02
289	-33.50	19.62	1.12	1.92	21.94	3.11
290	-33.79	18.91	1.00	1.87	21.36	3.10
291	-33.52	18.90	1.00	1.92	21.36	3.11
293	-35.60	18.91	1.00	1.92	21.36	3.10
294	-33.90	17.25	1.00	1.83	16.85	3.05
295	-33.94	18.62	1.00	1.88	17.79	3.12
296	-33.90	17.25	1.16	1.90	16.84	3.10
297	-33.90	17.25	1.01	1.89	16.85	3.03
298	-36.04	19.62	1.04	1.87	20.80	3.48
299	-33.93	17.56	1.21	1.89	24.20	3.18
300	-33.90	17.25	1.00	1.90	16.85	3.01
301	-33.79	19.62	1.12	1.87	21.94	3.11
302	-33.90	17.25	1.00	1.90	16.85	3.38
303	-35.56	18.67	1.47	1.88	20.76	3.13
304	-33.92	18.63	1.19	1.89	21.95	3.10
305	-33.90	17.24	1.01	1.83	17.34	3.01
306	-33.90	17.25	1.35	1.90	21.84	3.06
307	-33.90	17.34	1.16	1.92	16.85	3.10
308	-33.90	17.25	1.34	1.89	16.85	3.06
309	-33.92	17.34	1.16	1.88	16.85	3.10
310	-33.90	17.25	1.00	1.89	16.64	3.04
311	-33.94	18.63	1.19	1.89	21.95	3.12
312	-33.78	17.25	1.35	1.90	21.99	3.06
313	-33.90	17.25	1.01	1.83	16.85	3.06

Table A.1 continued

Design Point	R_{y_l} [degree]	R_{y_u} [degree]	t_l [mm]	t_u [mm]	L_l [mm]	L_u [mm]
314	-33.90	17.25	1.22	1.90	16.85	3.01
315	-33.90	17.24	1.01	1.83	16.85	3.01
316	-33.90	17.25	1.01	1.90	16.85	3.09
317	-33.90	17.25	1.16	1.90	16.85	3.10
318	-33.90	17.25	1.22	1.90	16.85	3.01
319	-33.92	17.25	1.37	1.90	16.85	3.06
320	-35.64	18.40	1.04	1.43	20.84	5.79
321	-33.82	19.62	1.30	1.87	21.94	3.11
322	-33.50	18.91	1.00	1.92	21.36	3.10
323	-33.98	18.45	1.04	1.92	20.86	3.42
324	-33.50	18.67	1	1.92	20.69	3.27
325	-36.04	19.62	1.04	1.87	20.95	3.52
326	-33.94	18.62	1.16	1.88	21.46	3.12
327	-35.10	18.63	1.19	1.89	21.78	3.62
328	-33.49	18.62	1.20	1.90	21.98	3.12
329	-35.66	18.45	1.03	1.92	20.85	7.73
330	-33.50	18.91	1.00	1.92	21.36	3.10
331	-35.51	18.15	1.00	1.75	16.05	8.55
332	-33.79	19.62	1.12	1.87	16.80	3.11
333	-33.50	18.91	1.11	1.92	21.46	3.30

Table A.2: The corresponding output values to the input values of optimization design points for neoprene rubber compliant part of the open cell control surface

Design Point	d_z [mm]	Q_l [Nmm]	Q_u [Nmm]	σ_{cmin} [MPa]	σ_{cmax} [MPa]	ϵ_{umin} [-]	ϵ_{lmin} [-]	ϵ_{umax} [-]	ϵ_{lmax} [-]
1	13.63	633.83	494.11	-65.26	80.29	0.06	0.14	0.08	0.19
2	22.26	653.57	541.58	-69.36	85.95	0.01	0.15	0.06	0.20
3	17.81	668.58	298.11	-44.98	37.16	0.22	0.22	0.26	0.28
4	16.95	639.63	473.32	-64.35	78.71	0.05	0.13	0.09	0.18
5	19.30	699.31	424.93	-45.96	59.08	0.20	0.20	0.26	0.25

Table A.2 continued

Design Point	d_z [mm]	Q_l [Nmm]	Q_u [Nmm]	σ_{cmin} [MPa]	σ_{cmax} [MPa]	ϵ_{umin} [-]	ϵ_{lmin} [-]	ϵ_{umax} [-]	ϵ_{lmax} [-]
6	17.90	783.75	585.88	-78.93	96.70	0.02	0.18	0.05	0.23
7	16.33	696.81	459.06	-58.76	72.84	0.08	0.13	0.12	0.19
8	14.92	834.33	575.26	-76.71	94.25	0.07	0.21	0.10	0.27
9	19.81	671.98	402.82	-49.43	61.76	0.10	0.21	0.14	0.26
10	16.09	736.99	448.67	-60.88	74.47	0.13	0.19	0.16	0.25
11	18.24	874.89	631.63	-86.97	106.09	0.03	0.21	0.06	0.27
12	19.34	709.76	396.75	-52.18	54.14	0.14	0.17	0.17	0.25
13	21.49	888.51	652.83	-85.33	105.34	0.04	0.22	0.07	0.28
14	15.25	707.59	543.67	-71.87	88.42	0.06	0.13	0.08	0.18
15	24.62	703.54	585.81	-71.80	89.91	0.01	0.19	0.05	0.25
16	18.69	670.04	537.51	-74.60	90.83	0.03	0.16	0.06	0.22
17	24.81	752.09	501.95	-52.00	67.62	0.04	0.20	0.15	0.26
18	19.86	786.38	593.81	-80.02	98.06	0.02	0.14	0.06	0.21
19	15.91	562.42	330.40	-48.76	48.20	0.17	0.15	0.20	0.20
20	20.98	680.40	538.52	-67.04	83.61	0.07	0.15	0.09	0.21
21	17.33	641.09	498.57	-60.53	75.92	0.06	0.14	0.09	0.19
22	19.75	664.58	561.38	-73.42	90.51	0.02	0.15	0.05	0.21
23	18.86	647.46	536.81	-66.22	82.71	0.02	0.16	0.06	0.21
24	20.18	601.86	400.19	-55.73	58.99	0.08	0.17	0.12	0.23
25	19.55	851.24	646.29	-82.93	102.70	0.02	0.23	0.05	0.29
26	19.22	667.48	383.39	-44.82	56.57	0.13	0.13	0.18	0.20
27	23.53	842.84	660.74	-83.28	103.61	0.01	0.16	0.04	0.25
28	15.89	811.06	611.23	-83.08	101.60	0.05	0.19	0.07	0.24
29	16.66	701.59	540.02	-67.81	84.37	0.03	0.19	0.06	0.23
30	13.84	636.98	380.77	-49.81	61.44	0.12	0.19	0.14	0.23
31	22.12	838.31	596.36	-80.05	98.20	0.04	0.19	0.07	0.25
32	23.14	734.47	532.60	-64.81	81.27	0.06	0.24	0.09	0.30
33	24.15	768.40	615.05	-80.28	99.10	0.01	0.14	0.05	0.22
34	20.73	762.96	594.99	-73.31	91.68	0.02	0.14	0.06	0.21
35	18.10	726.63	519.14	-73.43	89.09	0.04	0.15	0.08	0.22
36	21.25	812.60	558.46	-72.98	90.01	0.07	0.23	0.11	0.30
37	18.65	829.40	639.65	-80.45	100.10	0.03	0.19	0.06	0.24
38	17.11	754.44	553.33	-78.28	94.94	0.06	0.14	0.09	0.21

Table A.2 continued

Design Point	d_z [mm]	Q_l [Nmm]	Q_u [Nmm]	σ_{cmin} [MPa]	σ_{cmax} [MPa]	ϵ_{umin} [-]	ϵ_{lmin} [-]	ϵ_{umax} [-]	ϵ_{lmax} [-]
39	15.28	701.73	500.41	-67.67	82.86	0.09	0.22	0.12	0.26
40	15.28	621.07	428.57	-53.33	66.22	0.07	0.14	0.11	0.19
41	22.39	849.25	663.17	-87.74	107.91	0.01	0.20	0.04	0.26
42	18.90	747.23	428.56	-53.21	66.36	0.10	0.20	0.14	0.25
43	17.90	663.22	493.91	-64.43	79.53	0.05	0.22	0.09	0.26
44	15.96	699.08	537.04	-69.90	86.27	0.03	0.13	0.06	0.19
45	23.70	706.19	566.14	-74.42	91.71	0.02	0.20	0.06	0.25
46	17.21	776.62	565.52	-71.25	88.66	0.06	0.14	0.09	0.21
47	16.40	697.03	563.40	-72.82	89.99	0.03	0.20	0.06	0.24
48	20.80	788.46	616.66	-79.31	98.22	0.03	0.24	0.06	0.30
49	25.46	767.07	631.45	-78.87	98.31	-0.01	0.17	0.03	0.25
50	17.97	597.18	340.95	-40.84	51.24	0.15	0.17	0.20	0.21
51	20.67	666.23	512.15	-66.10	81.75	0.07	0.20	0.10	0.25
52	23.87	858.19	658.41	-86.65	106.78	0.00	0.23	0.04	0.30
53	22.73	761.75	626.30	-77.78	97.02	0.01	0.19	0.04	0.24
54	21.29	665.99	526.86	-64.67	77.63	0.03	0.17	0.07	0.23
55	22.15	605.77	397.87	-50.89	54.00	0.10	0.15	0.17	0.21
56	19.44	698.08	466.79	-59.16	69.39	0.07	0.22	0.12	0.27
57	13.65	740.28	546.48	-70.33	87.04	0.05	0.15	0.08	0.21
58	18.55	741.87	539.95	-65.80	82.52	0.04	0.16	0.07	0.23
59	17.75	657.17	501.10	-68.01	83.20	0.08	0.13	0.10	0.18
60	16.71	730.57	581.70	-79.06	96.61	0.02	0.17	0.05	0.21
61	14.15	735.06	486.14	-66.71	81.46	0.07	0.16	0.10	0.21
62	13.95	747.80	553.68	-75.21	91.98	0.04	0.20	0.07	0.24
63	25.13	821.46	650.65	-83.97	103.94	0.01	0.21	0.05	0.27
64	17.96	528.63	141.71	-42.41	25.28	0.23	0.15	0.29	0.21
65	22.31	805.94	575.49	-72.93	90.67	0.03	0.16	0.08	0.24
66	20.74	729.12	593.30	-77.76	95.80	0.01	0.14	0.04	0.21
67	22.04	870.87	600.88	-75.98	94.53	0.05	0.23	0.08	0.30
68	16.37	711.04	576.04	-72.43	90.06	0.03	0.15	0.06	0.20
69	22.14	728.94	599.75	-76.74	95.07	0.01	0.22	0.04	0.27
70	15.70	784.13	593.34	-80.01	97.99	0.03	0.14	0.06	0.21
71	17.93	641.01	378.78	-49.40	51.67	0.19	0.14	0.22	0.20

Table A.2 continued

Design Point	d_z [mm]	Q_l [Nmm]	Q_u [Nmm]	σ_{cmin} [MPa]	σ_{cmax} [MPa]	ϵ_{umin} [-]	ϵ_{lmin} [-]	ϵ_{umax} [-]	ϵ_{lmax} [-]
72	22.84	771.10	551.15	-66.16	83.23	0.07	0.15	0.11	0.23
73	20.47	746.80	595.17	-70.32	88.79	0.02	0.17	0.05	0.24
74	18.96	847.36	616.36	-76.69	95.73	0.04	0.20	0.07	0.26
75	21.23	756.87	593.71	-70.98	89.44	0.04	0.16	0.07	0.23
76	17.19	746.25	418.77	-49.88	62.75	0.17	0.18	0.21	0.23
77	22.42	850.48	649.11	-82.32	102.26	0.01	0.19	0.04	0.25
78	13.74	651.70	396.30	-51.51	63.58	0.16	0.14	0.18	0.19
79	22.55	712.08	528.23	-68.86	85.01	0.03	0.15	0.08	0.22
80	18.19	642.39	448.79	-57.71	66.57	0.11	0.21	0.14	0.25
81	19.15	756.02	593.04	-81.94	99.86	0.03	0.20	0.06	0.25
82	15.61	719.58	536.98	-67.31	83.82	0.05	0.22	0.08	0.26
83	21.20	724.74	577.67	-75.58	93.20	0.01	0.20	0.05	0.25
84	18.42	776.46	576.63	-80.04	97.47	0.03	0.23	0.06	0.28
85	21.34	704.90	557.74	-69.46	86.64	0.01	0.15	0.05	0.21
86	22.48	677.25	457.78	-59.89	62.49	0.11	0.18	0.15	0.25
87	18.97	704.60	568.75	-68.36	85.97	0.04	0.19	0.07	0.24
88	21.83	679.49	472.46	-57.31	69.05	0.07	0.15	0.11	0.21
89	22.55	725.93	536.05	-68.07	84.44	0.06	0.16	0.11	0.23
90	22.64	708.90	590.58	-72.65	90.85	0.01	0.15	0.04	0.21
91	19.19	796.42	556.07	-67.43	84.67	0.10	0.21	0.12	0.27
92	17.73	803.53	558.83	-73.33	90.44	0.04	0.22	0.07	0.28
93	15.25	664.45	521.94	-70.15	85.99	0.07	0.15	0.10	0.20
94	14.02	725.19	522.68	-67.72	83.71	0.10	0.18	0.12	0.22
95	19.40	784.00	582.84	-77.32	95.09	0.08	0.15	0.09	0.22
96	19.64	764.18	612.07	-81.49	100.07	0.02	0.14	0.05	0.21
97	15.98	641.39	479.59	-65.36	79.90	0.04	0.16	0.08	0.21
98	23.95	764.56	581.71	-72.70	90.67	0.01	0.21	0.07	0.26
99	22.07	739.21	586.77	-71.11	89.27	0.01	0.23	0.05	0.28
100	22.15	825.21	631.77	-76.96	96.57	0.02	0.24	0.06	0.29
101	17.99	635.67	366.35	-49.01	48.82	0.20	0.14	0.24	0.20
102	21.28	666.55	528.19	-64.70	77.82	0.03	0.17	0.07	0.23
103	16.98	567.19	334.21	-50.29	47.21	0.17	0.16	0.20	0.21
104	14.23	614.23	420.78	-53.07	65.98	0.08	0.14	0.11	0.19

Table A.2 continued

Design Point	d_z [mm]	Q_l [Nmm]	Q_u [Nmm]	σ_{cmin} [MPa]	σ_{cmax} [MPa]	ϵ_{umin} [-]	ϵ_{lmin} [-]	ϵ_{umax} [-]	ϵ_{lmax} [-]
105	20.15	607.11	406.99	-55.52	60.29	0.08	0.17	0.12	0.23
106	20.49	744.07	593.21	-70.09	88.50	0.02	0.17	0.05	0.24
107	22.57	696.23	542.57	-70.48	87.08	0.03	0.21	0.07	0.26
108	13.33	614.74	427.46	-55.67	68.73	0.07	0.13	0.10	0.18
109	23.12	686.50	538.31	-66.99	83.55	0.05	0.22	0.08	0.26
110	18.29	740.74	572.04	-72.76	90.29	0.03	0.13	0.06	0.19
111	19.69	648.99	390.73	-47.86	59.82	0.10	0.21	0.14	0.26
112	18.09	617.10	351.67	-42.15	52.88	0.15	0.17	0.20	0.22
113	15.39	498.49	176.37	-42.00	26.00	0.28	0.14	0.32	0.19
114	15.99	682.37	504.92	-65.29	80.73	0.04	0.15	0.08	0.20
115	19.59	617.52	404.83	-50.63	63.00	0.09	0.13	0.13	0.19
116	17.09	699.69	487.99	-66.96	81.76	0.05	0.20	0.09	0.25
117	15.25	622.29	432.55	-53.57	66.88	0.07	0.14	0.11	0.19
118	20.06	727.72	528.22	-70.94	87.01	0.05	0.20	0.08	0.25
119	13.44	717.36	494.69	-65.98	81.05	0.06	0.13	0.09	0.18
120	20.28	648.51	443.62	-55.23	67.51	0.08	0.23	0.11	0.28
121	17.76	621.96	459.86	-58.69	72.79	0.05	0.16	0.09	0.22
122	20.84	679.36	537.09	-66.97	83.50	0.07	0.15	0.09	0.21
123	13.93	644.32	388.05	-50.54	62.37	0.16	0.14	0.18	0.19
124	21.66	676.82	546.45	-64.26	81.25	0.03	0.17	0.07	0.23
125	15.68	537.19	278.53	-48.88	38.77	0.17	0.15	0.20	0.20
126	23.58	735.28	550.76	-68.81	85.75	0.04	0.17	0.08	0.24
127	16.36	724.74	542.98	-68.42	85.09	0.03	0.21	0.07	0.25
128	15.08	641.07	478.16	-59.67	74.37	0.08	0.14	0.11	0.19
129	17.50	624.62	457.42	-57.06	69.28	0.05	0.14	0.10	0.19
130	20.15	605.09	408.20	-55.12	58.63	0.12	0.17	0.15	0.23
131	15.97	556.10	315.78	-49.28	47.35	0.12	0.15	0.16	0.20
132	20.56	669.98	514.08	-66.51	82.21	0.07	0.20	0.10	0.25
133	16.20	733.41	446.43	-60.44	73.96	0.13	0.20	0.15	0.25
134	21.30	662.61	525.30	-64.91	77.32	0.03	0.17	0.07	0.23
135	19.85	788.78	594.90	-80.19	98.27	0.02	0.14	0.06	0.21
136	20.77	663.17	421.79	-49.56	62.49	0.10	0.14	0.16	0.21
137	16.39	853.58	582.17	-76.72	94.54	0.05	0.22	0.09	0.27

Table A.2 continued

Design Point	d_z [mm]	Q_l [Nmm]	Q_u [Nmm]	σ_{cmin} [MPa]	σ_{cmax} [MPa]	ϵ_{umin} [-]	ϵ_{lmin} [-]	ϵ_{umax} [-]	ϵ_{lmax} [-]
138	19.28	669.15	517.19	-67.17	82.99	0.03	0.17	0.07	0.23
139	16.58	753.02	555.10	-77.89	94.63	0.04	0.13	0.07	0.19
140	20.79	682.36	422.45	-52.88	60.02	0.11	0.17	0.15	0.24
141	16.63	540.16	90.93	-42.04	24.45	0.28	0.15	0.33	0.21
142	22.84	857.88	664.67	-86.47	106.81	0.01	0.22	0.04	0.28
143	16.52	701.96	428.29	-51.99	65.21	0.11	0.13	0.14	0.20
144	19.40	768.57	544.23	-65.31	82.20	0.10	0.21	0.12	0.26
145	17.76	661.84	386.47	-48.08	53.26	0.19	0.14	0.23	0.21
146	19.89	544.94	237.63	-49.05	31.29	0.17	0.16	0.23	0.22
147	15.27	638.90	437.99	-55.10	68.55	0.07	0.13	0.11	0.18
148	18.46	598.01	303.87	-37.79	42.10	0.18	0.17	0.24	0.22
149	17.50	558.57	213.53	-43.81	25.67	0.19	0.15	0.24	0.21
150	19.73	601.24	292.45	-39.72	37.09	0.17	0.15	0.23	0.21
151	17.36	605.11	259.68	-41.34	34.08	0.18	0.13	0.23	0.20
152	19.79	637.71	288.44	-35.56	37.13	0.15	0.15	0.22	0.22
153	15.93	640.66	522.49	-64.22	80.29	0.05	0.15	0.08	0.20
154	20.57	660.47	520.79	-67.65	83.57	0.02	0.15	0.07	0.20
155	16.40	603.93	264.42	-43.91	33.24	0.22	0.13	0.25	0.19
156	20.24	592.42	260.76	-41.58	31.44	0.16	0.21	0.23	0.26
157	17.31	599.19	302.62	-45.12	43.14	0.15	0.15	0.19	0.21
158	19.45	686.02	476.15	-60.83	75.35	0.11	0.21	0.14	0.26
159	20.70	641.68	450.27	-57.20	70.99	0.06	0.20	0.10	0.25
160	24.30	681.96	508.48	-58.73	73.96	0.06	0.19	0.11	0.25
161	20.42	589.62	329.99	-52.44	40.25	0.16	0.15	0.21	0.21
162	18.50	582.34	361.20	-53.01	48.97	0.18	0.16	0.21	0.22
163	16.25	643.75	357.58	-45.48	51.23	0.18	0.14	0.21	0.20
164	21.53	618.21	426.92	-58.30	62.18	0.07	0.18	0.11	0.23
165	18.00	691.57	369.87	-49.48	51.06	0.15	0.17	0.19	0.24
166	18.55	593.01	352.91	-39.52	49.81	0.20	0.13	0.25	0.19
167	16.70	642.88	403.64	-51.04	63.42	0.09	0.15	0.12	0.21
168	21.98	725.66	438.27	-54.90	60.47	0.10	0.23	0.15	0.28
169	19.51	618.71	433.44	-56.28	69.51	0.07	0.14	0.10	0.19
170	18.12	614.43	345.54	-41.19	51.74	0.15	0.17	0.20	0.22

Table A.2 continued

Design Point	d_z [mm]	Q_l [Nmm]	Q_u [Nmm]	σ_{cmin} [MPa]	σ_{cmax} [MPa]	ϵ_{umin} [-]	ϵ_{lmin} [-]	ϵ_{umax} [-]	ϵ_{lmax} [-]
171	20.89	655.27	518.84	-64.24	76.59	0.03	0.17	0.07	0.23
172	17.02	554.24	105.31	-42.23	24.14	0.28	0.15	0.33	0.21
173	22.20	647.45	538.39	-68.99	85.48	0.01	0.15	0.06	0.20
174	19.97	625.88	453.67	-56.49	68.36	0.09	0.17	0.12	0.23
175	22.91	669.96	456.98	-51.31	65.41	0.07	0.21	0.15	0.26
176	19.25	663.59	483.10	-62.93	77.69	0.06	0.14	0.09	0.20
177	20.19	651.74	454.82	-56.06	70.07	0.07	0.23	0.11	0.28
178	17.97	660.39	487.02	-63.45	78.34	0.05	0.22	0.09	0.26
179	17.66	561.80	224.28	-43.70	25.46	0.25	0.18	0.29	0.22
180	18.30	595.61	295.19	-38.02	43.22	0.14	0.15	0.19	0.21
181	20.38	680.29	393.40	-43.30	55.41	0.13	0.23	0.20	0.28
182	17.22	662.58	314.52	-45.83	44.04	0.16	0.21	0.20	0.26
183	20.75	642.55	415.86	-48.91	61.66	0.10	0.19	0.16	0.23
184	18.00	614.94	343.75	-41.12	51.61	0.15	0.13	0.20	0.19
185	18.01	616.49	462.52	-61.39	75.45	0.10	0.16	0.12	0.21
186	18.58	609.49	373.05	-53.88	54.77	0.10	0.20	0.14	0.24
187	15.35	550.12	328.26	-53.16	47.64	0.13	0.15	0.16	0.20
188	21.75	653.83	470.14	-58.85	73.29	0.05	0.21	0.10	0.25
189	19.10	595.96	388.75	-53.23	58.36	0.09	0.17	0.12	0.22
190	20.14	605.60	409.54	-55.16	58.87	0.12	0.17	0.15	0.23
191	14.69	634.88	324.98	-45.06	48.42	0.15	0.14	0.18	0.20
192	20.76	514.30	197.95	-49.75	33.03	0.17	0.17	0.25	0.23
193	18.26	654.01	490.98	-65.82	80.73	0.09	0.13	0.11	0.19
194	22.16	616.03	419.72	-49.16	56.73	0.12	0.17	0.20	0.23
195	16.51	589.29	353.51	-45.70	55.27	0.11	0.13	0.14	0.18
196	20.61	539.25	246.32	-51.92	34.32	0.16	0.17	0.22	0.23
197	17.29	619.28	356.95	-46.05	54.44	0.12	0.15	0.15	0.21
198	20.11	581.36	375.04	-53.44	53.31	0.11	0.16	0.15	0.22
199	15.68	619.06	378.43	-50.79	58.54	0.12	0.22	0.14	0.26
200	20.15	605.09	408.20	-55.13	58.63	0.12	0.17	0.15	0.23
201	20.15	605.09	408.20	-55.13	58.63	0.12	0.17	0.15	0.23
202	16.68	481.19	144.65	-46.24	30.75	0.21	0.15	0.26	0.20
203	21.88	629.04	451.42	-53.18	67.11	0.08	0.15	0.12	0.21

Table A.2 continued

Design Point	d_z [mm]	Q_l [Nmm]	Q_u [Nmm]	σ_{cmin} [MPa]	σ_{cmax} [MPa]	ϵ_{umin} [-]	ϵ_{lmin} [-]	ϵ_{umax} [-]	ϵ_{lmax} [-]
204	21.83	605.96	401.63	-51.86	58.62	0.07	0.17	0.13	0.23
205	18.12	671.97	412.26	-51.65	64.29	0.10	0.21	0.13	0.26
206	17.82	529.00	145.90	-42.74	25.60	0.23	0.15	0.29	0.21
207	22.60	668.00	402.84	-47.18	51.29	0.11	0.23	0.20	0.28
208	19.73	541.65	275.61	-45.09	36.33	0.14	0.14	0.19	0.19
209	20.28	589.99	373.38	-54.64	52.10	0.11	0.17	0.15	0.23
210	15.58	550.65	309.01	-49.83	45.87	0.13	0.15	0.16	0.20
211	19.49	598.16	382.58	-55.03	51.57	0.16	0.17	0.20	0.23
212	19.19	587.21	379.69	-53.46	56.43	0.09	0.16	0.13	0.22
213	17.70	480.15	136.08	-48.15	32.63	0.26	0.16	0.31	0.21
214	18.36	631.59	367.17	-46.29	57.49	0.11	0.21	0.15	0.25
215	20.28	591.09	323.98	-50.96	39.26	0.17	0.17	0.23	0.23
216	19.67	571.26	345.49	-52.77	48.28	0.11	0.16	0.16	0.21
217	20.45	584.59	223.94	-46.61	27.44	0.19	0.17	0.25	0.23
218	17.77	473.50	114.80	-46.67	31.41	0.23	0.16	0.28	0.21
219	21.20	724.00	444.19	-51.04	64.72	0.10	0.16	0.16	0.23
220	17.82	540.60	323.66	-48.74	47.01	0.14	0.14	0.17	0.19
221	20.99	577.18	278.99	-50.26	31.42	0.16	0.23	0.22	0.28
222	15.45	661.61	369.65	-46.67	55.96	0.13	0.15	0.16	0.21
223	17.77	473.73	114.03	-46.63	31.36	0.23	0.16	0.28	0.21
224	22.79	665.20	402.14	-47.70	50.78	0.10	0.22	0.20	0.28
225	20.40	652.58	451.91	-55.65	68.92	0.08	0.23	0.11	0.28
226	19.92	609.82	414.43	-55.44	62.13	0.07	0.17	0.11	0.23
227	16.63	548.89	339.78	-47.66	50.60	0.16	0.13	0.18	0.18
228	19.66	569.01	284.06	-43.18	37.67	0.14	0.14	0.19	0.20
229	20.29	566.31	340.28	-52.92	47.20	0.10	0.16	0.15	0.22
230	19.53	550.41	308.93	-47.05	41.80	0.15	0.16	0.20	0.21
231	20.29	575.98	348.72	-51.42	48.91	0.10	0.14	0.15	0.20
232	20.68	563.55	269.56	-51.76	33.27	0.15	0.15	0.21	0.21
233	19.62	570.93	286.10	-43.16	38.15	0.14	0.14	0.19	0.20
234	20.68	557.54	297.09	-52.13	34.67	0.16	0.17	0.22	0.23
235	20.17	577.51	334.60	-54.12	45.17	0.11	0.17	0.16	0.23
236	19.71	585.17	249.48	-46.49	27.63	0.18	0.16	0.23	0.22

Table A.2 continued

Design Point	d_z [mm]	Q_l [Nmm]	Q_u [Nmm]	σ_{cmin} [MPa]	σ_{cmax} [MPa]	ϵ_{umin} [-]	ϵ_{lmin} [-]	ϵ_{umax} [-]	ϵ_{lmax} [-]
237	18.37	568.87	290.32	-48.01	36.06	0.20	0.14	0.24	0.20
238	20.13	602.62	404.13	-55.80	59.81	0.08	0.17	0.12	0.23
239	19.31	518.15	237.29	-44.41	27.98	0.19	0.16	0.25	0.21
240	20.66	510.05	192.06	-49.92	33.36	0.17	0.17	0.25	0.23
241	22.40	591.91	358.15	-49.02	46.83	0.09	0.17	0.16	0.23
242	20.02	616.74	268.52	-39.84	33.04	0.16	0.21	0.23	0.26
243	19.87	542.26	231.17	-49.72	32.03	0.18	0.16	0.23	0.22
244	16.72	543.59	100.41	-41.26	23.58	0.28	0.14	0.33	0.21
245	20.26	580.72	259.52	-42.48	31.42	0.15	0.21	0.22	0.26
246	20.16	626.89	279.21	-39.86	34.61	0.15	0.21	0.22	0.26
247	20.13	581.71	259.05	-42.66	31.41	0.16	0.21	0.22	0.26
248	20.44	642.02	301.61	-46.69	35.39	0.16	0.14	0.21	0.21
249	21.09	513.58	215.36	-50.89	34.18	0.16	0.16	0.24	0.22
250	20.18	623.79	275.50	-39.89	33.86	0.16	0.21	0.23	0.26
251	16.84	540.57	91.56	-42.13	24.53	0.28	0.15	0.33	0.21
252	19.97	526.65	226.58	-43.36	26.34	0.16	0.14	0.23	0.20
253	20.81	519.73	202.39	-50.63	33.69	0.18	0.16	0.25	0.22
254	19.71	581.39	248.77	-41.11	30.68	0.16	0.21	0.23	0.26
255	20.18	622.45	275.10	-39.98	33.80	0.16	0.21	0.23	0.26
256	18.57	524.55	151.47	-43.94	26.93	0.22	0.15	0.28	0.21
257	20.12	568.35	250.68	-40.59	30.17	0.16	0.15	0.22	0.21
258	19.93	535.60	226.38	-49.37	31.92	0.17	0.16	0.23	0.22
259	19.93	501.78	172.47	-54.88	38.48	0.20	0.17	0.26	0.23
260	20.32	556.83	257.72	-44.16	30.97	0.15	0.22	0.22	0.26
261	19.94	535.93	226.96	-49.34	31.88	0.17	0.16	0.23	0.22
262	20.04	601.47	398.91	-55.24	58.87	0.08	0.17	0.12	0.23
263	21.93	583.82	315.44	-45.53	37.93	0.12	0.16	0.20	0.22
264	20.06	608.32	357.94	-52.41	50.67	0.11	0.22	0.15	0.26
265	20.27	567.71	254.16	-41.12	30.51	0.15	0.15	0.22	0.22
266	20.49	555.80	254.91	-43.96	30.63	0.15	0.22	0.22	0.26
267	20.30	558.60	260.45	-44.21	31.56	0.15	0.22	0.22	0.26
268	21.01	550.34	229.55	-50.77	32.81	0.17	0.22	0.24	0.27
269	20.26	572.11	255.82	-40.81	30.76	0.15	0.15	0.22	0.22

Table A.2 continued

Design Point	d_z [mm]	Q_l [Nmm]	Q_u [Nmm]	σ_{cmin} [MPa]	σ_{cmax} [MPa]	ϵ_{umin} [-]	ϵ_{lmin} [-]	ϵ_{umax} [-]	ϵ_{lmax} [-]
270	19.93	539.28	225.44	-49.04	31.47	0.17	0.16	0.23	0.22
271	17.61	511.59	155.52	-47.48	30.96	0.24	0.22	0.30	0.26
272	18.69	496.53	145.60	-46.20	30.15	0.22	0.16	0.28	0.21
273	20.47	491.31	165.54	-52.05	36.07	0.19	0.17	0.26	0.22
274	17.54	579.79	367.29	-49.72	54.50	0.14	0.16	0.17	0.21
275	21.18	514.41	202.23	-50.82	34.07	0.17	0.17	0.24	0.23
276	19.34	651.01	437.02	-56.79	70.12	0.07	0.15	0.11	0.21
277	18.70	497.53	146.70	-47.66	31.59	0.22	0.20	0.28	0.24
278	20.06	555.41	265.31	-42.97	33.67	0.14	0.16	0.21	0.22
279	18.66	495.00	139.78	-45.89	29.89	0.22	0.15	0.28	0.21
280	17.92	449.68	90.63	-47.63	33.18	0.23	0.16	0.30	0.21
281	21.95	582.87	303.32	-47.09	35.74	0.12	0.22	0.20	0.27
282	18.91	495.85	172.39	-47.46	31.45	0.19	0.16	0.25	0.22
283	21.05	513.15	198.01	-50.76	34.07	0.17	0.17	0.24	0.23
284	19.56	636.23	438.02	-56.72	70.10	0.07	0.21	0.11	0.26
285	17.90	448.72	88.66	-47.59	33.17	0.24	0.16	0.30	0.21
286	17.91	447.20	87.66	-47.60	33.23	0.24	0.16	0.30	0.21
287	20.19	599.99	398.58	-55.69	58.68	0.08	0.17	0.12	0.22
288	20.19	618.60	271.18	-39.98	33.08	0.16	0.21	0.23	0.26
289	16.97	437.83	42.73	-48.26	34.17	0.27	0.15	0.33	0.20
290	18.22	458.69	108.99	-48.19	33.42	0.23	0.16	0.29	0.21
291	17.92	449.68	90.63	-47.63	33.18	0.23	0.16	0.30	0.21
293	20.47	491.31	165.54	-52.05	36.07	0.19	0.17	0.26	0.22
294	20.30	557.66	259.70	-44.26	31.42	0.15	0.22	0.22	0.26
295	18.70	497.53	146.70	-47.66	31.59	0.22	0.20	0.28	0.24
296	20.24	585.23	263.62	-42.35	32.21	0.15	0.21	0.22	0.26
297	20.34	554.14	248.62	-44.07	29.62	0.15	0.22	0.22	0.26
298	19.93	501.78	172.47	-54.88	38.48	0.20	0.17	0.26	0.23
299	19.97	526.65	226.58	-43.36	26.34	0.16	0.14	0.23	0.20
300	20.35	552.26	246.64	-44.12	29.25	0.15	0.22	0.22	0.26
301	17.29	448.47	64.28	-48.83	34.37	0.27	0.15	0.32	0.21
302	20.23	563.85	273.22	-44.71	34.77	0.14	0.22	0.20	0.26
303	20.45	584.59	223.94	-46.61	27.44	0.19	0.17	0.25	0.23

Table A.2 continued

Design Point	d_z [mm]	Q_l [Nmm]	Q_u [Nmm]	σ_{cmin} [MPa]	σ_{cmax} [MPa]	ϵ_{umin} [-]	ϵ_{lmin} [-]	ϵ_{umax} [-]	ϵ_{lmax} [-]
304	18.66	495.00	139.78	-45.89	29.89	0.22	0.15	0.28	0.21
305	20.33	553.39	256.44	-44.14	30.76	0.15	0.21	0.22	0.25
306	20.26	572.11	255.82	-40.81	30.76	0.15	0.15	0.22	0.22
307	20.16	578.77	252.30	-42.62	30.36	0.16	0.21	0.22	0.26
308	20.17	616.70	272.23	-40.24	33.40	0.16	0.21	0.23	0.26
309	20.16	582.03	259.55	-42.70	31.45	0.16	0.21	0.22	0.26
310	20.34	554.89	249.05	-44.14	29.71	0.15	0.22	0.22	0.26
311	18.68	496.14	142.15	-45.94	29.90	0.22	0.15	0.28	0.21
312	20.12	568.35	250.68	-40.59	30.17	0.16	0.15	0.22	0.21
313	20.30	558.60	260.45	-44.21	31.56	0.15	0.22	0.22	0.26
314	20.24	592.42	260.76	-41.58	31.44	0.16	0.21	0.23	0.26
315	20.32	557.54	257.97	-44.12	31.01	0.15	0.22	0.22	0.26
316	20.32	555.58	253.14	-44.20	30.56	0.15	0.22	0.22	0.26
317	20.24	585.01	263.25	-42.35	32.15	0.15	0.21	0.22	0.26
318	20.24	592.35	260.73	-41.59	31.43	0.16	0.21	0.23	0.26
319	20.18	622.45	275.10	-39.98	33.80	0.16	0.21	0.23	0.26
320	20.21	605.47	409.49	-55.14	58.98	0.11	0.17	0.15	0.23
321	17.24	477.47	76.09	-47.07	31.61	0.27	0.15	0.32	0.21
322	17.90	448.72	88.66	-47.59	33.17	0.24	0.16	0.30	0.21
323	18.91	495.85	172.39	-47.46	31.45	0.19	0.16	0.25	0.22
324	18.11	468.52	123.95	-47.16	32.08	0.22	0.16	0.28	0.22
325	19.92	502.33	175.44	-54.92	38.50	0.19	0.17	0.26	0.23
326	18.69	496.53	145.60	-46.20	30.15	0.22	0.16	0.28	0.21
327	19.93	539.28	225.44	-49.04	31.47	0.17	0.16	0.23	0.22
328	18.15	487.88	126.25	-44.94	29.20	0.22	0.15	0.29	0.21
329	20.19	601.66	399.73	-55.72	58.91	0.08	0.17	0.12	0.23
330	17.90	448.50	88.18	-47.60	33.18	0.24	0.16	0.30	0.21
331	20.19	651.70	454.80	-56.05	70.06	0.07	0.23	0.11	0.28
332	17.19	488.67	80.06	-48.55	32.73	0.27	0.21	0.33	0.25
333	17.78	473.04	113.78	-46.67	31.43	0.23	0.16	0.28	0.21

APPENDIX B

EFFECT OF SAMPLE SIZE AND OPTIMIZATION METHOD ON BEST CANDIDATE POINT

In this part, four different analyses conducted are explained for the same optimization problem in order to evaluate the selected method, sizes of samples for initial and per iteration. The properties of cases are shown in Table B.1. In addition, Table B.2 presents the optimized input parameters of four different cases. Table B.3 shows the output variables of the optimization problem corresponding to the input data given in Table B.2. According to Table B.3, no significant difference is observed in the results. In addition to this, Case 1 is the fastest analysis among the others. Therefore, in this thesis, the properties of Case 1 are used in the optimization analyses.

Table B.1: The properties of different optimization cases

Case Name	Optimization Method	Number of Initial Samples	Number of Samples per Iteration
Case 1	AMO	100	50
Case 2	AMO	100	100
Case 3	MOGA	100	50
Case 4	AMO	150	50

Table B.2: The input values of each optimization analysis

Case Name	R_{yl} [degree]	R_{yu} [degree]	t_l [mm]	t_u [mm]	L_l [mm]	L_u [mm]
Case 1	-35.60	18.91	1.00	1.92	21.36	3.10
Case 2	-35.50	18.97	1.03	1.92	20.85	3.16
Case 3	-35.06	18.67	1.01	1.92	22.02	3.01
Case 4	-35.91	19.51	1.09	1.94	20.65	3.13

Table B.3: The output values corresponds to the input data of each optimization analysis

Case Name	d_z [mm]	Q_l [Nmm]	Q_u [Nmm]	σ_{cmin} [MPa]	σ_{cmax} [MPa]	ϵ_{umin} [-]	ϵ_{lmin} [-]	ϵ_{umax} [-]	ϵ_{lmax} [-]
Case 1	20.47	491.31	165.54	-52.05	36.07	0.19	0.17	0.26	0.22
Case 2	20.21	495.25	163.10	-51.75	35.65	0.19	0.17	0.26	0.23
Case 3	20.18	489.30	160.51	-50.15	35.06	0.20	0.16	0.26	0.21
Case 4	20.07	493.55	144.66	-53.38	37.28	0.21	0.17	0.28	0.23

APPENDIX C

VISUALIZATION OF PARETO FRONTS OF OBJECTIVE FUNCTIONS

In this part, Pareto fronts of three objective functions are presented with two dimensional plots together with optimization raw data in Figures C.1, C.2 and C.3. These figures belong to the optimization analysis of the open cell control surface with neoprene rubber compliant parts.

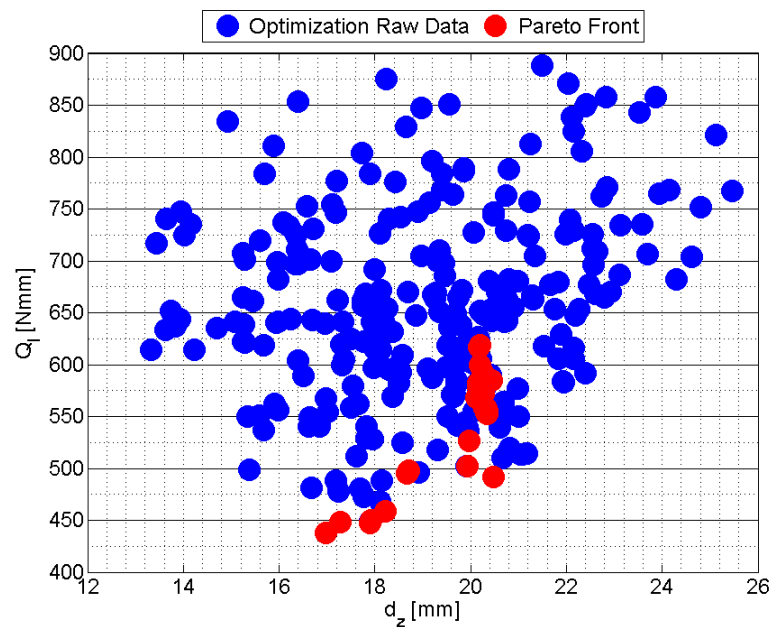


Figure C.1: Comparison of raw data and Pareto Front for torque reaction of the servo to actuate the lower part and tip deflection of the control surface in z-direction

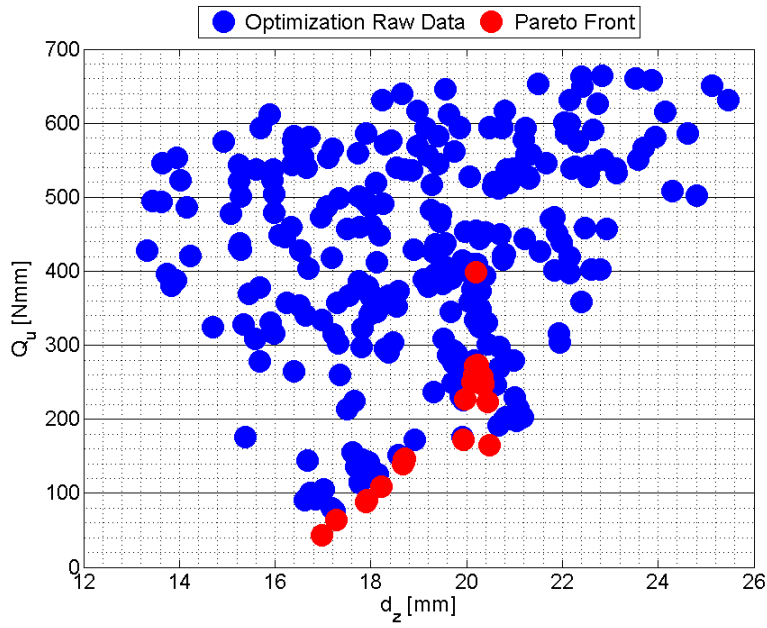


Figure C.2: Comparison of raw data and Pareto Front for torque reaction of the servo to actuate the upper part and tip deflection of the control surface in z-direction

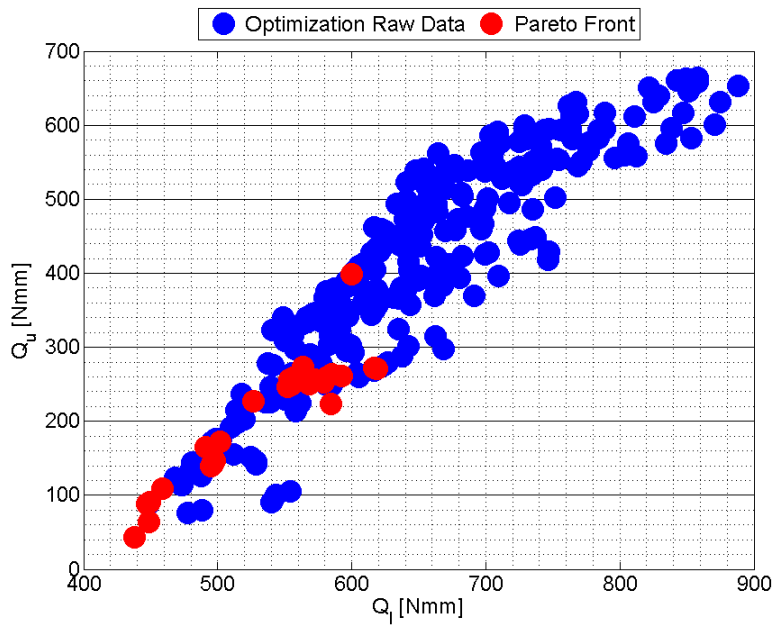


Figure C.3: Comparison of raw data and Pareto Front for torque reactions of the servo to actuate the upper and lower parts